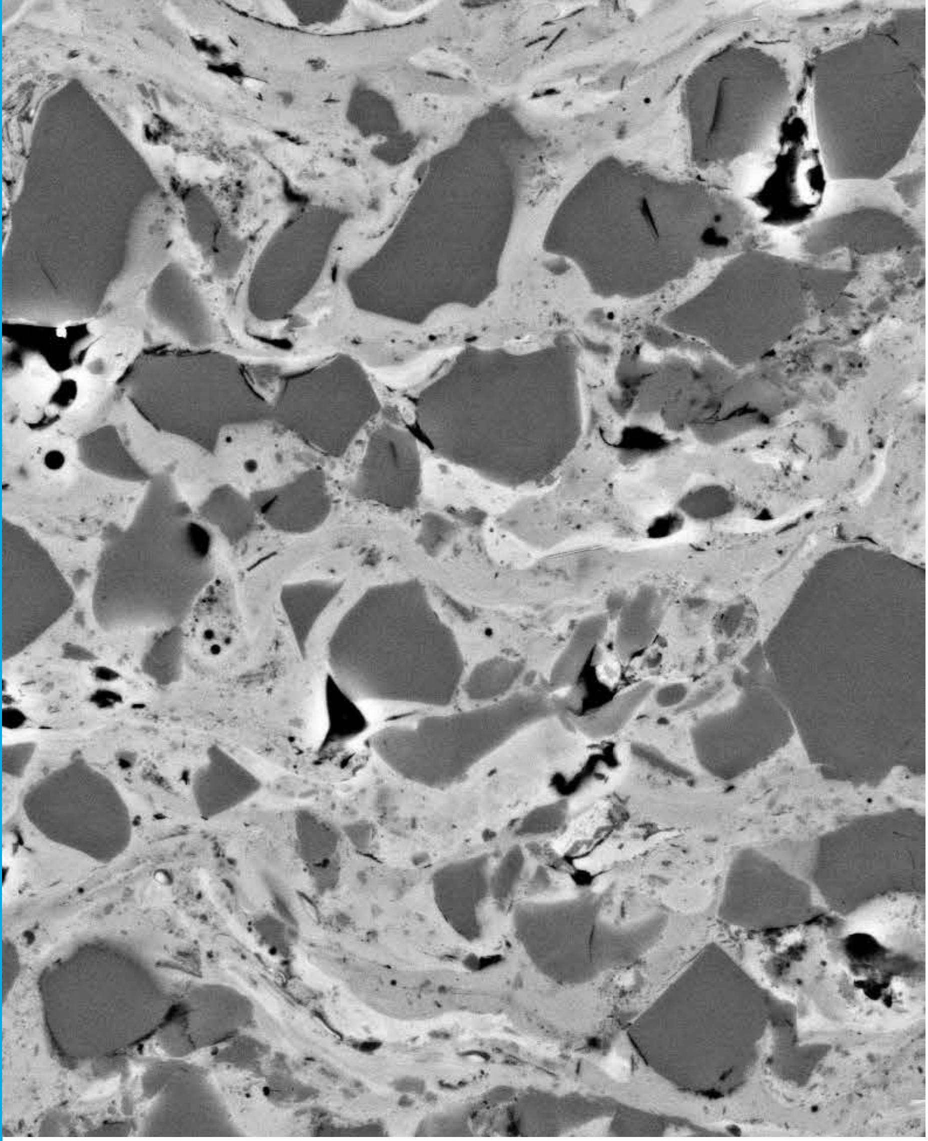

TECHNOLOGY•RESEARCH HIGHLIGHTS•VISIONS•SCIENCE•
300

The impact deformation and wear of thick composite coatings

Richard Peter Waudby

VTT

VTT TECHNOLOGY 300

The impact deformation and wear of thick composite coatings

Richard Peter Waudby

ISBN 978-951-38-8551-9 (URL: http://www.vttresearch.com/impact/publications)

VTT Technology 300

ISSN-L 2242-1211
ISSN 2242-122X (Online)
http://urn.fi/URN:ISBN:978-951-38-8551-9

JULKAISIJA – UTGIVARE – PUBLISHER

Teknologian tutkimuskeskus VTT Oy
PL 1000 (Tekniikantie 4 A, Espoo)
02044 VTT
Puh. 020 722 111, faksi 020 722 7001

Teknologiska forskningscentralen VTT Ab
PB 1000 (Teknikvägen 4 A, Esbo)
FI-02044 VTT
Tfn +358 20 722 111, telefax +358 20 722 7001

VTT Technical Research Centre of Finland Ltd
P.O. Box 1000 (Tekniikantie 4 A, Espoo)
FI-02044 VTT, Finland
Tel. +358 20 722 111, fax +358 20 722 7001

This is dedicated to my family in England and Finland who supported from the beginning to the end. Thank you all.

Preface

Richard Waudby was employed by VTT Technical Research Centre of Finland Ltd and joined the VTT Graduate School in August 2011 for a period of four years. The topic for his PhD work was "Empirical assessment and modelling of the impact wear of thick composite coatings". The work was supervised by Professor Allan Matthews at Sheffield University, UK and Professor Kenneth Holmberg at the VTT. The work was sponsored by the VTT Graduate School and some jointly funded VTT projects, mostly the project Wear resistant materials and solutions (DESICRI) subproject within the FIMECC Demanding Applications Program (DEMAPP) program. The work was supported by Tampere University of Technology, Ms Kati Valtonen, who performed the erosion testing and by City University of Hong Kong, Dr Lawrence Lee, who deposited the DLC thin film coatings for the thermal spray samples.

The PhD work was interrupted in the winter 2015-16 after Richard left VTT and later that spring he informed professor Matthews that he does not intend to finish the work. We publish here the latest version of his PhD work draft with Richard's permission even if it is not complete to make the results available for further analysis and to be benefited by the research community.

Espoo 15.5.2017

Kenneth Holmberg, Research Professor	Tarja Laitinen, Research Manager
VTT Technical Research Centre of Finland	VTT Technical Research Centre of Finland

Declaration

I hereby declare that except where specific reference is made to the work of others, the contents of this dissertation are original and have not been submitted in whole or in part for consideration for any other degree or qualification in this, or any other University. This dissertation is the result of my own work and includes nothing which is the outcome of work done in collaboration, except where specifically indicated in the text.

Richard Peter Waudby
2016

Acknowledgements

The work presented in this document is the result of collaboration between The University of Sheffield and VTT Technical Research Centre of Finland, Espoo, Finland (VTT). The majority of the work was performed on location at VTT who provided project funding, work and onsite supervision. The VTT Graduate School funding program provided 50% of the research funding. The remaining 50% funding came from a FIMECC Ltd. funded program named Demanding Applications Program (DEMAPP) managed by Dr. Markku Heino of Spinverse Oy, Finland.

This thesis is mostly related to work performed in the DEMAPP sub-project P1; Wear resistant materials and solutions (DesiCri). The aim of DesiCri was to investigate wear resistant steels and coatings for the mining and minerals industrial sectors in Finland. The project participants were Ruukki Oy, Metso Minerals Oy, Technical University of Tampere (TUT) and VTT. The University of Sheffield was a participant through assocation of the author's Doctoral student registration and by external membership to the DesiCri project.

Firstly, I would like to thank the Tribology research group at VTT who facilitated my stay. These persons include Helena Ronkäinen, Kenneth Holmberg, Aino Helle, Antti Vaajoki, Timo Hakala, Peter Andersson, Simo Varjus and Lauri Kilpi. Access to the excellent facilities was very much appreciated. Kenneth provided on-site supervision at VTT.

Secondly, I would like to thank Tommi Varis, Tomi Suhonen, Jarkko Metsäjoki, Markku Lindberg, Ulla Kanerva and Mika Jokipii for producing the experimental thermal spray coatings at VTT based upon many years worth of their own experience. Ulla performed all Xray Diffraction assessments. Jarkko performed the majority of SEM assessments with the remainder performed by myself.

Thirdly, thanks to Anssi Laukkanen, Tom Andersson and Tatu Pinomaa from the materials modelling group at VTT for their help with regards to computational materials modelling techniques. The access to the computer servers and their experience when dealing with microstructural meshing was appreciated.

Additional thanks go to Kati Valtonen, Veli-Tapani Kuokkala, Marian Apostol and

Matti Lindroos at the Technical University of Tampere who kindly allowed me access to their experimental equipment and to present at the various tribology and coatings seminars held at the university. I acknowledge the tests performed in part by Marian and Matti with the High Velocity Particle Impactor and the erosion tests performed by Marian and Kati. I always felt welcome at TUT.

I also acknowledge the support of Dr. Tom Slatter of the University of Sheffield. Tom's willingness to share his experiences of the investigation of impact wear assessment was appreciated.

The high load percussive impact tests were performed at Caterpillar, Inc. under the guidance of Dr. Colm Flannery. The visit was arranged by myself, Colm, Steve Taylor (Caterpillar Inc.) and Prof. Allan Matthews for two weeks during the Summer of 2014. I enjoyed my time at Caterpillar and I benefited greatly from Colm's experience of impact assessment and interpreting impact damage.

I would like to thank my research collaborators at Ruukki Oy, Componenta Oy, Fincoat Oy and Metso Minerals Oy who are too numerous to mention but facilitated my work through project sponsorship or by granting research visits.

Lastly, my sincerest thanks to thank Prof. Allan Matthews and Dr. Adrian Leyland of the University of Sheffield. They have both provided fine supervision when asked. In addition, I greatly appreciate the opportunities presented by them; highlights including access to special equipment, the research visit to Caterpillar Inc., IL, and long discussions in Allan's office over a cup of good coffee.

Contents

References **156**

List of abbreviations

a-C	Amorphous Carbon
a-C:H	Hydrogenated Amorphous Carbon
AE	Acoustic Emission
AFM	Atomic Force Microscope
ALD	Atomic Layer Deposition
ASTM	American Society for Testing and Materials
CJS	Carbide Jet Spray thermal spray nozzle for HVOF processes
CME	Computational Materials Engineering
CVD	Chemical Vapour Deposition
DC	Direct Current
DEM	Discrete Element Method
DEMAPP	Demanding Applications Project
DesiCri	Design Criteria Sub-project
DIN	Deutsches Institut für Normung
DJ-H	Diamond Jet Hybrid thermal spray nozzle for HVOF processes
DLC	Diamond-like Carbon
EDS	Energy Dispersive X-ray Spectroscopy
FEA	Finite Element Analysis

FEM	Finite Element Method
FIB-SEM	Focused Ion Beam Scanning Electron Microscope
Fimecc	Finnish Metals and Engineering Competence Cluster
FOV	Field of View
HT	High Temperature
HV	Hight Velocity
HVAF	High Velocity Air Fuel
HVOF	High Velocity Oxygen Fuel
HVPI	High Velocity Particle Impactor
ICME	Integrated Computational Materials Engineering
IIT	Instrumented Indentation Testing
KIC	Fracture Toughness (Mode I) found by Indentation Testing
LT	Low Temperature
LV	Low Velocity
MFP	Mean Free Path of the Binder Phase
MT	Medium Temperature
MV	Medium Velocity
POD	Pin-on-Disc
PSPP	Process-Structure-Property-Performance relationship
PVD	Physical Vapour Deposition
RH	Relative Humidity
SEM	Scanning Electron Microscope
SEM-EDS	Scanning Electron Microscope-Energy Dispersive X-ray Spectrum
SME	Small to Medium Enterprise

ta-C	Tetragonal Amorphous Carbon
ta-C:H	Hydrogenated Amorphous Carbon
TBC	Thermal Barrier Coating
TS	Thermal Spray
TS-DLC	Thermal Spray - Diamond-like Carbon multilayer
TUT	Technical University of Tampere, Tampere, Finland
VTT	VTT Technical Research Centre of Finland, Finland
WC	Tungsten Carbide
XRD	X-ray Diffraction
2D	Two Dimensional
3D	Three Dimensional

List of symbols

a	Half-diagonal length of a Vickers indentation
A	Contact area
$\mathrm{a_c}$	Indentation contact zone radius
$\mathrm{a_f}$	Area fraction of the grains
b	Crack length from a vertice of a Vickers indentation
B	Boron
c	The sum of a crack length (b) and a half-Vickers diagonal (a)
C	Carbon
Cr	Chromium
d	Initial impact distance
D	Average carbide grain diameter
E	Young's Modulus
$\mathrm{E_{IT}}$	Indentation modulus
E*	Effective modulus for a Hertzian contact analysis
$\mathrm{E_k}$	Kinetic energy
f	Frequency
F	Force
Fe	Iron

F_n	Force in normal direction
F_t	Force in tangential direction
HB	Brinell Hardness
H_S	Static Hardness
H_D	Dynamic Hardness
h_c	Peak penetration of Vickers indenter during instrumented indentation test
H_{comp}	Composite hardness
H_{IT}	Indentation hardness
HSp	Scratch hardness
HV	Vickers hardness
HV0.3	Vickers hardness with an applied indentation force of 300g
j	Constant for wear
k	Constant
K	Wear rate
K'	Wear coefficient for adhesion
K_{ab}	Wear coefficient for abrasion
K_C	Fracture toughness
K_{IC}	Fracture toughness by Indentation with a Vickers indenter (Mode I)
K_{IMP}	Wear coefficient for impact
L	Mean free path of binder
L_C	Critical failure load (Normal)
m	Mass
mA	Microamperes
Mo	Molybdenum

Mn	Manganese
N	Number of impact cycles
n	Wear constant
Ni	Nickel
N_0	Critical number of impact cycles at which wear is first observed for percussive normal impact, also known as the zero-wear point
N_L	Total number of discrete grains intersected along a plane divided by the unit length
N_S	Total number of grains per unit area
P	Applied normal load
p	Flow pressure
P_{ave}	Average load over an impact cycle
P_{KIC}	Indentation force for Fracture Toughness Assessment
P_0	Peak pressure for a Hertzian contact analysis
R	Radius of a sphere, for a Hertzian contact analysis
Si	Silicon
t	Thickness
v	Velocity
V	Volume
V_f	Deformed volume in film
V_s	Deformed volume in substrate
W	Tungsten
w	Width of scratch
x	Sliding distance

Z	Number of removed (worn) atomic layers
μ	Coefficient of Friction
μm	Micrometers
σ	Stress
σ_Y	Yield stress
τ	Shear stress
ν	Poisson’s ratio
χ	
ε	Strain
$\acute{\varepsilon}$	Relative erosive wear resistance
ρ	Density
δ	Indentation depth for a Hertzian contact analysis

List of Figures

List of Tables

Chapter 1

Introduction

Current materials science research is evolving to satisfy increased demand for high level understanding. Applied research programmes are increasingly being developed to attract small-to-medium enterprises (SMEs), in order to develop a technological platform from which those companies can grow and mature into market leaders.

Likewise, research institutes are developing holistic research methodologies to improve understanding and to offer solutions to industrial problems. One example is the Processing-Structure-Property-Performance (PSPP) chain, first described by Olsson [4]. Due to the holistic nature of the method, it is often exhausting in terms of effort and cost. However, the approach is maturing and yielding results. The work is often performed using experimental and computational means, i.e. Integrated Computational Materials Engineering (ICME). Often, computational models are used to quickly develop a representation of the investigated problem which is then validated with experimental work. The data which is used to build the computational model may be sourced from an experiment or a seperate model. Organisations such as VTT Technical Research Centre of Finland (Espoo, Finland) [5] and Questek (Evanstone, IL, USA) [6] are actively developing academic and commercial services to enable the PSPP methodology through ICME.

This thesis work utilises the PSPP methodology to investigate the impact and erosive behaviour of thick coatings and multilayer structures, from simple ideal contacts (e.g. indentation) through to complex contact conditions (e.g. erosion). The work is focussed on the demands of the mining and minerals industry in Finland. As such, the investigated materials are those which are proven or comparable to those already in use. Other focus areas such as armour ceramics, space technology, paper and pulp processing and bioprosthetics may benefit from the work presented henceforth.

1.1 Tribology

When the subjects of physics, chemistry, materials science, biology and mechanical engineering collide; tribology is formed. Whilst this does little to define what tribology is, it does suggest its depth in terms of contributing research fields. Jost [7, 8] referred to tribology as “the science and technology of interacting surfaces in relative motion and of the practices related thereto”. Much like other research fields, it is a systematic study of a problem, e.g. two or more bodies interacting with each other by some means. For the purposes of this thesis, these interactions shall be limited to mechanical means although some thermal and chemical interactions will be considered when appropriate.

The research field of tribology revolves around the concepts of wear, friction and lubrication. The term tribology derives from the Greek word, tribo, which means “to rub”. As such, any contact which is subject to a load and translation of the surface can be investigated under the field of tribology. This may include rolling, sliding, a normal approach or the seperation of surfaces[9].

The scope of this thesis is mainly interested in tribology with respect to wear, although friction is considered to a lesser extent. Lubrication is not considered, although the use of a lubricant is often considered when investigating or resolving a tribological problem.

1.1.1 Mechanical properties

Hardness

The static hardness, H, of a material is used to define a material’s resistance to plastic deformation. This can be found with various methods and the results may vary depending upon the method and parameters chosen. Generally, a static hardness test involves creating an indent in a material surface by pressing an indenter of known size, geometry and mechanical properties against the test surface under a set load-time or displacement-time profile. The indent is then examined in accordance to the chosen method. The static hardness, $\mathrm{H_s}$, is often used to estimate the Yield Strength, σ_Y, of a material with Equation 1.1.

$$H_S \approx 3\sigma_Y \tag{1.1}$$

Otherwise, the dynamic hardness may be assessed at higher deformation rates. As for static measurements, the hardness result is dependent upon the test parameters. More information on defining hardness is available elsewhere [10].

Elastic Modulus

The Elastic Modulus, E (otherwise known as the Young's Modulus) is the slope of the linear and elastic section of the stress-strain curve. It is used to define how easily a material will deform elastically, i.e. without permanent deformation. The Elastic Modulus can be found by a variety of methods including , atomic force microscopy (AFM) [11], wave techniques [12] and instrumented indentation [13, 14]. More information on defining Elastic Modulus is available elsewhere [10].

Fracture Toughness

The fracture toughness of a material, K_c, is the ability of a material which has not yielded to resist fracture. Depending upon the desired mode of fracture to be investigated, fracture toughness can be found with bend tests, shear tests and modified indentation tests.

1.1.2 Wear

Wear is generally regarded as the displacement and removal of material from a tribological contact [9]. It is distinct from the elastic and/or plastic deformation of a surface which do not include material loss. It is often desired that wear is minimised in order to ensure that the surface stays close to the original dimensional tolerance. However, some applications are so that they demand that a surface will be subject to a controlled degree of wear. The aerospace industry provides good examples of both cases. In favour of wear, the turbine blade edges are expected to wear by abrasion to ensure a minimal seperation between blade edge and the inner diameter of the turbine housing. In opposition to wear, the landing gear bearings are subject to high impact loading, fatigue, scuffing and even adhesive wear due to high temperatures.

There are numerous mechanisms with which material can wear from a surface. These may occur in parallel and enabling or reducing the loss of material for a given mechanism [15, 16]. For low to moderate contact pressures, wear is assumed to be as a result of interasperity contacts. It should be noted that for some high deformation, high impact contacts that this may not be the case [9] .

Adhesive wear

Adhesive wear occurs when two contacts bond together and then shear; it is often severe. It is normally observed on unlubricated contacts which may be otherwise inert in the tested environment except by contact with the other sliding body. The presence of any agents which may alter the state of the surface, such as oxidisers, may reduce the influence of adhesive wear. This is particularly true for metal-metal contacts. For example, the presence of an oxide film on a metal surface may reduce the likelihood of adhesive wear, unless it is removed before or during the sliding contact. The sheared layer will often transfer off the weaker material, leading to wear of the of the weaker material[17].

Abrasive wear

Abrasive wear occurs for a sliding contact when there are hard particles, or volumes, loaded against a softer surface. The hard particles may be embedded into a sliding surface (two body abrasive wear) or loose and may roll (three body abrasive wear)[18]. There are four basic mechanisms of abrasive wear; cutting, fracture, fatigue by repeated ploughing and grain pull-out.

Abrasive wear can be investigated with a variety of different test methods, including scratch testing [19, 20], rubber wheel [18, 21] and pin-on-disc [22, 23].

Corrosive and oxidative wear

Corrosion is a process where a material changes composition, due to chemical reactions with another material. Oxidation is where the corrosive medium is oxygen or an oxygen compound and that the affected volume is transformed into a more stable oxide[24]. Wear can occur by a number of means in loaded or unloaded contacts. Pitting due to cathodic/anodic potentials may occur without loading and as such it is not a tribological contact, however a tribological contact may occur and interact simultaneously. Additionally, a tribological contact (e.g. impact, abrasion) may damage and wear the corroded region. Subsequently, corrosion may be seen at the recently worn site and form a new, corroded volume.

Fatigue wear

Cyclic loading which leads to progressly increasing damage and wear to the investigated material is known as fatigue wear. The number of loading cycles may vary from order of magnitudes of tens through to millions and more. The time period between the inital loading step and the final load step at which failure occurs is the fatigue lifetime. The maximum stress that is subjected to the material is often a fraction of the stated yield stress limit. As such, plastic deformation is not observed if the maximum stress is below the yield stress. Typically, microscopic cracks form along weak interfaces or at stress concentrators (e.g. grain boundaries, pores, defects) and propagate slowly before sudden crack growth and ultimate failure.

Impact and erosive wear

The wear of material due to impact occurs when a surface is loaded and unloaded over a short time period by a single particle. As well as loss of material, there may be heavy deformation and wear mechanisms acting simulataneously with impact wear. More information on impact wear is presented in Section 1.2.

Erosion is similar to that of impact, in the sense that the impacting erosive particle quickly loads and unloads the surface. However, erosion usually implies that there are multiple particle impacts occuring simultaneously across a wider area. In that sense, erosion is chaotic whilst impact is controlled.

For both impact and erosion, one often investigates the influence of the impacting angle, impact momentum (mass, velocity, acceleration) and of the impacting particle (shape, mass) itself.

Wear equations

Due to the high complexity of wear, there is no universal equation or model. Numerous models and equations have been developed to describe the wear of materials under select regimes, such as adhesion, abrasion and impact.

Holm [25] describes adhesive wear for a sliding contact with an applied normal load, as shown in Equation 1.2. The wear value is based on the total number removed atomic layers, Z. The flow pressure, p, sliding distance,x, and applied normal load, P, must be known. It provides a good basis for a simple wear equation but it is difficult to use to assess laboratory or in-field test results as monitoring the change of number of atomic layers is challenging.

$$V = \frac{ZPx}{p} \tag{1.2}$$

More famously, Archard [26] developed an approach. It is suitable for a sliding adhesive contact where the wear volume, V, is found according to Equations 1.3 and 1.4. Note that two of the wear rate, K, coefficient of wear, K', and hardness, H, must be known. This method is similar in form to that of Holm[25], where the sliding load and applied forces are considered. The Archard version includes the hardness of the investigated material and so allows easier comparison. As it does not feature any atomic scale definitions, i.e. Z, it can provide simple and easy comparison of similar laboratory scale assessments.

$$K = \frac{K'}{H} \tag{1.3}$$

$$V = K'\frac{Px}{H} \tag{1.4}$$

For abrasive wear conditions, Rabinowicz [27] developed an approach which is nominally similar to that of Holm [25] and Archard [26]. The contact assumes that there are two bodies in relative motion, sliding for a finite distance against an applied load. The primary difference is that to calculate the predicted wear volume, an abrasion coefficient, $\mathrm{K_{ab}}$ should be known. The abrasion coefficient varies depending upon the tribological system.

For impact contacts, there are few equations and models for the prediction of wear. This is due to the complex tribological interactions between impacting bodies and wide variety of different impact modes and model tests, as well as a lack of prior research data. Engel [3] stated that the contact conditions must be well defined in order to predict wear. Aspects including the contact area, mechanical properties of the impacting bodies, tribological conditions and impact conditions should be well defined. In practice, this is difficult as impact tests are often poorly controlled and often use unstandardised methods. Standard methods enable the development of research data on a subject, which allow comparison on a like-for-like basis.

A modelling technique for predicting compound wear was suggested by Lewis [28], as part of a short communication built upon the research of Engel. The approach was to combine previous models developed for erosion and impact conditions with that of the sliding model developed by Archard [26] for a compound impact approach. It assumes that the impacting body is rigid and does not deform, whilst the impacted body does deform. The relationship is shown in Equation 1.5.

$$W = \left(\frac{kP_{ave}Nx}{H} + K_{IMP}NE_K^n\right)\left(\frac{A_i}{A}\right)^j \tag{1.5}$$

The primary part of the equation is based on the Archard work [26], where 'k' is a sliding constant, $\mathrm{P_{ave}}$ is the average load over the contact time, N is the number of impact cycles, x is the sliding distance and H is the hardness of the impacted body. The second part is based primarily on the impact nature of the contact, where $\mathrm{K_{IMP}}$ is the impact wear coefficient, $\mathrm{E_K}$ is the kinetic energy of the impact and n is an empirically derived constant for wear. Both parts are subject to modification by the ratio of initial contact area to final contact area after N cycles and j is a wear constant.

1.1.3 Friction

Friction is defined as a resistive force between two or more bodies which are in relative motion. The bodies may be as a fluid or solid. Friction is often reported as a systemic value, i.e. it is not a material specific property. From a tribological perspective, it may be defined by the mechanical properties, relative movement, environmental conditions and lubrication of the sliding materials.

$$\mu = F_t / F_n \tag{1.6}$$

For a tribological assessment, it is often possible to measure both the force loading the contact (Fn) and the resistive transverse friction force (Ft) for a sliding contact. Friction is normally reported as a dimensionless value and it is given the symbol, µ. One should exercise caution when comparing friction coefficients obtained with differing contacts, such as those between standardised and non-standardised methods [29].

1.2 Impact phenomena

The study of impact behaviour has some importance to fields including cutting tools, minerals and mining, aviation, space technology and armour protection. For example, failure of tooling used for tunneling into rock due to impact will lead to higher operational costs due to reduced productivity, necessary maintenance and replacement of the broken item. Other applications where understanding impact are even more critical where human life can be endangered. A good example is the Columbia Shuttle Disaster, 1983, where a wing section was damaged due to an impact event with foam and ultimately led to the loss of life of seven crew members [30].

Impact damage can occur across a variety of different length scales. For example, impact deformation may vary from deformations of micrometres during particulate erosion impact events [31]through to kilometres when considering meteorite impacts[32]. The means to describe the impact event can remain similar.

1.2.1 Impact wear

Impact wear has been defined by P.A. Engel as “the wear of a solid surface that is due to percussion, which is a repetitive exposure to dynamic contact by another body”[3]. This is true for contact conditions subjected to an impact fatigue condition whereby repeated loading deteriorates the contact surfaces. In addition to this, impact tests can also be performed with a single impact event under similar conditions.

Impact tests can also be paired with other wear mechanisms such as erosion (ref Ratia) and abrasion [33]. The presence of a secondary wear mode may accelerate wear of the surfaces leading a reduced operational lifetime in the real application. In that sense, Engel’s[3] definition of impact wear is somewhat restrictive yet offers differentiation to erosive wear. Typically, erosion particles are relatively small with varying shapes and sizes, they have a velocity and mass distribution and do not repetitively and sequentially strike the same site. In that sense, the difference between erosion and impact is the precision and control of the impact event.

1.2.2 Impact mode

When assessing the behaviour of a material system under dynamic impact conditions, it is important to understand and control the impact mode. There are three basic impact modes with respect to orientation and contact; normal impact, compound sliding-impact and compound angled impact. A schematic summarising the impact

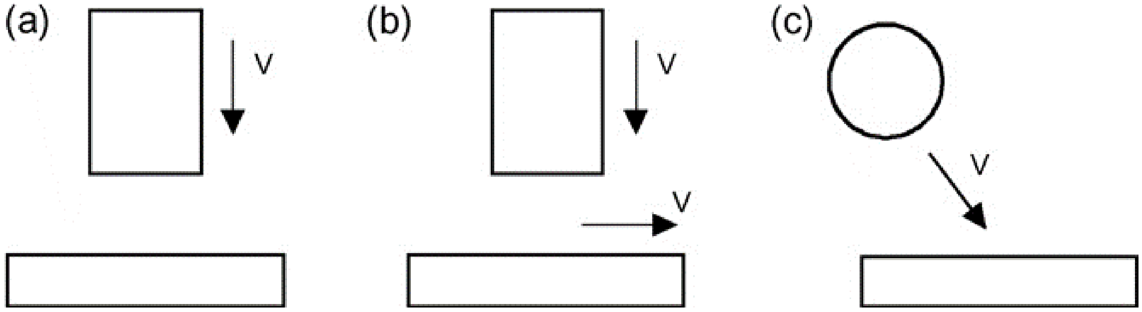

* Note that the arrow describes the direction of motion for the impacting body, whilst the symbol “v” describes the velocity [28]

Figure 1.1: Schematic of impact modes, with normal impact mode (a), compound sliding-impact (b) and compound angled-impact (c)

modes is given in Figure 1.1.

Normal impact

Normal impact test methods have been used to assess the performance of thin film ceramic coatings for cutting tools [34, 35] for fatigue, fracture and wear. The method was initially developed by Knotek et al. [36] to simulate wear and fatigue under high local dynamic stress on the surface[37] by repeatedly impacting a test specimen with a hard counterface. Through repetitive, controlled impacts, it is possible to investigate wear and deformation rates, as well as the link between total impact cycles and failure.

The impact force, impact duration, number of impact events and impact frequency are often controlled. The impact force is determined by the impacting mass, impact velocity and deformation behaviour of both the counterface and impact test specimen. Usually, the loading geometry is ball-on-flat which is relatively simple due to high symmetry which permits easier use of Hertzian contact analysis. A schematic diagram of such an arrangement is given in Figure 1.2[38]

Normal percussive impact test methods have since been used as a means to assess thin film deformation and wear [39]and to investigate erosion performance [31].

Compound impact

Likewise, compound impact test methods are also commonly used. Compound impact contacts introduce a substantial shear component by a sliding or non-normal angled contact. The impacting counterface may be fixed[41, 42] or free, i.e. a projectile. For the latter case, the projectile velocity is often generated by pressurised gas [43] or gravity [44]. The test is often actively monitored to provide better understanding of the

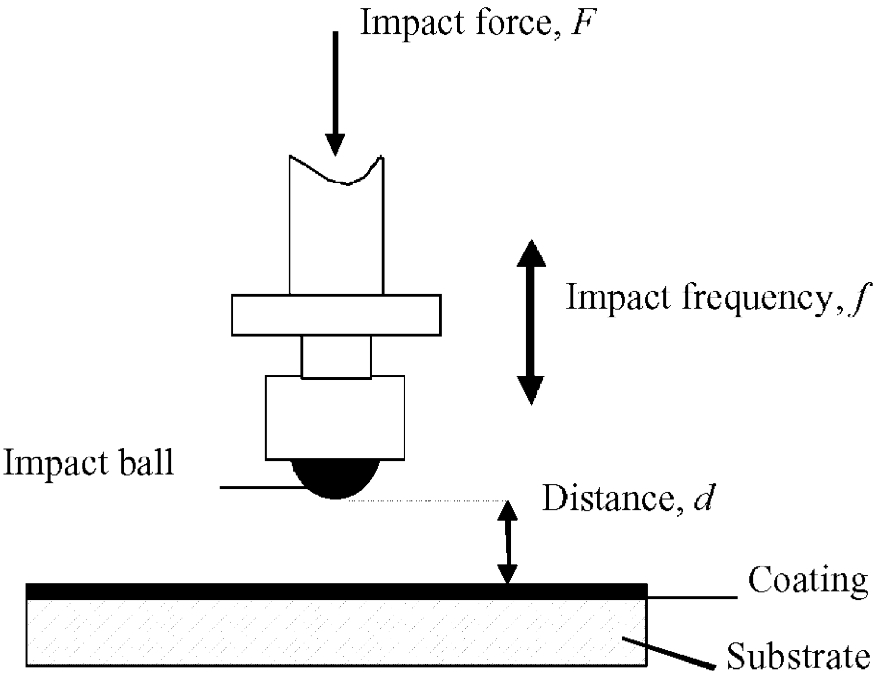

[40]

Figure 1.2: Schematic drawing of a normal percussive impact test at normal incidence

impact event. Monitoring methods include high-speed video cameras for visualisation of deformation and wear [45], use of speed guns to monitor particle velocity to aid the calculation of particle impact energy [46] and force sensors to measure the impact forces subjected to the test sample. The main controllable variables are particle velocity (v), particle mass (m), impact angle, and the number of impact events. The impact force is determined by the impacting mass, impact velocity and deformation behaviour of both the impacting particle and the impact test specimen. The peak impact energy is normally found by the Newtonian kinetic energy equation (1.2) which assumes that factors such as drag and rotational energy are null.

$$E_k = \frac{1}{2}mv^2 \tag{1.7}$$

1.2.3 Coefficient of restitution

The coefficient of restitution, e, is used to describe the tranformation of energy during a collision between two or more impacting bodies. It is based on the ratio of relative speed after the collision for the two bodies, V', annd the relative speed before the collision for the two bodies, V. An equation for a two body impact event is given in

Equation 1.8.

$$e = \frac{V_2' - V_1'}{V_2 - V_1} \tag{1.8}$$

The coefficient of restitution can be used to determine the elasticity of the impact event. An elastic impact event has no energy transformation, i.e. the kinetic energy of the impact bodies before and after the collision are equal. Thus, e = 1. If e = 0, the collision is inelastic and the impacting bodies are assumed to coelesced. For most impact tests of hard materials, the coefficient of restition is found between 0 and 1.

1.2.4 Lubricated impact

It is common to study impact behaviour under dry conditions, to minimise the variables present during assessment. However, lubrication effects may be observed for real applications. For example, the loader of a mining truck may be wet due to rain or other environmental factors, leading to modification of the impact event by wetting of the surfaces and modification of local substances, e.g. soil and clay. Medical prostheses such as artificial hip joints and heart valves are also subject to lubricated impacts.

Bowden and Tabor[47] and Finken [48] used the dropball test method to investigate the role of a lubricant on the plastic deformation of a metallic substrate due to impact by a harder body. It was noted that the deformation was deeper for a lubricated contact than for an unlubricated contact. This was also observed for a study of non-metallic materials subjected to impact loads by a pivotal hammer apparatus in [49], when using a sharp counterface. Additionally, the lubricant was suspected of promoting the propagation of cracks.

1.2.5 Summary of impact phenomena

In conclusion, impact test methods are applied across different fields and scales. In terms of material science and tribology research, some methods are available and are published. The impact contact is complex in comparison with other tribological test methods. This is due to it being a dynamic contact where factors such as deformation, friction and wear are evolving over short time scales.

1.3 Thick and thin coatings

Coatings are often employed as a means to modify friction, wear or deformation behaviour of a surface. There are a multitude of different materials which may be used and processes in which to apply. This section will mainly focus on thick Thermal Spray (TS) coatings with minor contributions on Physical Vapour Deposition (PVD) and multilayer coatings.

1.3.1 Thermal spray

Thermal spray is a term used to cover a variety of related techniques which may deposit a coating onto a target surface by the acceleration molten or semi-molten particles. These particles mostly impact the target area and build up a coating comprised of multiple lamellae (or splats). A thermal spray coating is often complex in terms of its microstructure, chemisty and mechanical properties. The links between materials processing, microstructure, material properties and performance in application are strongly researched worldwide [50, 51].

Thermal spray in industry

The thermal spray family of methods are used to apply coatings for a variety of industries. The technique is commonly used solve problems involving:

- Excessive wear [52]
- Thermal behaviour, i.e. conduction and insulation [53]
- Corrosion [54]
- Friction modification [55, 56]
- Aesthetics

Thermal spray processing

The first published example of the use of a thermal spray method was by Dr M. IJ Schoop in 1910 as a means to spray metallic lead [57]. Currently it is possible deposit a wide variety of different materials such as metals, ceramics, polymers and their composites with a wide array of processing conditions. A summary of the range of thermal spray processes is given in Figure 1.3 [58].

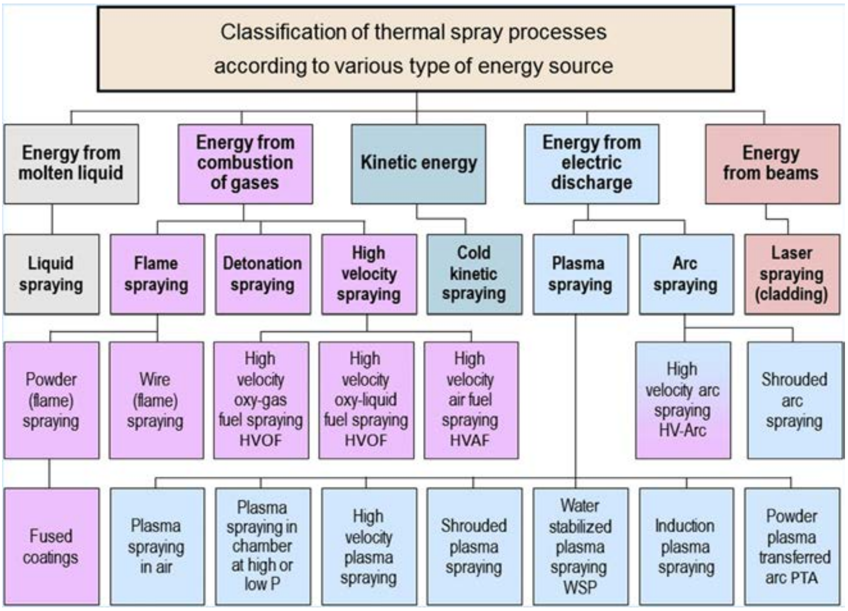

[58]

Figure 1.3: Summary of the thermal spray process family according to the type of energy source

Typically, a heat source is used to melt a feedstock material which is accelerated towards the intended coating site. The heat source may be a combustion flame, electric arc or a plasma field. The aim is to melt or partially melt the feedstock prior to it impacting the target site. Consequently, the melting point of the feedstock should be considered when choosing the correct spray process. For example, ceramics and refractory metals, such as tungsten based materials, are commonly sprayed with electric arc, plasma [58, 59] or HVOF [58, 60] methods as these can suffiently melt the feedstock material for it to flow on the target during particle impact. Likewise methods which are typically cooler, such as HVAF or cold kinetic spray[61] are often used to deposit low melting temperature materials such as metals [62, 63]or those which may degrade at elevated temperatures, such as polymers[64] or hardmetals [65]. Figure 1.4 gives a useful plot to show the typical temperature and velocity parameters for different thermal spray processes.

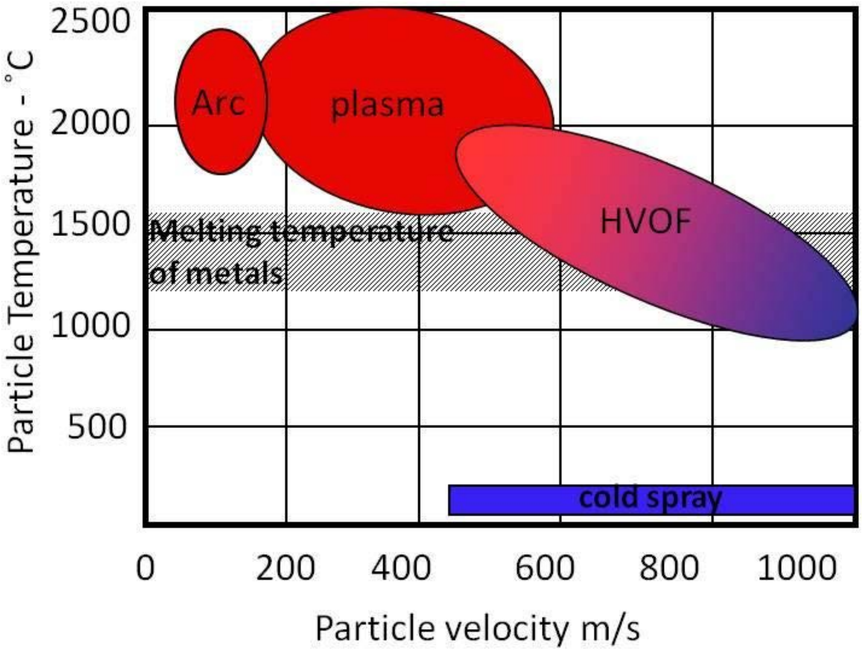

[60]

Figure 1.4: Particle temperature and velocity in different thermal spray techniques

The spray temperature may have a significant influence on the final coating. High spray temperatures may lead to the formation of meta-stable phases[66] due to inter-splat diffusion leading to high cohesive strength or changes to the substrate should cooling not be sufficient.

Within a spray process, the choice of fuels and nozzle type can also influence the final coating and should be considered. For example, powder-fed HVOF nozzles are generally classified as 1st, 2nd or 3rd generation. Figure 1.5 shows typical particle temperature and velocity ranges for such nozzles.

Generation	Nozzle type	Total heat output	Chamber pressure	Spray rate (WC-Co)
-	-	kW	bar	kg / h
1st	straight	80	3 - 5	2 - 6
2nd	De laval	80 - 120	5 - 10	2 - 10
3rd	De laval	100 - 300	8 - 12	10 - 12

[54]

Table 1.1: Typical descriptors of HVOF systems

As seen in Table 1.1 [54], each new generation of nozzle features improved heat output, pressure and spray rate. The choice of nozzle further influences the morphology of the coating leading to differences in phase composition and mechanical properties.

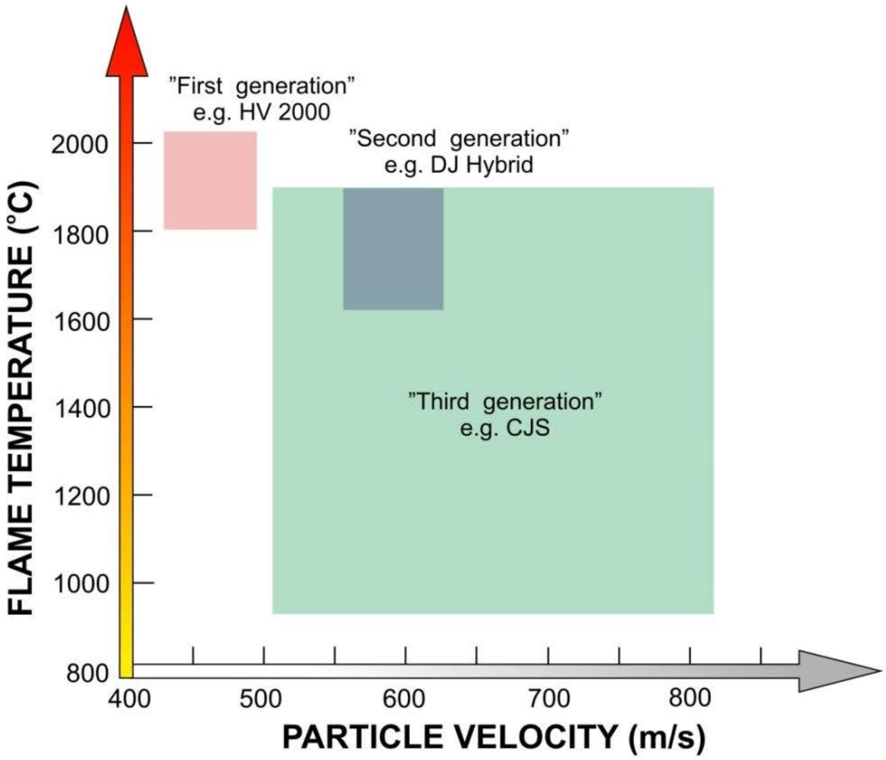

[67]

Figure 1.5: Typical parameter ranges for 1st, 2nd and 3rd generation HVOF nozzles

The coating thickness can vary from tens of microns through to several millimeters depending upon on the materials used and the spray process. The thickness limitation often arises from high residual stresses in the coating [68] which may cause the coating to offer compromised cohesive strength, excessive cracking or even partial or full delamination of the coating.

Thermal spray feedstock materials

Significant control over the final coating can also be gained through the use of different feedstock materials. The feedstock is typically in the form of a powder or wire, although liquid suspensions are gaining traction in research environments. The choice of feedstock form is dependant upon the spray method and the material to be sprayed. There are clear advantages to both powder and wire morphologies.

Powders are made to certain compositions, particle sizes and particle size distributions. A range of methods are available to use including atomised, fuse/sinter and crushed and agglomeration and sintered. Powder morphology MAY influence final material and mechanical behaviour of sprayed coatings and as such it should be carefully considered.

Summary of thermal spray methods

The wide versatility of thermal spray methods is attractive. Through control of particle processing parameters (such as spray temperature, particle velocity), feedstock materials, fuels and nozzles types it is possible to create a variety of different coatings. It is a vibrant industrial field with strong research activities and rapid development of materials, processes and new applications.

1.3.2 Thin hard films

Thin films are able to be manufactured with a wide variety of different methods including chemical vapour deposition (CVD) [69], physical vapour deposition (PVD)[69] and atomic layer deposition (ALD)[70–72] based methods. These are all capable of depositing thin films which have thicknesses below 5 µm. Thus, thin, hard coatings can be applied which are primarily ceramic and hardness may be in excess of 20 GPa[73–75]. This section will focus on coatings for wear protection and friction modification by the PVD method in accordance with the materials investigated in the thesis.

Physical vapour deposition relies on the atomisation or vapourisation of a source material and then subsequent deposition of that material onto a target substrate [69]. There may be one or more source materials used during the coating process. It is possible to create coatings which have single layers, multiple layers of different composition [76] or graded compositions as a function of depth [77–79] by controlling the rate of flow of material from the source to the target substrate. A wide variety of different materials may be applied with the PVD method. Initially, metallic coatings were deposited [69] however ceramic and alloyed are also applied. As such, multilayer composite coatings are possible, such as a alternating ceramic-metallic layers. This allows coatings to be as simple or as complex as required by the intended application.

Coatings manufactured by PVD methods are used for a wide variety of different applications. These include wear protection [80–83], friction modification [84, 85] and for aesthetics [86, 87].

Diamond-like carbon

Diamond-like carbon (DLC) films are able to be applied by CVD and PVD methods. DLC films are made primarily of carbon and have some similarities to natural diamond, although hydrogen and other dopants may also be present. Elemental carbon may also form graphite, fullerenes or nano-structures such as nanotubes. For DLC coatings, it is possible to control the form of the DLC by adjusting the ratio of sp2 and sp3 bonded carbon, and Hydrogen atoms, as shown in Figure 1.6. The figure shows the different general classes of undoped DLC films; a-C (amorphous carbon), a-C:H (amorphous carbon with significant quantities of sp2 bonded carbon), ta-C (tetragonal amorphous carbon) and ta-C:H (tetragonal amorphous carbon with significant quantities of sp2 bonded carbon) [88]. Through controlling the quantity of sp2 to sp3, one can adjust mechanical properties such as hardness and elastic modulii, reaching similar levels to natural diamond . Generally, Hydrogen is applied to prevent the film transforming to the more stable phase, graphite.

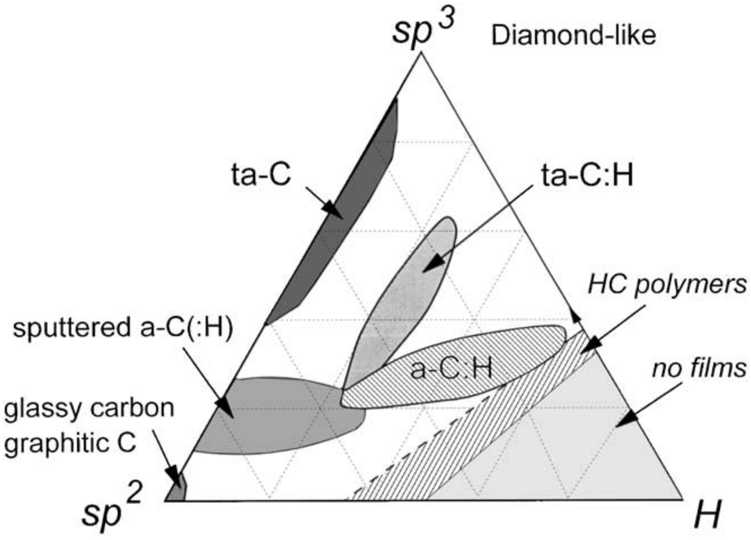

[88]

Figure 1.6: Ternary diagram of the C-H system

DLC films are often applied onto bond and gradient layers, especially when coating metallic substrates. This may be due to concerns over thermo-elastic mismatch or poor adhesion. The bond coat thickness is often less than 1 µm. The adhesion and thermo-elastic mismatch between the bond coat and the DLC film may be improved further by including a graded layer. Finally, metallic elements may be added during the DLC deposition process in order to develop special functionality (e.g. chemical reactivity)

[89, 90] or to improve the load bearing capability. Such versatility with respect to the form of DLC films has helped them to be widely used across industry for tribological applications.

1.3.3 Hybrid thermal spray-thin film coatings

There is a limited amount of literature related to hybrid multilayer coating systems of any description which include a thick thermal spray layer and a thin film layer. Often, the thick thermal spray layer is an interlayer between a metallic substrate (e.g. steel or aluminium) and a thin hard film (e.g. DLC, TiN). Bolelli et al. found that a hard WC-Co interlayer between a steel substrate and DLC film offered improved fracture and delamination performance under scratch and indentation testing[91]. This is due to the hard interlayer bearing the load with reduced deformation as a result of high elastic modulus leading to reduced strain of the thin film. Likewise, Bolelli et al. found that similar benefits are to be found with a similar interlayer and DLC film applied to an aluminium substrate under scratch and indentation contacts[92]. It was also noted that the DLC film afforded no benefit towards corrosion resistance.

These hybrid thermal spray-thin film process coatings are largely restricted to demanding, high value applications or for academic interest. The costs related to coating equipment, surface preparation and their infrastructure are prohibitive. Similar results can be obtained with duplex diffusion processes, such as carburisation and nitriding [38] of the substrate prior to the application of the thin hard film.

.

1.4 Aims

Numerous researchers have demonstrated the effectiveness of the Processing-Structure-Property-Performance (PSPP) approach[4, 51, 52, 93]. This is a methodology which aims to develop the understanding of the relationship between the material processing, material structure and microstructure, material properties and material performance for a given application. It requires an extensive effort due to the holistic nature.

This work aims to follow a similar approach, with an emphasis on the impact, sliding and erosive wear of thick, composite hard coatings and their material properties. A flow chart which shows the investigation process is given in Figure 1.7. The material properties are defined by the choice of raw materials and their processing (see Chapter 3). The effect of the material properties are considered for laboratory scale assessment: scratch performance (see Chapter 4), percussive impact (see Chapter 5) and compound sliding impact (see Chapter 6). Subsequently, both material properties and laboratory scale assessments are compared against erosion performance, to establish whether any relation can be established to offer improved understanding of the erosive contact(see Chapter 7). Consequently, the whole framework, as shown in Figure 1.7, is discussed to offer improved understanding on the PSPP relationship for the investigated materials underimpact, sliding and erosive conditions. A summary of the aims is given below.

- To investigate the tribological properties of commerical and experimental coatings
- To improve the understanding of impact wear mechanisms of composite coatings
- Develop a PPSP-based relationship for the assessment of the impact, sliding and erosive wear of thick, composite coatings
- To develop understanding of how to design impact resistant, thick coatings

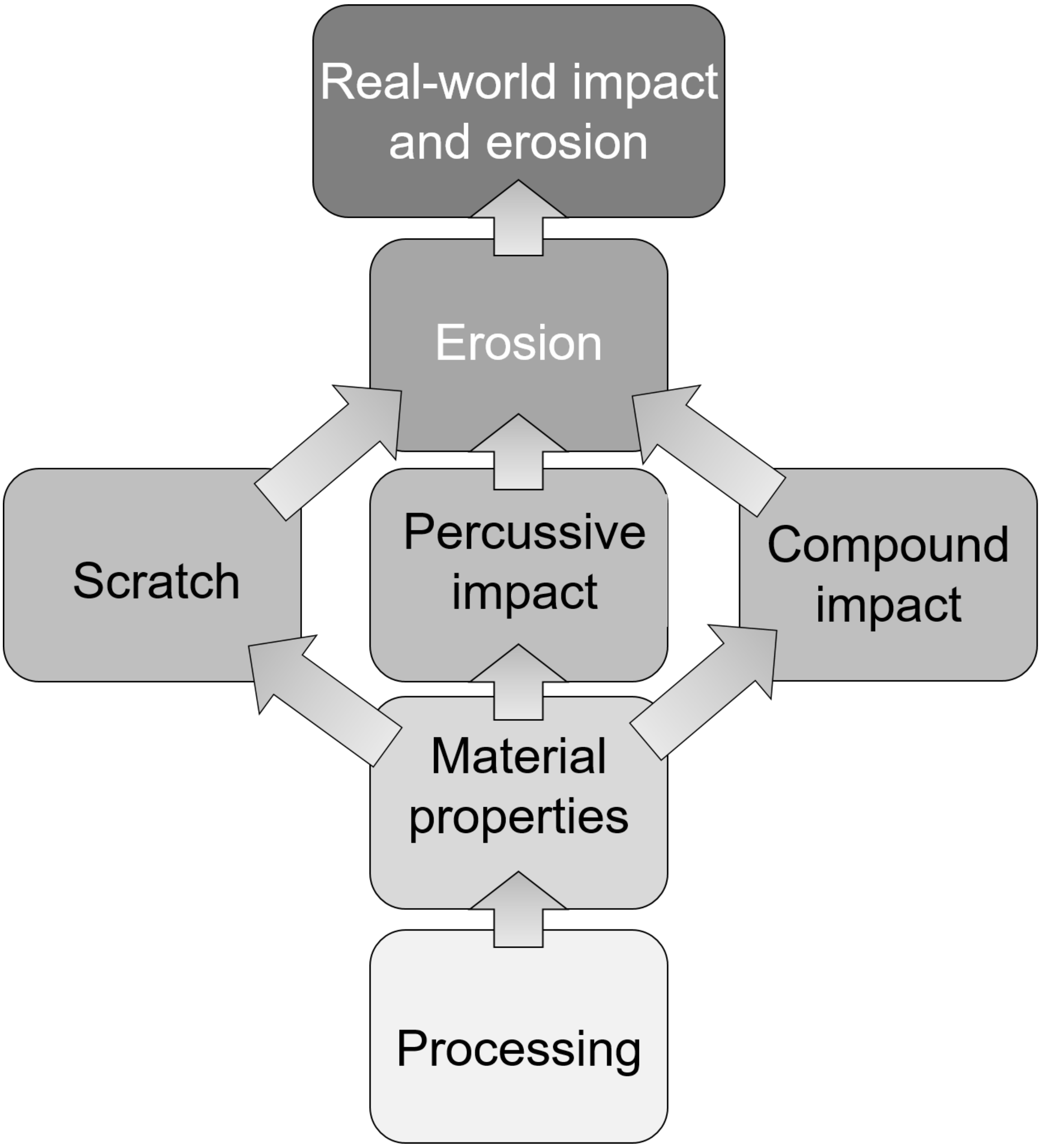

Figure 1.7: Investigation framework for the research activities presented in this document

Chapter 2

Research methods

The methods employed for the research reported in this thesis are given in this chapter, along with a brief summary of the techniques and equipment that were employed. This chapter includes the analytical work related to characterisation of the investigated materials, surface analysis, mechanical testing and tribological testing.

2.1 Analytical work

In this section, details are presented concerning the methods employed to characterise the investigated materials.

2.1.1 Surface preparation and roughness

All samples were ground and polished to a mirror finish, where the average roughness (Ra) was less than 1.5 µm. Suitable diamond-embedded discs for grinding to create a flat and even test surface under even load. Final polishing was done by hand using cloth polishing mats and diamond suspensions (9µm, 3µm and 1µm grit). Surface roughness was assessed by 2 dimensional stylus profilometry prior to experimental testing. A minimum of five measurements were taken at different orientations, per sample, and results averaged. The test parameters are given in Table A.1.

2.1.2 X-ray diffraction

X-Ray Diffraction (XRD) was used to determine the material phases in sprayed samples. It also gave an indication of the quantity of amorphous, i.e. non-crystalline, material in the coating. A Philips PW 3710 device with with Mo K-alpha radiation source was used at 2theta orientation. The voltage was 45 kV and the current was 35 mA, with a 0.2 µm step size.

2.1.3 Scanning electron microscopy

Scanning Electron Microscopy (SEM) was used throughout the investigationas as an aid to to characterise the materials, worn surfaces and failures. Primarily, an UltraPLUS Thermal Field Emission, Carl Zeiss Microscopy GmbH., Scanning Electron Microscope w ith an UltraDry EDS Detector, Thermo Fisher Scientific Inc., was used due to high resolution imaging capability. Otherwise, a Philips XL30, Philips, NL, SEM with an UltraDry EDS Detector, Thermo Fisher Scientific Inc., was used in a limited capacity. During SEM operation, a focused beam of electrons is scanned over the investigated surface. Depending upon the detector which is employed, secondary or backscattered electrons are used to generate the image of the investigated site.

Secondary electrons are the product of inelastic collisions between the electrons of the scanning, focused electron beam and the valence electrons of the investigated surface. The affected depth is typically on the order of nanometres as the secondary electrons are relatively low energy and cannot escape the investigated material from depths greater than several nanometres. Increasing the acceleration voltage of the focused electron beam will increase the affected depth, however topographical resolution may be reduced due to the increased detection of electrons originating from below the surface.

Backscattered electrons are the product of elastic collisions between the focused, scanning electron beam and the nuclei of the atoms of the investigated surface and near-surface regions. As such, backscattered electrons are used to assess compositional or topographical features. As with secondary electrons, increasing the accelerating voltage of the focused electron beam will increase the affected depth and the detector count.

Scanning electron microscopy was used to generate images of the microstructure of the investigated materials and to visualise the failures generated by the test methods described in Sections 2.2 and 2.3.

Microstructural assessment by image analysis

Images of the microstructure were taken with secondary electron SEM imaging and processed to define the binder mean free path (MFP), number of carbides per unit area, average carbide diameter, porosity content and matrix content by area. The

SEM images were subject to image analysis with ImageJ (ref) software. Each image subject to thresholding to identify open pores and cracks, as these areas appear darkest and the area fraction calculated. Then, the image was converted to a binary (black or white) image and subject to various analysis methods. The mean free path calculation was made in accordance with Equations (3, 4 and 5), developed by S. Usmani [94, 95]. Note that D is the average carbide grain diameter, L is the mean free path of binder, $N_L$is the number of discrete grains intersected along a plane divided by the unit length, $N_S$is the number of grains per unit area and a_f is the area fraction of the grains. Note that grains can include porosity and and non-carbide forms, unless explicitly removed by good thresholding of the image. Each image was subject to 30 individual line measurements for N_L. For each investigated material, 1 to 2 images were assessed.

$$D = \frac{4}{\pi}\frac{N_L}{N_S} \tag{2.1}$$

$$L = \frac{1 - a_f}{N_L} \tag{2.2}$$

$$a_f = N_L D \tag{2.3}$$

2.1.4 Scanning electron microscopy - energy dispersive Xray analysis

SEM-Energy Dispersive X-Ray Analysis (SEM-EDS) was used to identify local elemental composition by measuring the relative intensity of suspected elements. Due to electrons ionising the near-surface atoms, Xrays are emitted whose wavelengths can be used to identify the local elemental composition. Both unworn and worn surfaces for investigated. Worn surfaces were assessed to understand the elemental composition of tribofilms.

2.1.5 Optical microscopy

Wear and failure modes were assessed with optical microscopy. A variety of different objectives were used in accordance with the scale of the investigated feature.

2.1.6 Non-contact optical profilometry

Non-contact optical profilometry was used to generate 3D representations of the worn surfaces, so that the deformed and worn areas and volumes could be assessed. The assessment was performed with the Sensofar Plµ 2300 hardware and Sensofar Plµ 2.31 software (Sensofar Tech S.L., Spain), hence forth known as the Plµ system. For most assessments, a 20x objective was used as it facilitated a wide depth range to accomodate varying sample slopes. Due to the large areas that were assessed, multiple field-of-views (FOV) were taken and combined to form a composite image. The assessment area, depth range, resolution and brightness parameters were optimised for each assessment, to ensure that a good quality profile was obtained.

The Plµ system uses a confocal technique to create a 3D profile of the investigated site whilst interferometry is used to check that the sample is level. The technique involves recording the brightness of a defined site (i.e. pixel) at a particular depth. When the pixel is bright (i.e. illuminated), the coordinates are recorded and used to build a topolopical map of the investigated surface. The 3D profile was then resolved, which is where each pixel is connected to its neighbouring pixels to create a smooth surface.

2.2 Static and quasi-static mechanical assessment

The methods used to assess the mechanical behaviour of the investigated materials under static and quasi-static conditions are presented in this section.

2.2.1 Instrumented Indentation testing

There are numerous methods to assess surfaces and coatings to find valuable mechanical descriptors with Instrumented Indentation Testing (IIT). The methods employed have been split into two sections; macro-hardness and fracture toughness. Good instrumented indentation testing assumes that the investigated sample surface is ideally smooth and that the indenter shape is known. Hardness results are often reported in units of pressure (e.g., GPa) which relies on this assumption.

An instrumented indentation records the movement of the indenter during an indentation protocol with respect to a pre-determined reference point. Simultaneously, the normal force exerted by the indenter is recorded. The indenter is loaded according to pre-determined loading rate and held at a set load (load control mode) or indenter penetration depth (depth control mode) for a set time (dwell time). Immediately after

Parameter	Unit	Top surface	Cross section
Indenter	-	Vickers	Vickers
Analysis	-	Martens [100]	Martens [100]
Max. load	N	2.942	2.942
Loading speed	mm/min	0.1	0.1
Dwell time	s	10	10
Unloading speed	mm/min	0.1	0.1

Table 2.1: Vickers macro-hardness test parameters

the dwell time has elapsed, the indenter is unloaded according to a pre-determined unloading rate. With constant monitoring of the normal force and indenter penetration depth, it is possible to investigate material properties which have a time-dependancy, such as creep (ref).

A variety of different methods are available, including the Vickers hardness test [96], Brinell hardness test [97], Shore hardness test [98], Rockwell hardness test [99] and Knoop hardness test [96]. Some methods are favoured by industry (e.g. Rockwell for thin film systems) due to simple test practices. Additionally, IIT may be performed across a wide range of force- and length-scales, depending upon the investigated material. When investigating near-surface volumes, low indentation loads (less than 300mN) are used alongside fine indenters (Berkovich, Cube Corner).

Macro-hardness

Macro-hardness tests were performed with a standard diamond Vickers indenter. The tests were performed in an ambient atmosphere without control of temperature or humidity. An overview of the test parameters is given in Table 2.1. From a Martens analysis [100] of the loading curve, important results including indentation hardness, work and elastic modulus can be found. The Vickers analysis is found according to (ref). Any assessments where the peak penetration depth was greater than 10 % of the coating thickness were discarded.

Fracture toughness

For fracture toughness measurements, IIT was employed. In essence, a Vickers indenter is loaded to promote crack propagation from the vertices of a Vickers indent. The method is helpful when investigating coatings as the instrumented equipment can accurately control the indenter penetration depth, to ensure that the influence of the substrate is minimised.When assessing thermal spray coatings, it is recommended

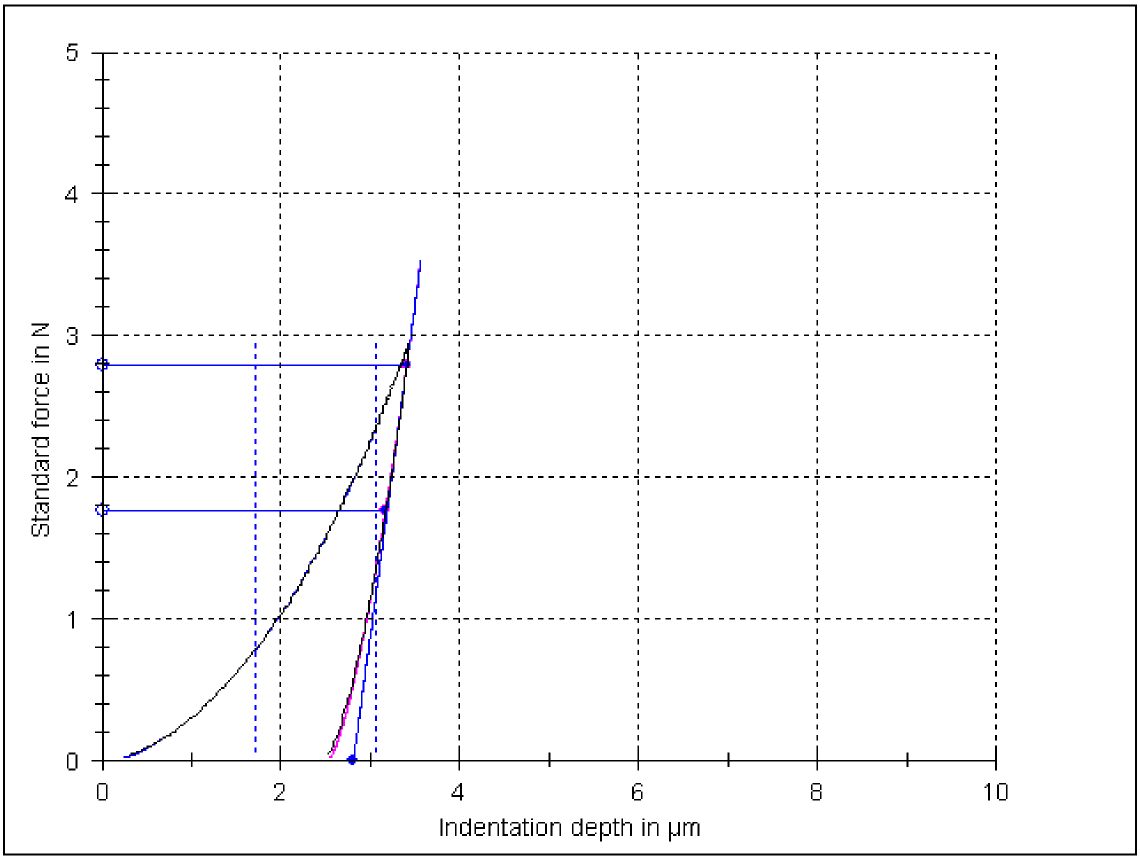

Figure 2.1: Typical loading curve and indent for a Vickers macro-hardness test for a thermal spray WC-CoCr coating

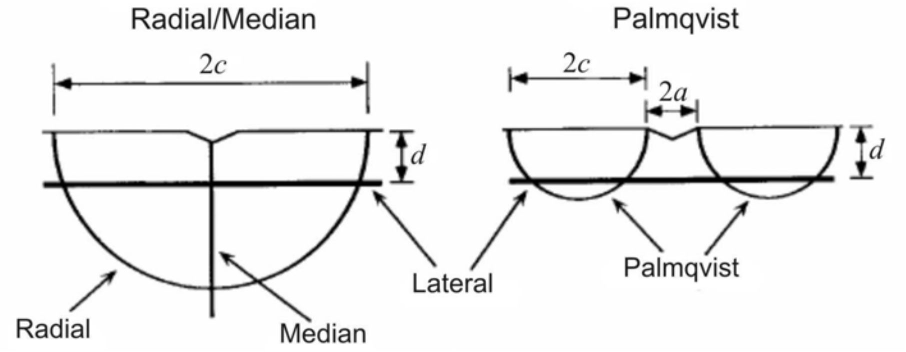

[104]

Figure 2.2: Schematic diagrams of the typical indent and crack patterns for fracture toughness for radial/ median and Palmqvist morphologies, by instrumented indentation testing

to perform indents from the top-surface and from through the cross-section of the coating.

The Evans-Wilshaw method [101] was used to find the fracture toughness by instrumented indentation, KIC. This method is often used as it is based solely on the force, indent size and crack length measurements.The analysis which is presented in Equation 2.1 uses the indentation load, P_{KIC} (mN), average half-indent diagonal, a (µm) and the sum of the average crack length and average half-indent diagonal, c (µm).

$$K_{IC} = 0.079 \left(\frac{P_{KIC}}{a^{1.5}}\right) log \left(\frac{4.5a}{c}\right) \tag{2.4}$$

Numerous other different analyses are available, depending upon the nature of the cracks that are formed. Schematic diagrams of the indents and ideal cracks for both top surface and cross-section tests is given in Figure 2.2. Other methods, such as [102, 103] include material properties such as hardness and elastic modulus which should be measured seperately. A good summary of the analysis methods is available elsewhere [104]. Where results are not available, typical results from the literature are taken. An overview of the test parameters is given in 2.2.

2.3 Tribological test methods

A range of tribological tests were performed which are commonly used in research. The methods are outlined in this section.

Parameter	Unit	Value
Indenter	-	Vickers
Analysis	-	[101, 102]
Max. load	kgf	3 - 30
Loading speed	mm/min	0.1
Dwell time	s	10
Unloading speed	mm/min	0.1

Table 2.2: Fracture toughness by instrumented indentation test parameters

2.3.1 Scratch test

The scratch test method has been used to investigate the adhesion of thin, hard coatings to substrates [105–107]. In most cases, an indenter of defined geometry, material and size is drawn across the investigated surface until failure of the coating or substrate. The test method has been standardised for a range of different materials, including thin ceramic coatings [1], plastics [108, 109] and sprayed ceramic coatings [110]. A schematic of a typical, modern scratch device is given in Figure 2.3. Modern devices are now capable of recording acoustic emissions, normal force through the indenter, tangential (friction) force against the movement of the indenter and indenter penetration. The indenter may be subject to a constant or linearly increasing load. The former is often used to investigate friction behaviour for a given sliding contact condition. The latter is typically used to characterise the load dependancy of critical failure modes. Failures may include through thickness cracking, delamination, cohesive failure and plastic deformation of the coating and/or substrate.

There are a variety of different indenters available for use. Most commonly, a Rockwell C diamond indenter is used due to high symmetry due to a hemispherical tip. However, other shapes are used, including Berkovich, Vickers and large spheres. For most investigations, the indenter material is stiff and harder than that of the coating and/or substrate. This is to minimise deformation of indenter during loading and to maintain shape. As such, indenters are often made of diamond when investigating hard materials, including those tested for this current investigation.

Two devices were used; the CSM µMicro Scratch Combitester (CSM, Switzerland) and the VTT Macro Scratch tester (VTT Oy, Finland). The VTT device is able to test with a maximum load of approximately 100 N, whereas the the CSM device is limited to 30 N. However, the CSM device is more able to control the loading rate, sliding distance and sliding speed due to sophisticated controls. As such, for those materials which needed testing with with a maximum load of no more than 30 N, the CSM

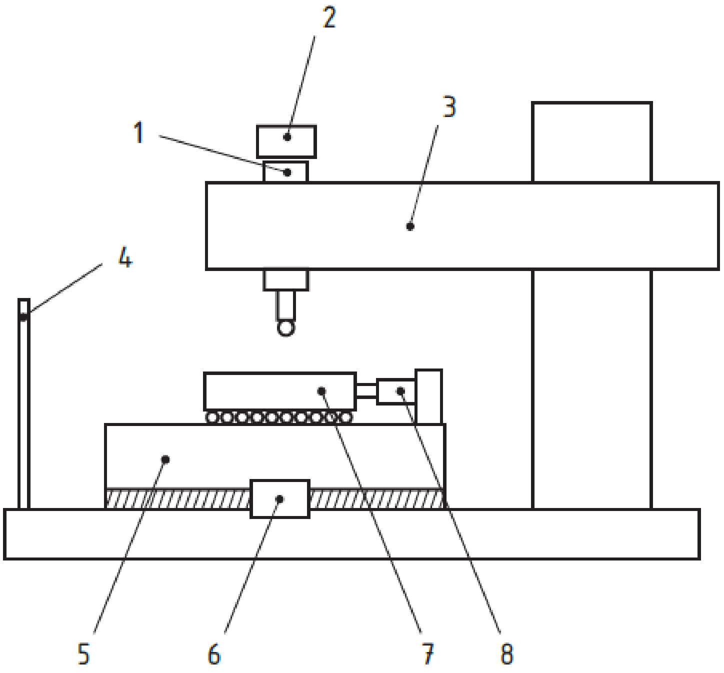

Key

1	Stylus shaft
2	Vertical load transducer
3	Upper support assembly
4	Base reference
5	XY stage to manoeuvre
6	XY stage drive arrangement
7	Low friction sample table
8	Horizontal force transducer

[111]

Figure 2.3: Schematic diagram of a typical, modern scratch test device

device was used. For some tests performed with the VTT device, the maximum load was reduced to 50 N from 100 N. This was done for those coatings which promoted excessive wear of the diamond indenter, leading to heavy cracking and retirement of the indenter. For both devices, a diamond Rockwell C indenter was used, which had a 200 µm radius. Multiple indenters were used as worn/ damaged indenters were retired. An optical microscope image of an indenter which suffered heavy cracking and wear is given in Figure 2.4. The indenters were manufactured to strict quality criteria and assumed to be similar. The sliding direction was constant with respect to the real indenter geometry, in order to minimise the effects of indenter asymmetry. Tests were performed according to BS EN 1071-3:2005 [1]. The test parameters is given in 2.3.

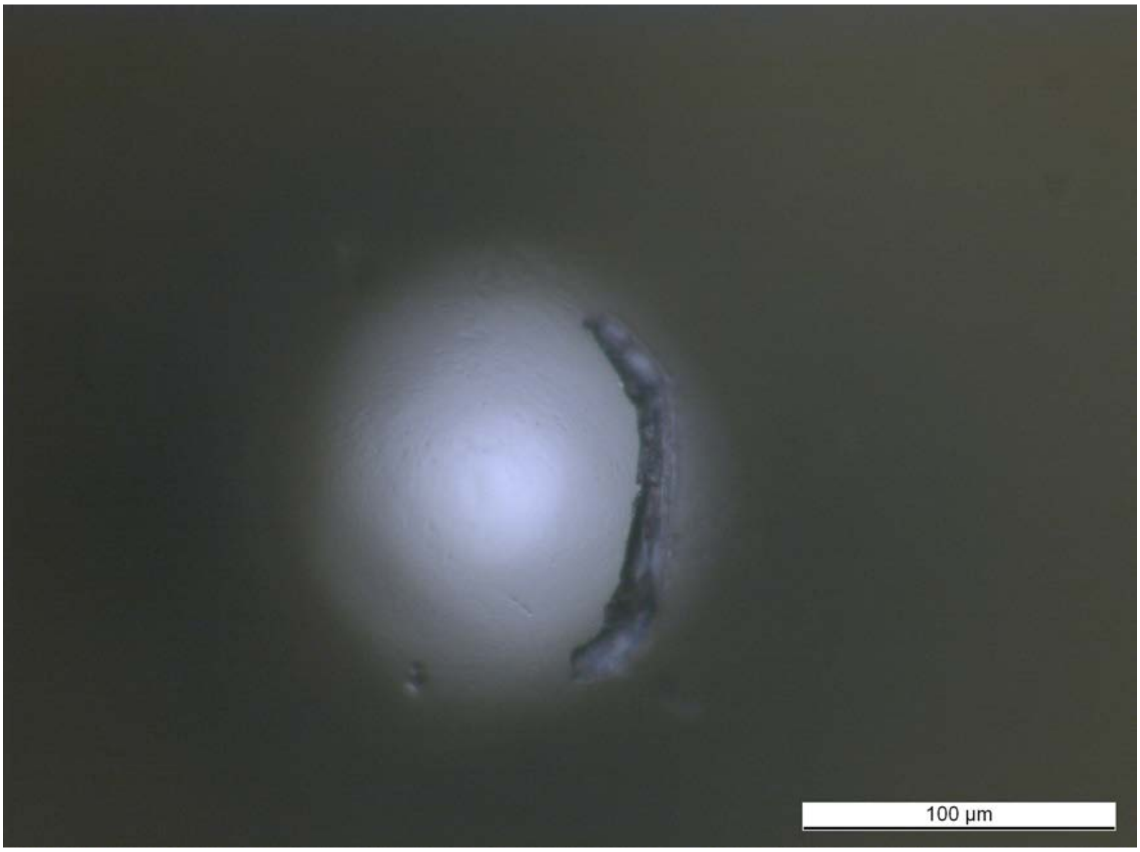

* Note that the sliding was from left to right and that the damaged site was at the leading edge

Figure 2.4: Optical microscope image of a diamond Rockwell C indenter tip which has suffered significant fracture and wear after one scratch against EXP3

The scratch scars were imaged using optical microscopy to record critical failure loads and to qualitively assess failure modes. For a limited number of tests, the scratch

Test parameter	Unit	CSM	VTT 1	VTT 2
Equipment	-	CSM	VTT	VTT
Stylus geometry	-	Rockwell C	Rockwell C	Rockwell C
Stylus radius	µm	200	200	200
Minimum load	N	0.050	2 *	5 *
Maximum load	N	30	100 *	50 *
Sliding distance	mm	10	10 *	10 *
Sliding speed	mm/min	10	10	10
Loading rate	N/mm	2.995	10 *	5 *
Air temperature	°C	22±1	22±1	22±1
Relative humidity	%	50±5	50±5	50±5

*Please note that these parameters varied slightly, in accordance with normal operation of the device.

Table 2.3: Scratch test parameters

scars were assessed with optical 3D profilometry.

2.3.2 Percussive normal impact

Percussive normal impact testing was performed at a number of sites. Low load impact tests were performed with the Pneumatic Impactor at the University of Sheffield. The test parameters is given in Table 2.4. High load impact tests were performed at two sites. The trial tests were performed with the IonCoat I 10 impactor at Cutting and Wear UK Ltd, Rotherham. The remainder were performed with the IonCoat I 10 impactor at Caterpillar Inc., Peoria, Illinois, USA. The test parameters is given in Table 2.5. All tests were performed under ambient conditions where temperature and humidity were not actively controlled. For both cases, the counterface was a fixed WC-Co ball of 6 mm diameter and roughness complying to Grade G10 of ISO 3290-2 [112].

Parameter	Unit	Low load
Peak load	N	100
Impact frequency	Hz	8-10
Air gap	mm	15
Number of impact cycles	'000	0.1, 1, 2.5, 5, 10, 20, 35, 50

Table 2.4: Low load percussive normal impact test parameters

Parameter	Unit	High load
Peak load	N	1800
Impact frequency	Hz	55
Air gap	mm	0.25
Number of impact cycles	'000	0.1, 1, 2.5, 5, 10, 20, 50, 100, 250

Table 2.5: High load percussive normal impact test parameters

2.3.3 Compound impact

The compound impact tests were performed with the High Velocity Particle Impactor (HVPI) apparatus [45, 113]. A projectile is accelerated towards the target specimen, which is set to an impact angle between 0 and 90º. Due to high deformation of the impact specimen surface, sliding of the projectile is often observed. As such, the nature of the impact contact is compound angled-sliding-impact, i.e. a combination of Figures 1.1b and 1.1c. The test parameters are given in Table 2.6.

Parameter	Unit	Value
Impact angle	°	30
Air pressure	Bar	1.9 - 9
Projectile diameter	mm	9
Projectile mass	g	3
Projectile material	-	100Cr6 steel [114]
Roughness [ISO]	-	G10

Table 2.6: Single compound sliding impact test parameters

The equipment consists of a 9mm smooth bore (firearm barrel without helical grooves cut into the barrel walls) with a length of 550 mm. The projectile velocity can be controlled through adjusting the air pressure of the gas tank prior to firing, which can range between 0.1 and 16 Bar. Various projectiles can be used; including metallic balls, ceramic balls, rock particles and non-spherical particles (e.g. bullet heads). By adjusting the mass and velocity of the projectile, a wide range of impact energies can be acheived.

The projectile velocity is measured with a commercial chronograph and the measured velocity varied slightly for a given air pressure. The relationship between air pressure and projectile velocity is shown in Figure 2.5. The variance may arise from slight differences in projectile shape and size leading to resistance against the barrel walls when fired, as well variation of real pressure control.

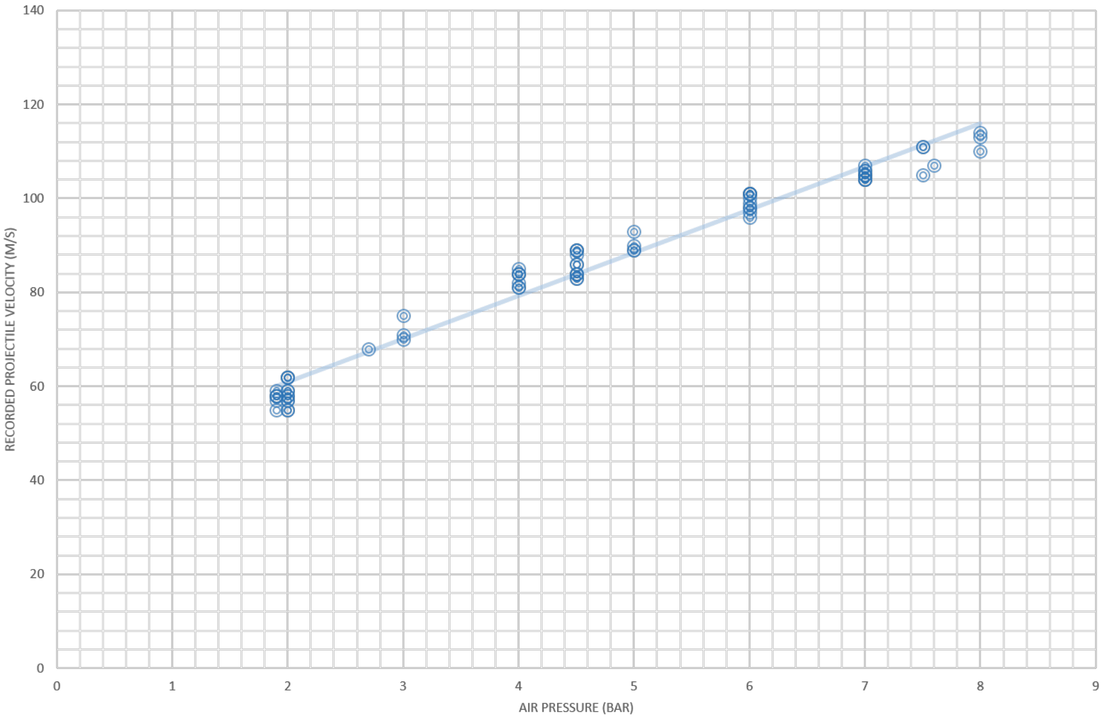

Figure 2.5: Relationship between air pressure and projectile velocity, for a 3g 100Cr6 steel ball

The target sample is fixed to a stiff sample holder which is assumed to be rigid, 1 m from the end of the barrel. The sample can be tilted from 0 to 90°. In order to preserve samples, the number of individual impact events against the sample is maximised; between 2 and 8 impacts were applied per sample. The number of impacts was maximum when the projectiles were accurately fired and that the impact-damaged area was small. Where possible, all impact sites did not overlap their impact craters or visible crack networks. All tests were performed under ambient conditions where temperature and humidity are not actively controlled. The impact events were monitored with high frame rate cameras. A limited number of tests also had a triaxial force sensor to record impact forces underneath the sample.

2.3.4 Erosion test

The erosion tests were performed with the erosion test device at Technical University of Tampere, Finland. The equipment is a centrifugal accelerator device which is similar to the device presented by Kleis [115, 116], as shown in a schematic drawing in Figure 2.6.

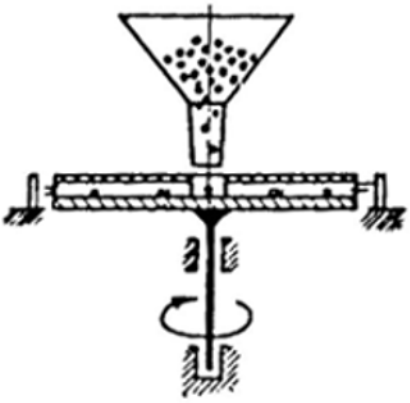

[115, 116]

Figure 2.6: Schematic drawing of the erosion test equipment

Erosion is achieved by accellerating a known amount of erosive media at 15 samples, orientated at an impingement angle between 15 and 90º. The erosive media was quartz. The average particle impact velocity was set between 25 and 80 m/s. The test parameters are given in Table 2.7.

Parameter	Unit	Value
Impact angle	º	30, 60 or 90
Average particle velocity	m/s	25, 50 or 80
Erosive media mass	kg	6

Table 2.7: Erosion test parameters

Three tests were performed for each combination of impact angle and average particle velocity. For each individual test, a new and untested sample was used. Each test sample was weighed before and after testing, with the difference used to describe wear as a function of mass loss. The samples were observed by eye for substrate exposure. The worn surfaces were inspected with SEM to establish wear mechanisms under erosive conditions.

Chapter 3

Materials

3.1 Introduction

A variety of different materials were selected for this work. This is, in part, due to consideration paid to the wider supporting projects and framework at VTT looking to strengthen local industry. As such, coatings from a Finnish supplier were tested alongside experimental thick and thin films.

3.2 Summary of materials

3.2.1 Commercial coatings

Three thick coated samples were sourced from Fincoat Oy, Riihimäki, Finland. Their base compositions, as-sprayed thickness and spray method are given in Table 3.1. The coatings were sprayed onto 40 mm x 50 mm x 9 mm rectangular coupons of Uddeholm Formax steel. As these are from a commercial supplier, information related to spray process deposition parameters or powder characterisation are not available. The mechanical properties are given in Table 3.9. COMM1 was chosen as CrC-NiCr-based materials are commonly used to coat the suspension stanchtions of large mining equipment due to good fracture toughness and tribological behaviour. COMM2 was chosen as Tungsten Carbide-Cobalt coatings are commonly used for sliding wear protection due to high hardness. COMM3 was chosen as Molybdenum Boride based coatings generally exhibit good sliding wear resistance. The HVAF processing technique was chosen as the method is gaining popularity with industry due to low spray temperatures and high particle velocity giving dense, hard coatings with morphology similiar to that of the original feedstock material.

Sample code	Base Composition (wt%)	As-sprayed thickness (µm)	Spray technique	Key characteristic
COMM1	CrC-25NiCr	300	HVAF	LT
COMM2	WC-10Co4Cr	300	HVAF	LT
COMM3	MoB-CoCr	300	HVAF	LT

* Please note that the key characteristic, LT, denotes “low temperature” spray process

Table 3.1: Summary of commercial coatings specification

3.2.2 New experimental coatings

Three thick coatings were sprayed using three different thermal spray processes using typical process parameters. A summary of the process parameters is given in 3.4.The aim was to assess the impact and sliding wear response of coatings made by each process. The composition, thickness, substrate material and average carbide size were kept constant, as shown in 3.2. The mechanical properties are given in Table 3.9. The base composition was set as WC-10Co4Cr as this is commonly used in research and industry, demonstrating high hardness and reasonable fracture toughness. Additionally, it is possible to spray this material with multiple spray methods (HVOF, HVAF) and different nozzles when the powder particle size distribution is slightly modified.

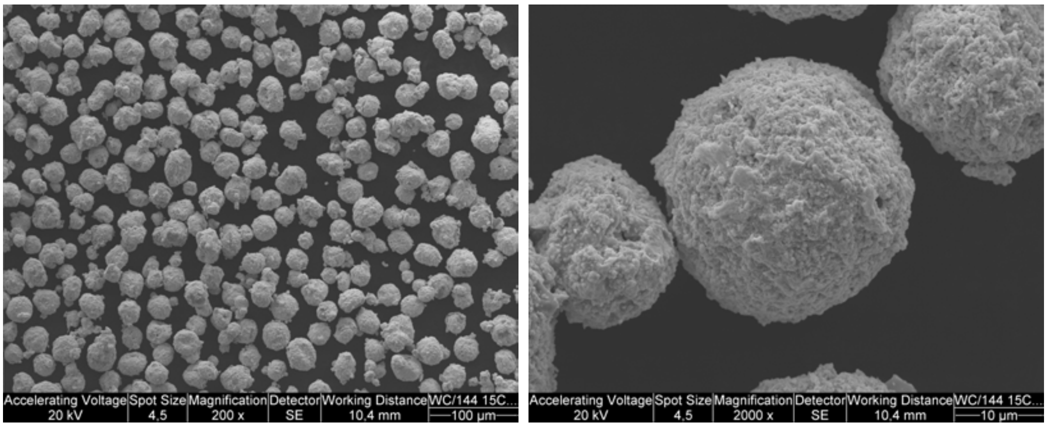

Figure 3.1: SEM images of WC-144 powder

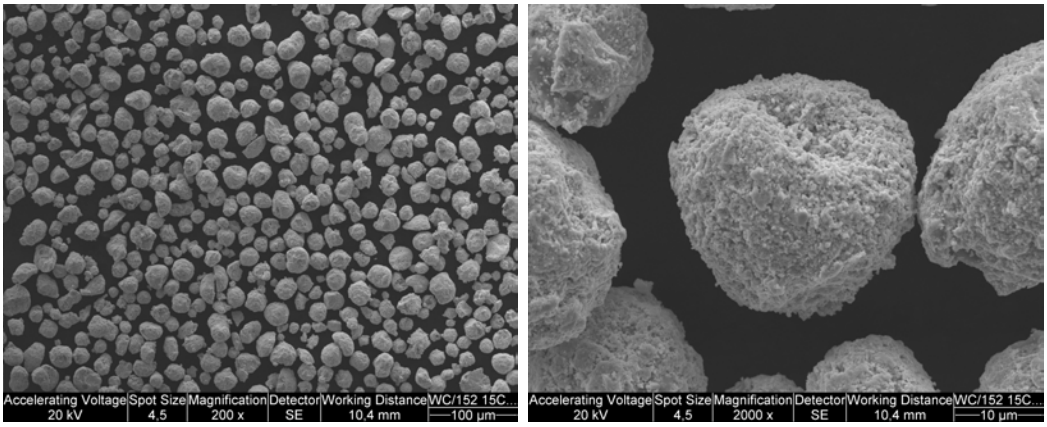

Figure 3.2: SEM images of WC-152 powder

Two commercial powders were used. SEM images of the unsprayed powders are given in Figures 3.1 and 3.2. Note that WC\152 is regarded as similar to WC\153 having the same company specification but from a different batch. As such the powder images of WC\152 shown in Figure 3.2 are representative of WC\153 of Table 3.2.

3.2.3 Advanced composite multilayer coating

A hybrid process, multilayer coating based on a hard, thin film coating applied to a thick, thermal spray carbide coating was developed. The thin film was developed by Dr. Lawrence Li, City University of Hong Kong. A summary of the mechanical properties and performance of the same thin film coatings on M2 steel substrates is presented in Table 3.5 [117]. The thin film included a DLC top coat, a Chromium-Carbon gradient layer and a metallic Chromium bond coat.

Sample code	Base composition (wt%)	As-sprayed thickness (µm)	Spray technique	Spray gun	Key characteristic
EXP1	WC-10Co4Cr	300	HVOF	DJ-H	HT, LV
EXP2	WC-10Co4Cr	300	HVOF	CJS	MT, MV
EXP3	WC-10Co4Cr	300	HVAF	Kermetico	LT, HV
EXP4	EXP2 + DLC	300	HVOF/PVD	Assorted	-

* Please note that for the key characteristics: LT, MT and HT denote low, medium and high temperature spray process. LV, MV and HV denote low, medium and high average spray particle velocity.

Table 3.2: Summary of experimental coatings specification

Process	-	EXP1	EXP2	EXP3
	Units			
Powder manufacturer	-	Durmat	Durmat	Durmat
Company code	-	135.063	135.017	135.017
VTT internal code	-	WC\144	WC\153	WC\153
Morphology	-	Agglomerated, sintered	Agglomerated, sintered	Agglomerated, sintered
Composition	wt%	WC-10Co4Cr	WC-10Co4Cr	WC-10Co4Cr
Average carbide size	µm	0.4	0.4	0.4
Particle size distribution	µm	15 - 36	5 - 25	5 - 25

Table 3.3: Powder materials for new experimental coatings

Process	-	EXP1	EXP2	EXP3
	Units			
H_2 flow rate	l/min	635	80	35%
C_3H_8 flow rate	l/min	-	16	75 psi
Kerosene	Bar	-	15	-
O_2 flow rate	l/min	215	940	-
N_2 flow rate	l/min	14	16+16	35%
Air flow rate		350 l/min	-	94 psi
As-sprayed thickness	µm	> 260	> 260	> 260
Powder feed	g/min	40 - 50	65	85 - 90
Stand off	mm	230	200	250
Pass distance	mm	3	3	4

Table 3.4: Thermal spray process parameters for the new experimental coatings

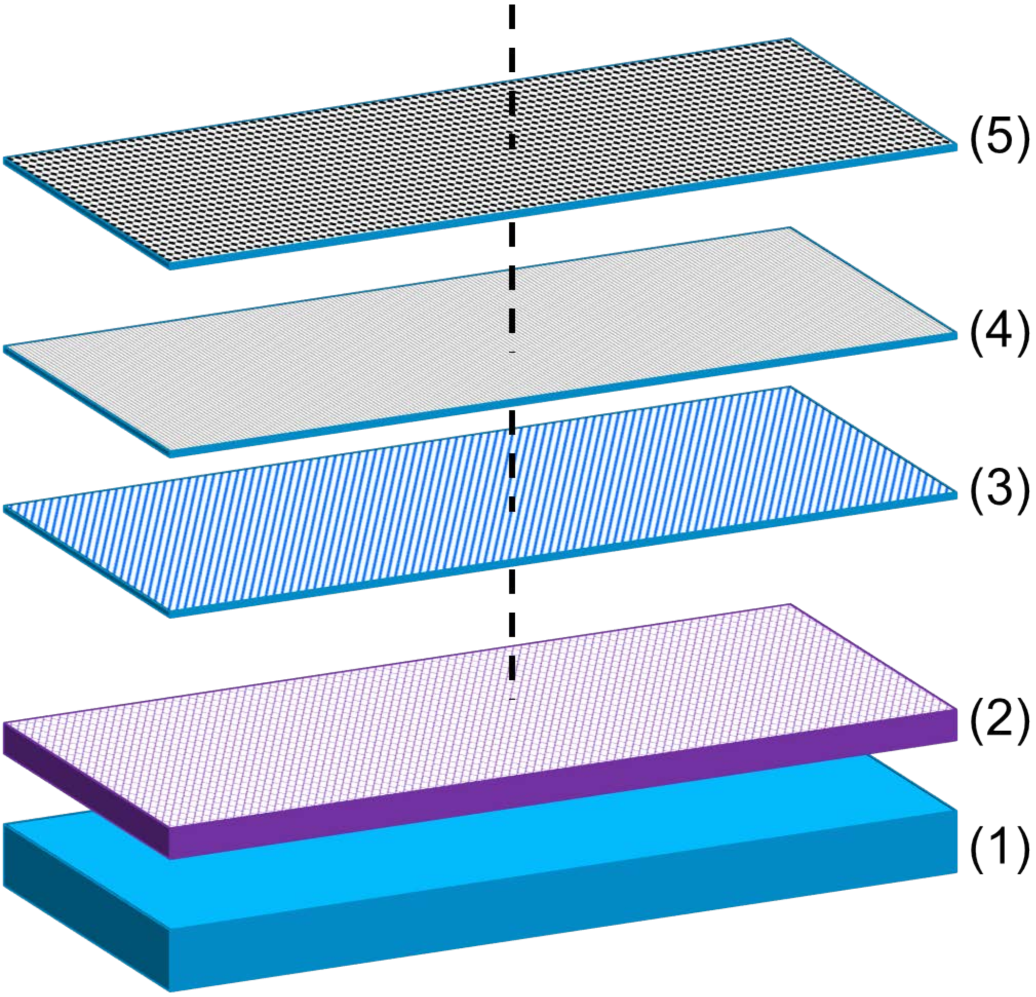

*Note that the individual layers are comprised of a 9 mm thick, Uddeholm Formax steel substrate (1), 250-300 µm thick EXP2 thermal spray coating (2), 0.4 µm thick Chromium bond coat (3), 0.2 µm thick CrxCy gradient layer (4) and 1.1 µm thick, amorphous, hydrogen-free DLC layer (5)

Figure 3.3: Schematic drawing of hybrid process, multilayer coating (EXP4).

The DLC layer had an amorphous, hydrogen-free structure. In order to maintain consistency with regards to impact deformation, Uddeholm Formax coupons with dimensions of 40 mm x 50 mm x 9 mm were used as the primary substrate. The secondary substrate (coating layer 1) is the same as EXP2 (see Section 3.2.2). The TS coating top surface was ground and polished to a mirror finish prior to the deposition of the thin films.

Parameter	Symbol	Unit	Value	Ref.
DLC Hardness	H_{IT}	GPa	18 ± 1.3	[117]
DLC Indentation Modulus	E_{IT}	GPa	205 ± 10	[117]
DLC Poisson#'s ratio	ν	-	0.202	[117]
DLC thickness	t	μm	1.11	[117]
Buffer+gradient+CrCx thickness	t	μm	0.63	[117]
Substrate Hardness	H_{IT}	GPa	6.3 ± 0.06	-
Substrate Indentation Modulus	E_{IT}	GPa	220 ± 13	-
Substrate Poisson's ratio	ν	-	0.3	

[117]

Table 3.5: Properties and performance of the reference DLC multilayer coating developed by Li

The DLC coatings were deposited by closed-field unbalanced magnetron sputtering [118, 119]. A commercially available UDP650/6 magnetron sputtering system comprising six rectangular cathodes (2 Chromium and 4 graphite targets) was used. The target configuration was arranged to be Cr-C-C-Cr-C-C, located symetrically around the vacuum chamber [120]. Prior to deposition, the chamber was evacuated to a background pressure less than 0.4 mPa. The Ar working gas pressure was kept at 170 mPa by flow rate control during sputtering. The equipment was furnished with a rotating substrate holder at a speed of 10 rpm. The substrate was biased with pulse DC at a frequency of 250 kHz. The target-to-substrate distance was 17 cm [117].

The deposition process of the DLC coatings comprised four major steps; plasma ion cleaning, adhesive layer, compositionally graded layer and pure carbon top layer deposition. In order to remove the oxide layer or other contaminants from the surface, the substrates were sputter cleaned with Ar plasma at a bias voltage of -450 V for 30 minutes in the first stage. After that, an adhesive Cr layer was prepared followed by a CrCx graded layer for load support. Finally, the DLC top layer was produced by only sputtering the graphite targets which had a purity greater than 99.999% [117].

Processing parameter	Unit	Value
Deposition method	-	Magnetron sputtering PVD
DLC structure	-	a-C
Background pressure	mPa	0.4
Ar working gas pressure	mPa	170
Substrate temperature	°C	200
Bias voltage - Ar plasma cleaning	V	-450
Bias voltage - deposition	V	-60
Target rotation speed	rpm	10
Target-to-substrate distance	cm	17
Deposition rate - Cr	nm/min	20
Deposition rate - CrCx	nm/min	18
Deposition rate - DLC	nm/min	10

Table 3.6: Processing parameters for thin film DLC deposition by PVD

The CrCx graded layer was incorporated to assist with the accommodation of stresses and thus reduce micro-cracking [120]. It has been reported that the mechanical properties of DLC films can be varied in a controllable manner by selecting appropriate deposition parameters such as bias voltage, which largely determines the energy of ions bombarding the growing film surface [120]. A constant bias voltage was applied during the whole DLC deposition process. The deposition rates are given in Table 3.6 [117].

3.2.4 Reference steel substrates

Uddeholm Formax was used as the substrate materials for all samples, except for the erosion tests . Uddeholm Formax steel was supplied in the hot-rolled and machined condition, with a hardness of 170 HB. For the erosion tests, Böhler K490 coupons were used. See Table 3.7 for information on their specified composition.

Element	Unit	Uddeholm Formax	Bohler K490
C	wt%	0.18	1.4
Si	wt%	0.3	-
Mn	wt%	1.4	-
Cr	wt%	-	6.4
Mo	wt%	-	1.5
V	wt%	-	3.7
W	wt%	-	3.5
Fe	-	Balance	Balance

Table 3.7: Typical elemental composition for the commercially sourced substrate materials

3.2.5 Counterface materials

A variety of different counterfaces were used, depending upon the investigation. For the percussive normal impact tests, a WC-Co ball was used and supplied by Spherotech GmbH., Germany. The ball had a 6 mm diameter and a roughness complying to Grade G10 of ISO 3290-2 [112]. For the single compound sliding impact test, a 9 mm diameter 100Cr6 ball was used, with roughness complying to Grade G28 of IS0 3290-2 [112]. For the ball-on-disc tests, an alumina ball with a 10 mm diameter was used. This was sourced from Spherotech GmbH. and the roughness complied with Grade G10 of ISO 3290-2[112]. For, the indentation and scratch tests, an appropriate sharp diamond stylus was used. These were sourced from ST Instruments, The Netherlands and Mössner GmbH, Germany.

3.3 Characterisation of materials

3.3.1 Surface roughness

The investigated surfaces were ground and then polished to an average roughness, Ra, of less than 0.1 µm. The roughness values were obtained as described in Section 2.1.1.

3.3.2 Coating composition by Xray Diffraction analysis

The coatings were assessed with Xray Diffraction analysis , as described in Section 2.1.2. The diffraction spectra are presented for materials EXP1, EXP2, EXP3, COMM1, COMM2 and COMM3.

COMM1

The base composition for COMM1 was specified as 25NiCr-CrC. An XRD spectrum for COMM1 is given in Figure 3.4. The spectrum indicates the presence of Nickel (Ni) and of two Chromium Carbides; Tongbaite (Cr_3C_2) and Cr_7C_3.

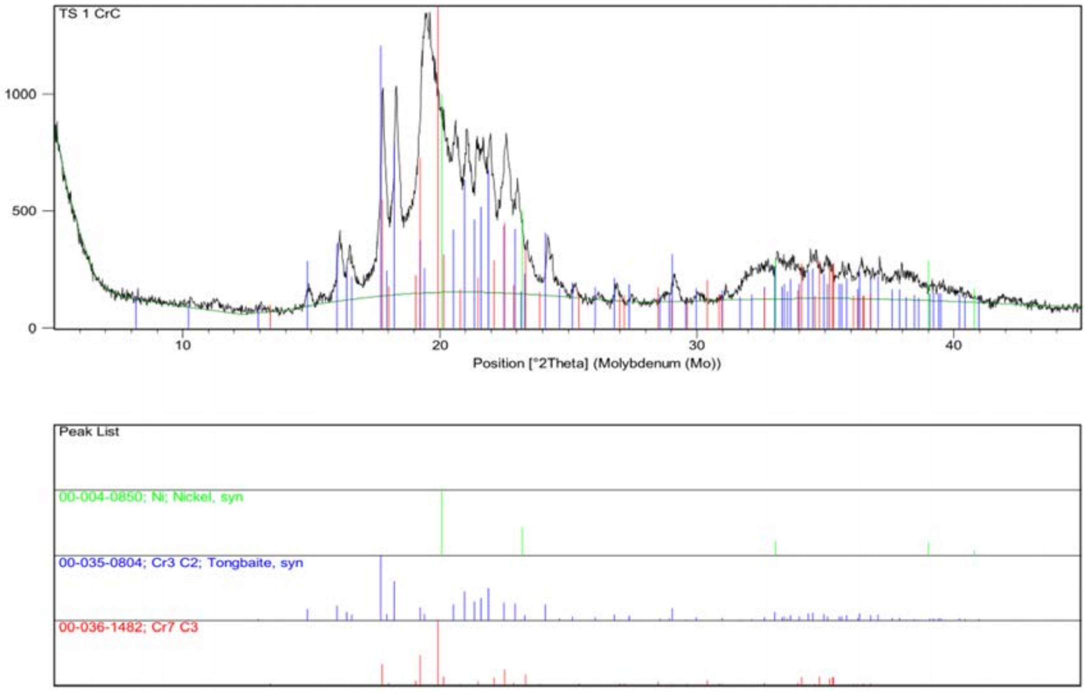

Figure 3.4: XRD spectrum for COMM1

COMM2

The base composition for COMM2 was specified as WC-10Co4Cr, which is the same as for EXP1, EXP2 and EXP3. An XRD spectrum for COMM2 is given in Figure 3.5. The spectrum indicates the presence of Tungsten Carbide (WC), Tungsten Semi-Carbide (W_2C) and a Tungsten-Cobalt-Carbon compound (W_3Co_3C). As the spraying process is a low temperature process, it is suspected that WC and W_3Co_3C originate from the powder forming process rather than the spray process. As such, their content could be minimised through better powder production methods.

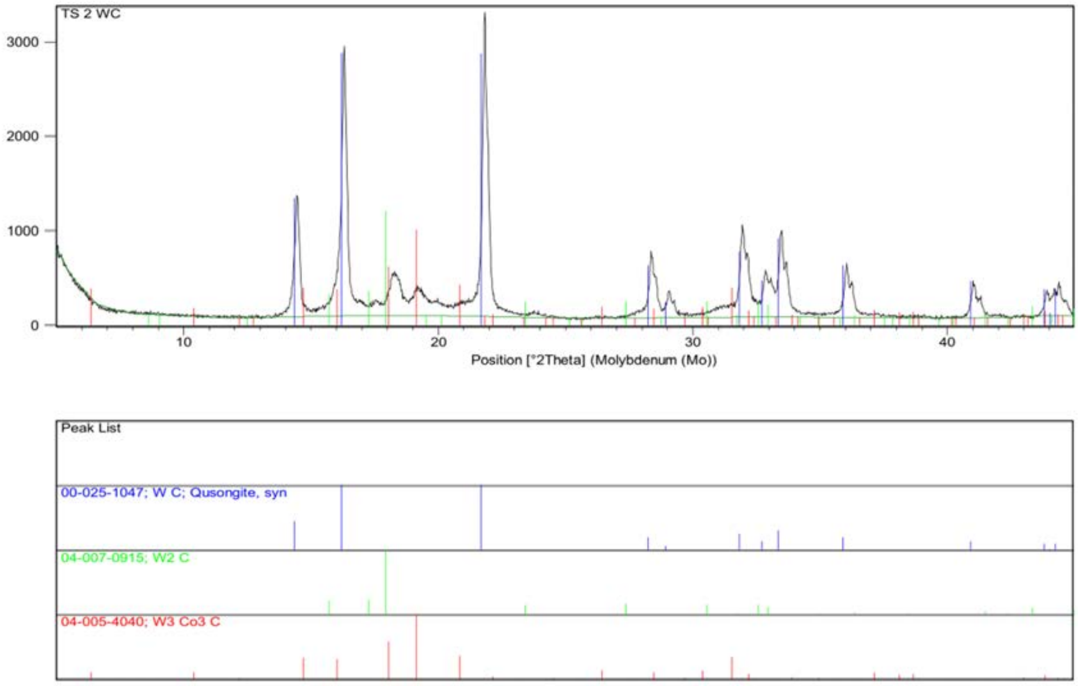

Figure 3.5: XRD spectrum for COMM2

COMM3

The exact base composition of COMM3 is unknown to the author as the coating manufacturer does not provide the information. XRD analysis has shown that the coating is formed from Molybdenum, Cobalt and Boron. An XRD spectrum is shown in Figure 3.6. The spectrum indicates the detection of Cobalt (Co), Molybdenum Boride (MoB) and a Cobalt-Molybdenum-Boron compound ($CoMo_2B_2$). Additionally, the peaks are not all well defined, due to a suspected high amorphous content.

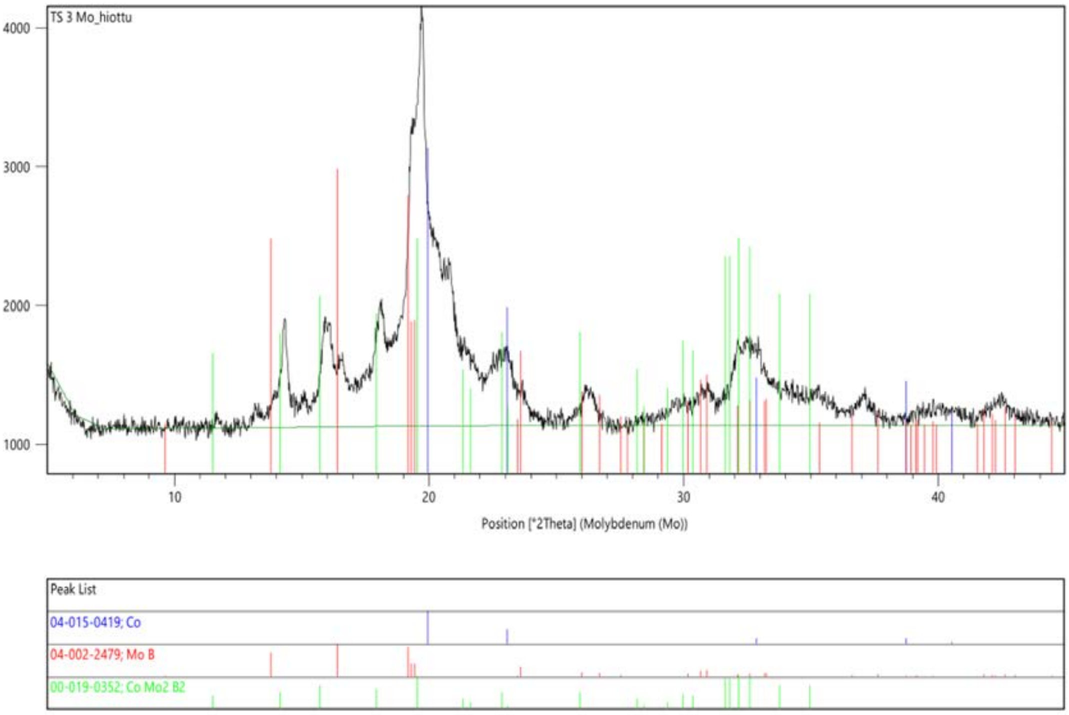

Figure 3.6: XRD spectrum for COMM3

From private communication with Tomi Suhonen, VTT, on the composition of the coating, it is suspected that the coating is features various Molybdenum Borides in a Cobalt-Chromium binder matrix (MoB-CoCr) [121]. The estimated contents of each element are given in Table 3.8.

Element	Unit	Estimated weight percentage
B	wt%	8.0 - 8.5
Co	wt%	25.0 - 28.0
Cr	wt%	13.5 - 15.0
Mo	-	Balance

Table 3.8: Estimated elemental content by weight percentage for COMM3

EXP1

The base composition of EXP1 is WC-10Co4Cr, with Tungsten-Carbon based Carbides and a Cobalt-Chromium-Carbon based binder matrix volume. An XRD spectrum is presented in Figure 3.7

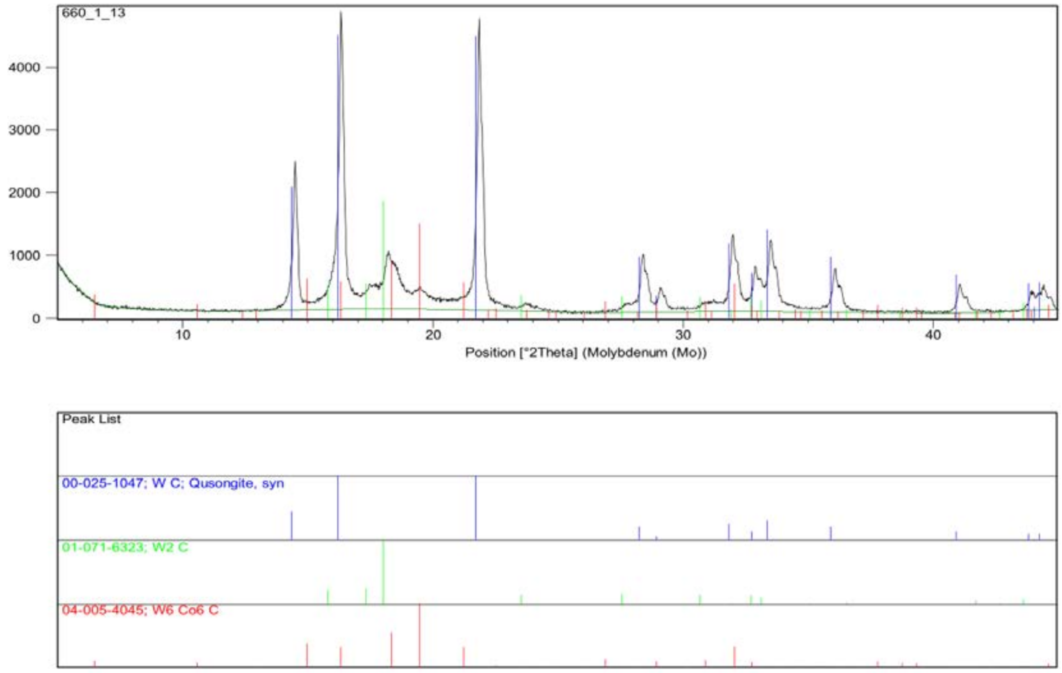

Figure 3.7: XRD spectrum for EXP1

From XRD analysis, Tungsten Carbide (WC), Tungsten Semi-Carbide (W_2C) and Tungsten-Cobalt-Carbon compound, η-carbide, (W_6Co_6C) was detected. The presence of W_2C and W_6Co_6C is expected to have formed as a result of the spraying process due to high temperatures permitting diffusion of carbon from the carbide to the metal matrix binder volume.

EXP2

The base composition of EXP1 is WC-10Co4Cr, with Tungsten-Carbon based Carbides and a Cobalt-Chromium-Carbon based binder matrix volume. An XRD spectrum is presented in Figure 3.8.

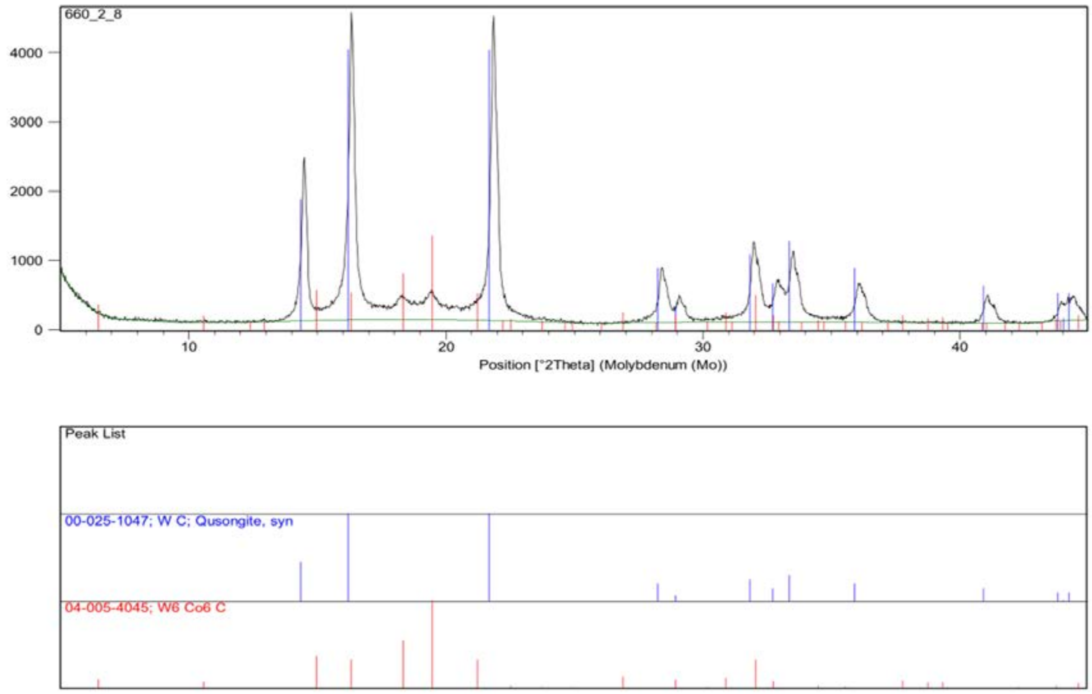

Figure 3.8: XRD spectrum for EXP2

From XRD analysis, Tungsten Carbide (WC) and Tungsten-Cobalt-Carbon compound, η-carbide, (W_6Co_6C) was detected. The presence of W_6Co_6C is expected to have formed as a result of the spraying process due to high temperatures permitting diffusion of carbon from the carbide to the metal matrix binder volume.

EXP3

XRD analysis was not performed for EXP3 as the spray temperatures should not be sufficient for carbide degradation to occur. As such, the XRD spectrum is expected to be similar to that EXP2.

EXP4

XRD analysis was not performed for EXP4, as the steel substrate and thermal spray metal carbide volumes are identical to that of EXP2. The thin film multilayer was assessed by other means, as shown in Section 3.3.3.

3.3.3 Microstructure

Each investigated material was subject to SEM imaging to define key microstructural features, including pores, cracks, matrix volumes and carbides. The microstructural images are presented in 3.3.3. Important statistical descriptors such as mean free path, average carbide diameter and carbide aspect ratio are presented in Table 3.11.

COMM1

The microstructure of COMM1 through the coating cross-section can be observed in Figure3.9. The coating has bonded well to the substrate with no cracking or excessive porosity along the steel-coating interface at the bottom. Within the coating, carbide and matrix volume are visible and can be distinguished. The carbides are dark grey, the matrix volume is light grey whilst any porosity and cracking appear black. The resin binder at the top of Figure 3.9 appears black.

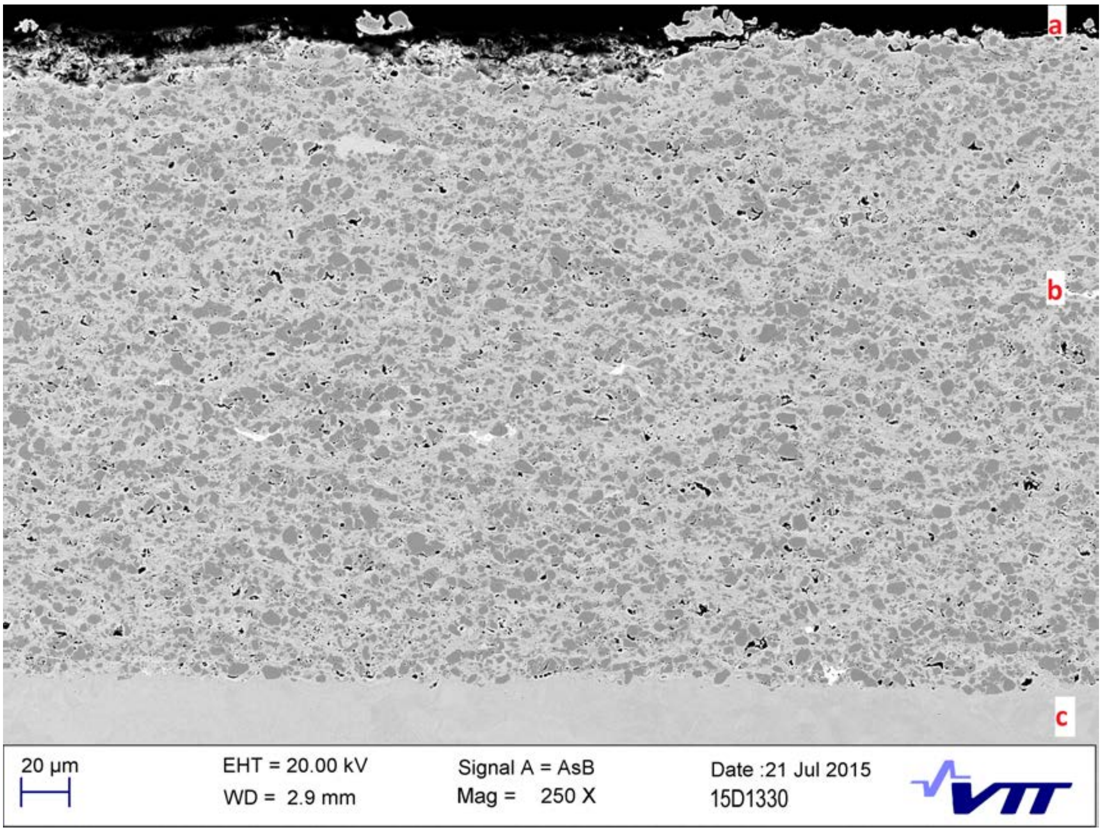

*Note that the features labelled ’a’, ’b’ and ’c’ are the resin binder, coating and substrate volumes respectively

Figure 3.9: An annotated SEM image of the microstructure of COMM1 through the coating thickness

The carbides are angular with some rounded edges, as shown in Figure3.10. As a result of local compositional variation in the matrix, it is possible to observe multiple matrix phases. Some carbides have fractured internally, which may reduce the ability of the carbide to support loading. Such features may weaken the material when compared to a ideal coating.

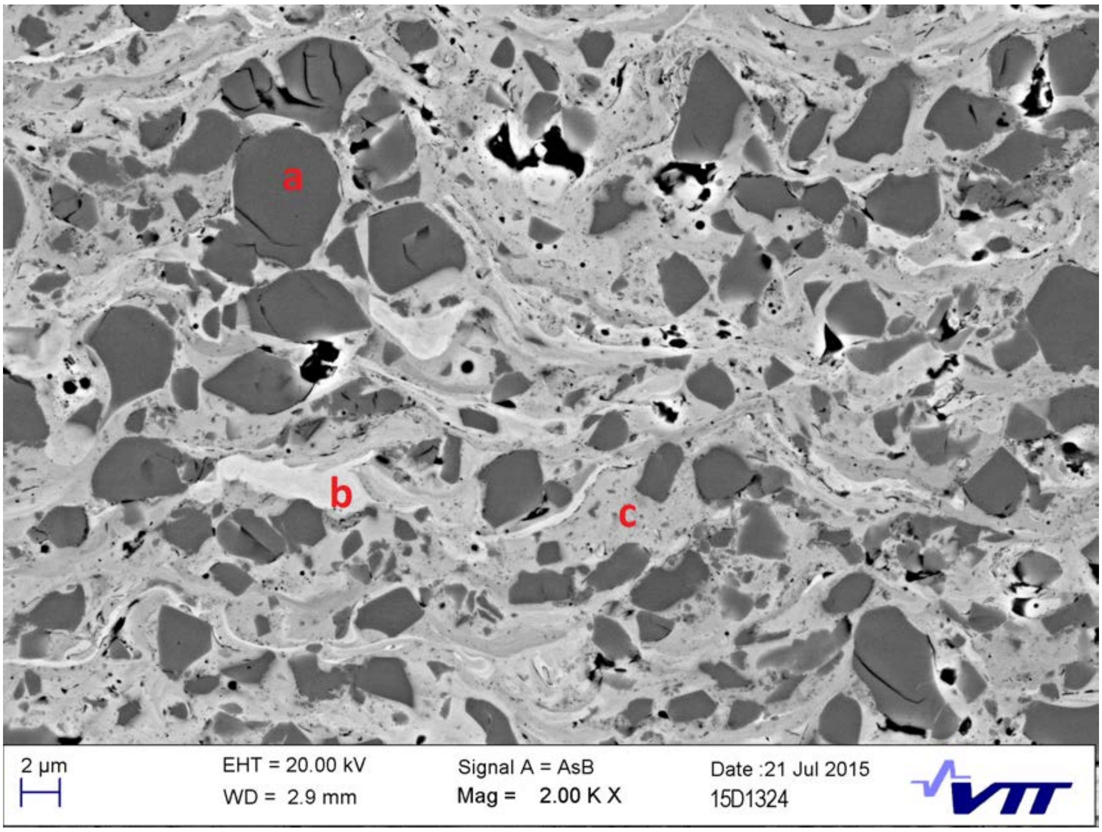

*Note that the features labelled ’a’, ’b’ and ’c’ show examples of the carbide, matrix phase 1 and matrix phase 2 volumes respectively

Figure 3.10: An annotated SEM image of the microstructure of COMM1 through the coating thickness

At higher resolution, matrix-carbide interface fractures are observed, as seen in Figure3.11. Without good local bond strength between carbide and the surrounding matrix, wear by carbide ejection may be accelerated. Microporisity is also observed in the matrix but not in the carbides.

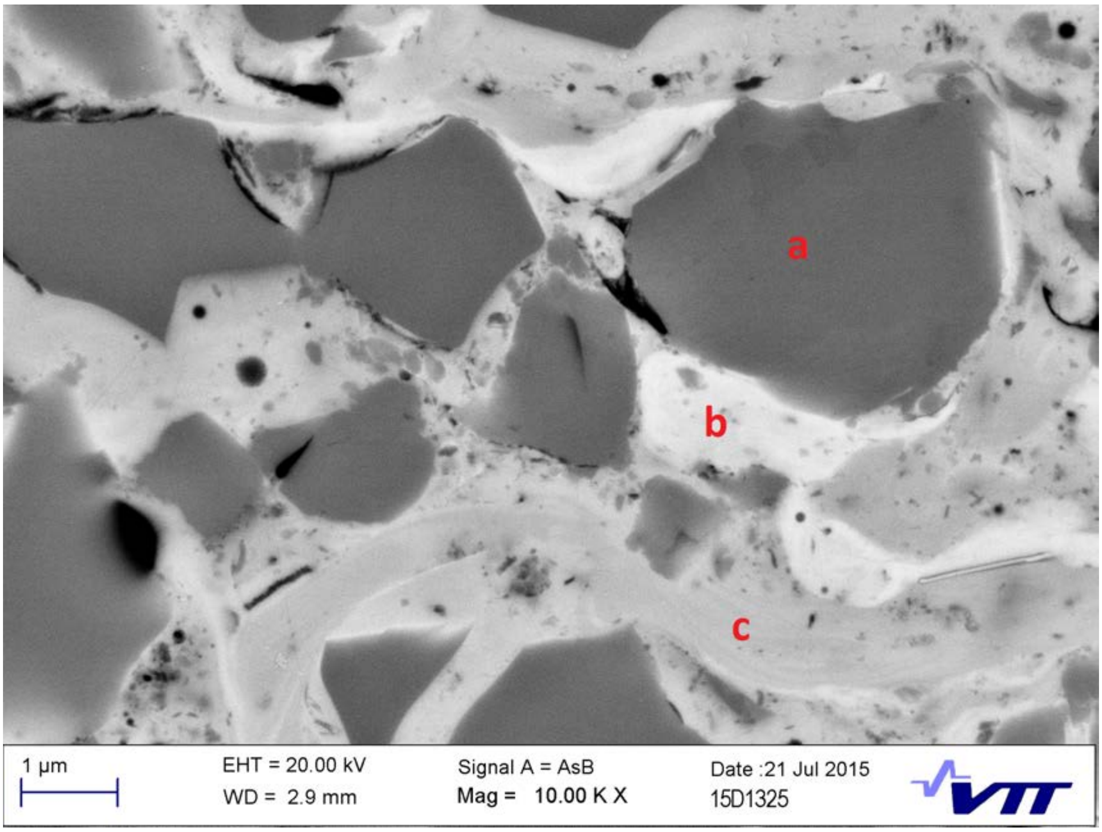

*Note that the features labelled 'a', 'b' and 'c' show examples of the carbide, matrix phase 1 and matrix phase 2 volumes respectively

Figure 3.11: An annotated SEM image of the microstructure of COMM1 through the coating thickness, showing carbide and matrix volumes

COMM2

A through-thickness cross-sectional SEM image of COMM2 is given in Figure 3.12. The coating is steel substrate is dark grey whilst the coating is dark grey. Porosity, cracking and the resin binder (at the top) appear black. The coating appears well adhered to the substrate with no observed cracking or excessive porosity at the coating-substrate interface. Cracking is observed along the resin-coating interface, which is due to excessive loading during the sample preparation stages.

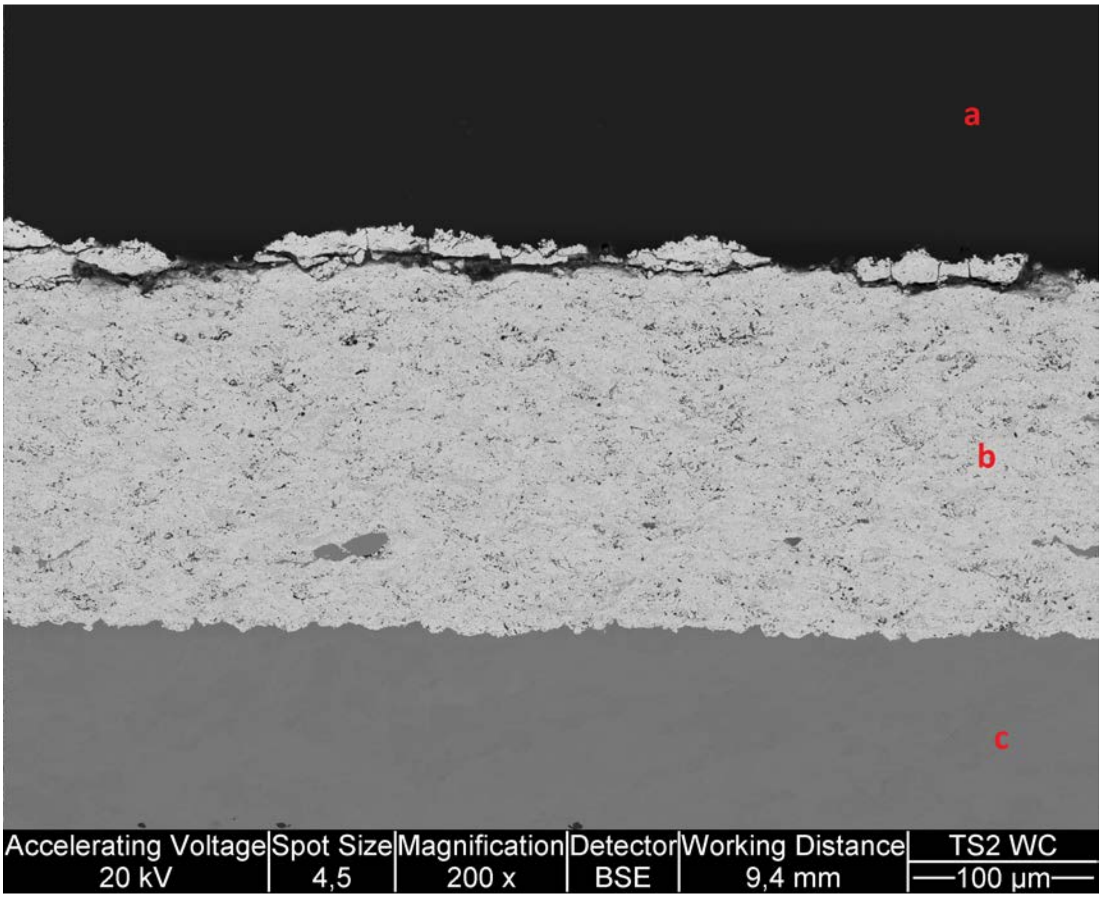

*Note that the features labelled ’a’, ’b’ and ’c’ are the resin binder, coating and substrate volumes respectively

Figure 3.12: An annotated SEM image of the microstructure of COMM2, through the cross-section of the coating

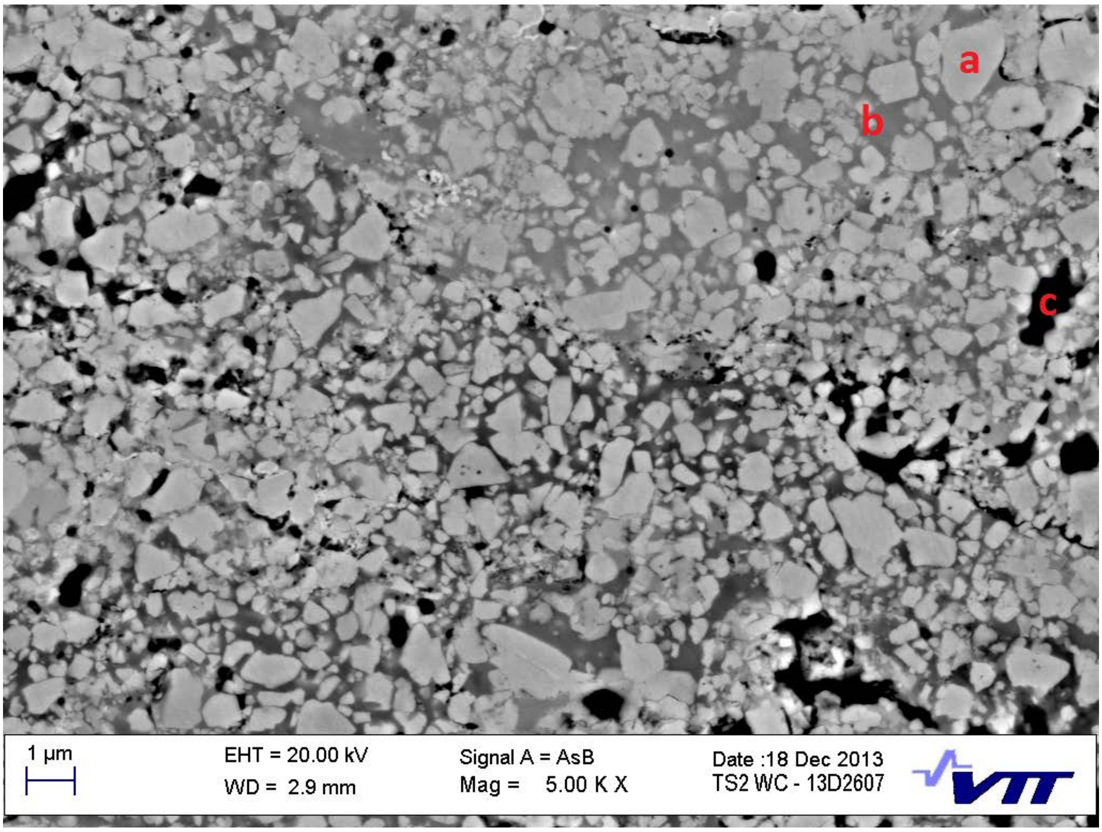

*Note that the features labelled 'a', 'b' and 'c' show examples of the carbide, matrix and pore volumes respectively

Figure 3.13: An annotated SEM image of the microstructure of COMM2, through the cross-section of the coating

When observed at higher magnification, it is possible to see splat boundaries, individual carbides, porosity and matrix volumes, as seen in Figure3.13. Individual carbide and the surrounding matrix can be observed in Figure 3.14. The carbides appear angular and slightly rounded. There are multiple sites of carbide/ grain pullout, which appear black. These can be differentiated from porosity due to their non-circular shape.

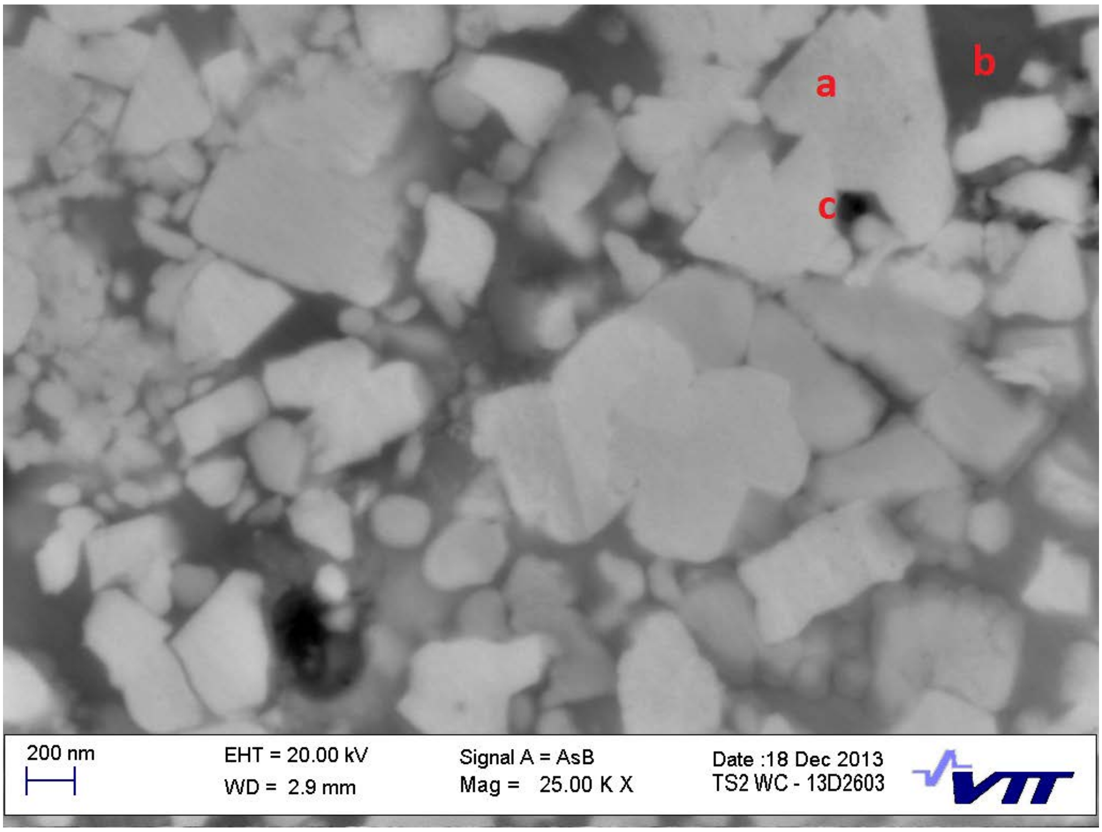

*Note that the features labelled ’a’, ’b’ and ’c’ show examples of the carbide, matrix and pore volumes respectively

Figure 3.14: An annotated SEM image of the microstructure of COMM2, through the cross-section of the coating

At high magnification (see Figure 3.14), the carbides are clearly visible, either individually or by agglommeration. Porosity is also observed. The matrix region appears between the carbide volumes in a range of grey-scale tones. The likely reason is that the softer matrix has been polished preferentially to the harder carbides, leaving areas with a recess as darker grey due to a reduced emission of secondary electrons. It is assumed that the matrix content is consistent through the depth of unpolished coating.

COMM3

The microstructure of COMM3 is complex due to the presence of numerous phases and defects. A through-thickness cross-section of the microstructure can be observed in Figure 3.15. The coating-substrate interface shows some porosity and cracking, which may reduce the bond strength expected from a thermal spray processed material.

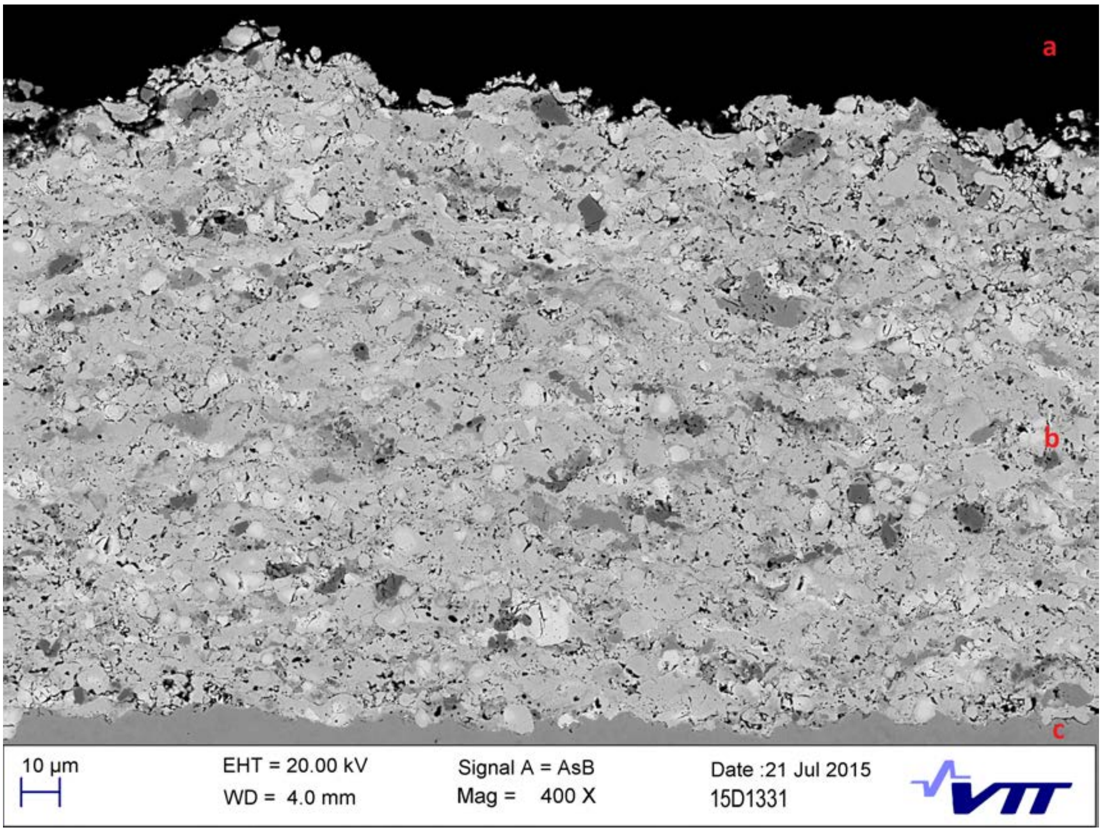

*Note that the features labelled ’a’, ’b’ and ’c’ are the resin binder, coating and substrate volumes respectively

Figure 3.15: An annotated SEM image of the microstructure of COMM3, through the cross-section of the coating

It is difficult to seperate the hard phases (metal borides) from the binder matrix. A higher resolution SEM image of COMM3 microstructure is given in Figure 3.16. The coating appears to be very porous with some cracking.

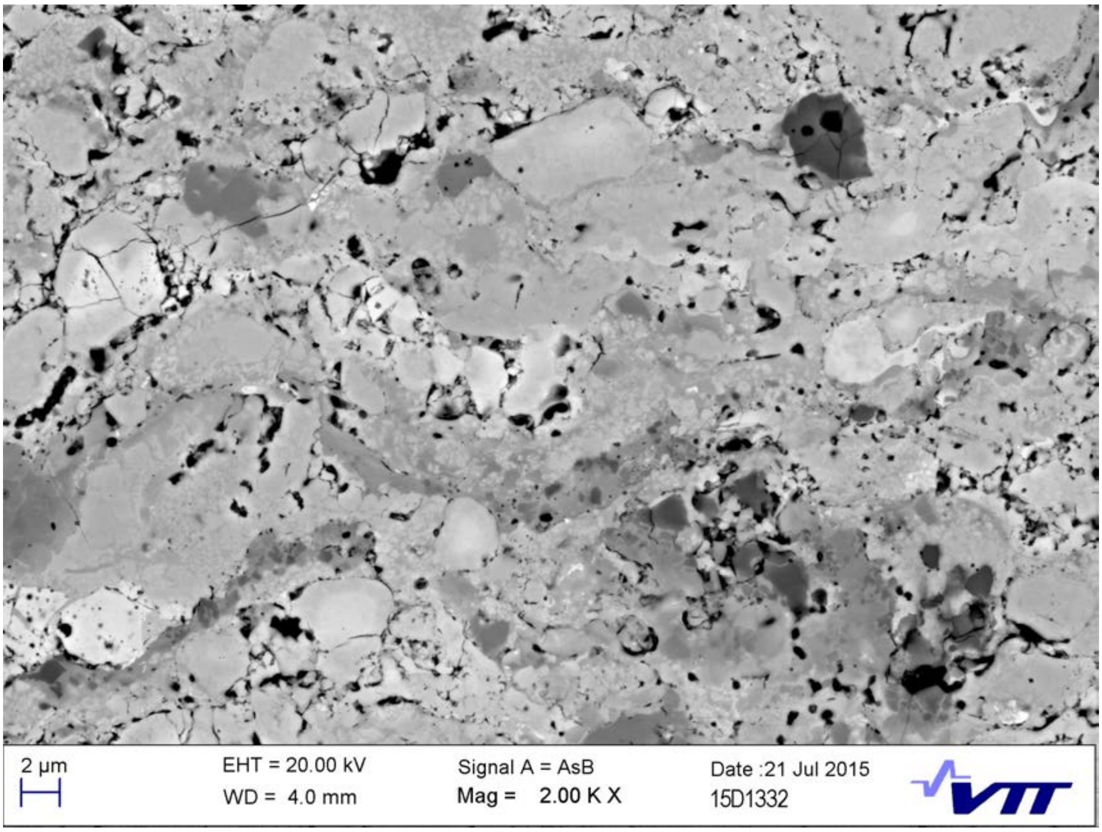

Figure 3.16: An annotated SEM image of the microstructure of COMM3, through the cross-section of the coating

The coating can be defined as being composed of volumes which appear dark or bright, as seen in Figure 3.17. However, it is not analagous to other materials investigated (e.g. COMM1, COMM2). The large volumes which appear to be dark contain smaller, darker volumes.

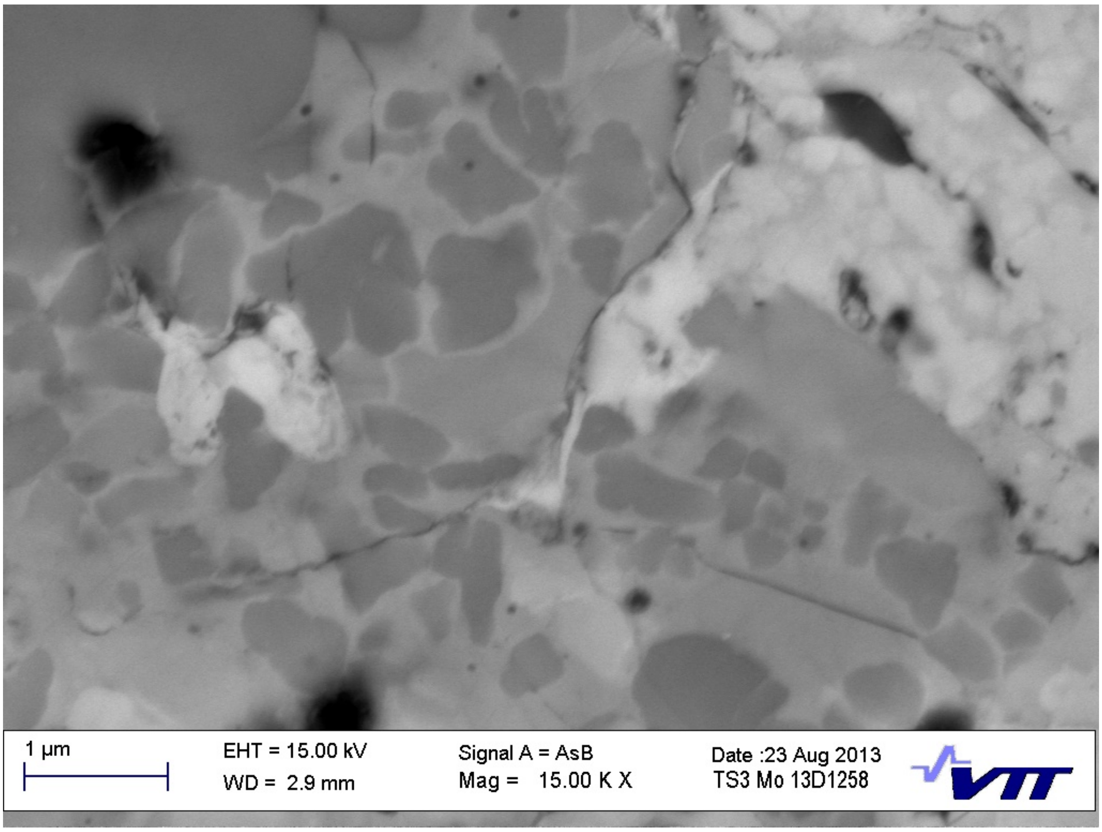

Figure 3.17: An annotated SEM image of the microstructure of COMM3, through the cross-section of the coating

EXP1

As seen in Figure 3.18, EXP1 is well adhered to the steel substrate with minimal porosity nor interfacial cracking. It appears reasonably dense, although the image magnification it is not possible to distinguish porosity from carbde/ grain pullout due to metallographic processing.

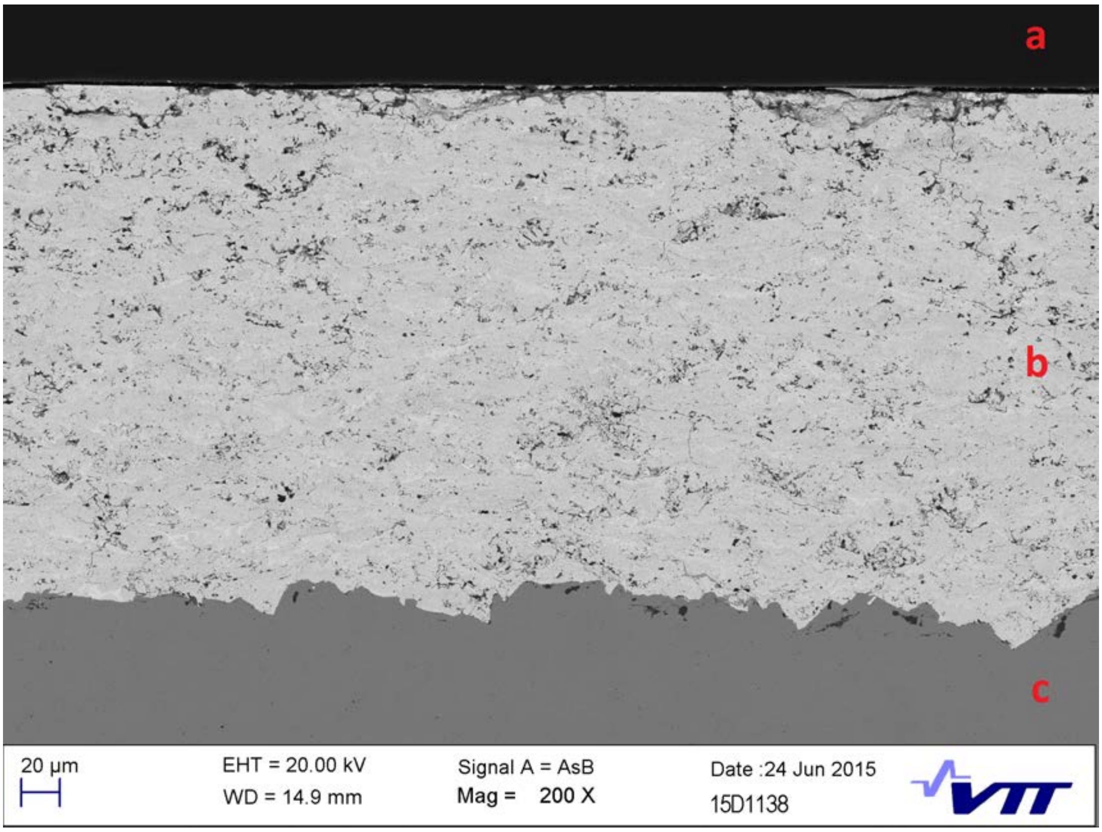

*Note that the features labelled ’a’, ’b’ and ’c’ are the resin binder, coating and substrate volumes respectively

Figure 3.18: An annotated SEM image of the microstructure of EXP1, through the cross-section of the coating

As seen in Figure 3.19, EXP1 has a number of large pores and carbide pullout which appear to be distributed in a non-uniform manner. The black regions tend to link, which may follow a splat boundary. A splat boundary will be compositionally different to the bulk of the split, leading to potentially brittle regions forming facilitating fracture and wear around the splat boundary. Additionally, a splat boundary may facilitate the movement of trapped gases which may lead to pronounced porosity.

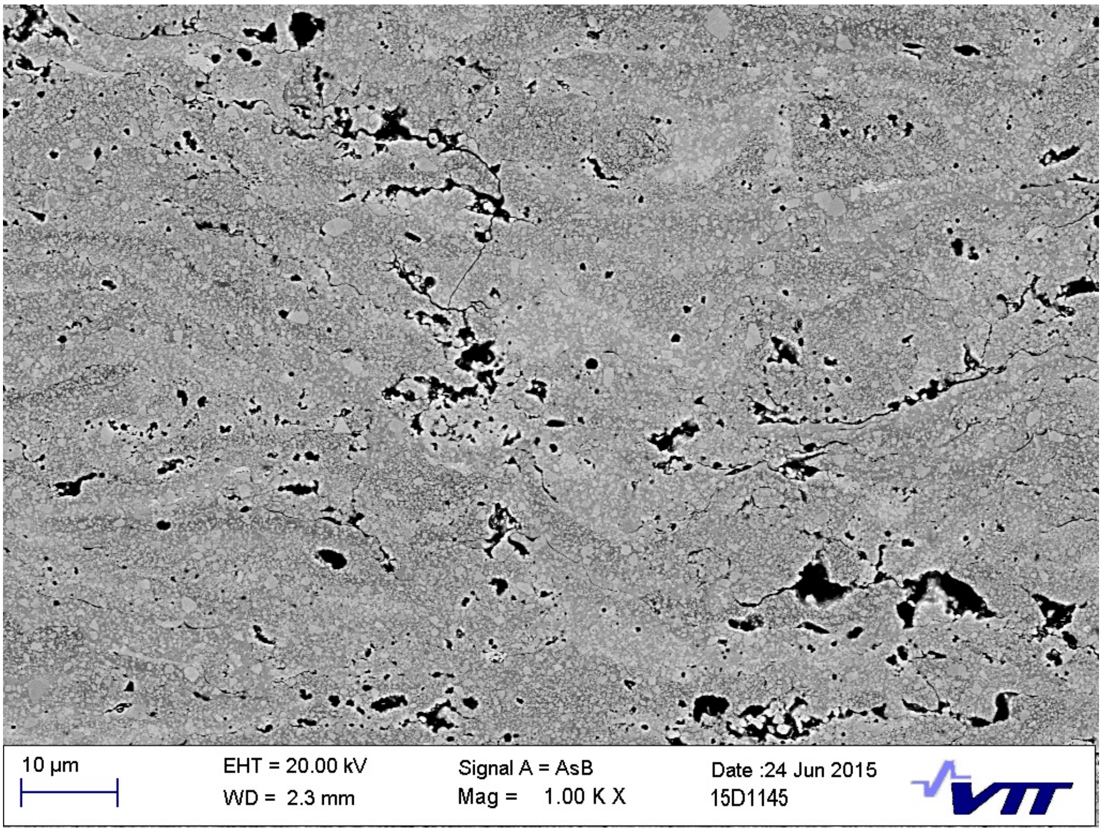

Figure 3.19: An annotated SEM image of the microstructure of EXP1, through the cross-section of the coating

Due to the high spraying temperatures, some carbides have become rounder, with an aspect ratio closer to 1. The roundening is due to diffusion of Tungsten and Carbon from the edges of the carbides to the matrix region. This leads to a complex matrix binder composition which may vary substantially depending upon the location of the site of interest. Examples of round and angular carbides for EXP1 are given in Figure 3.20.

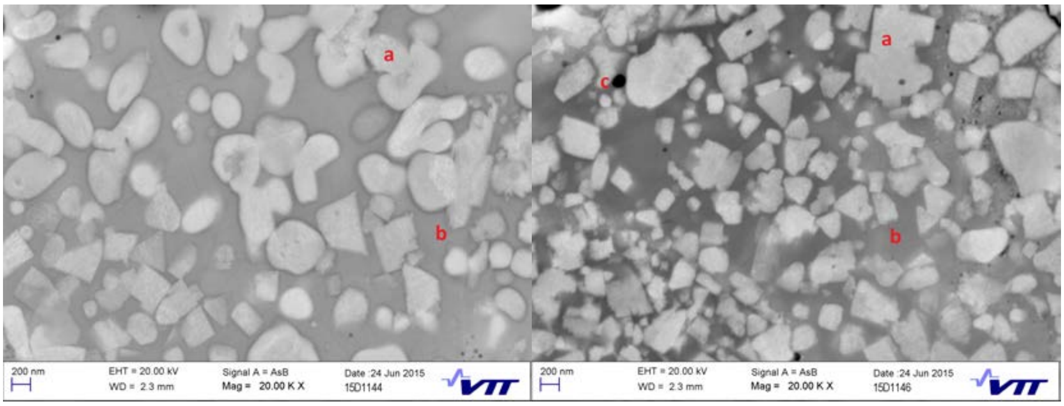

*Note that the features labelled 'a', 'b' and 'c' show examples of the carbide, matrix and pore volumes respectively

Figure 3.20: Two annotated SEM images of the microstructure of EXP1, through the cross-section of the coating

EXP2

As seen in Figure 3.21, EXP2 is dense and well adhered to the substrate. The spraying process involves high particle velocities and reasonably high spray temperatures, which should promote good adherence to the substrate and bonding between splats.

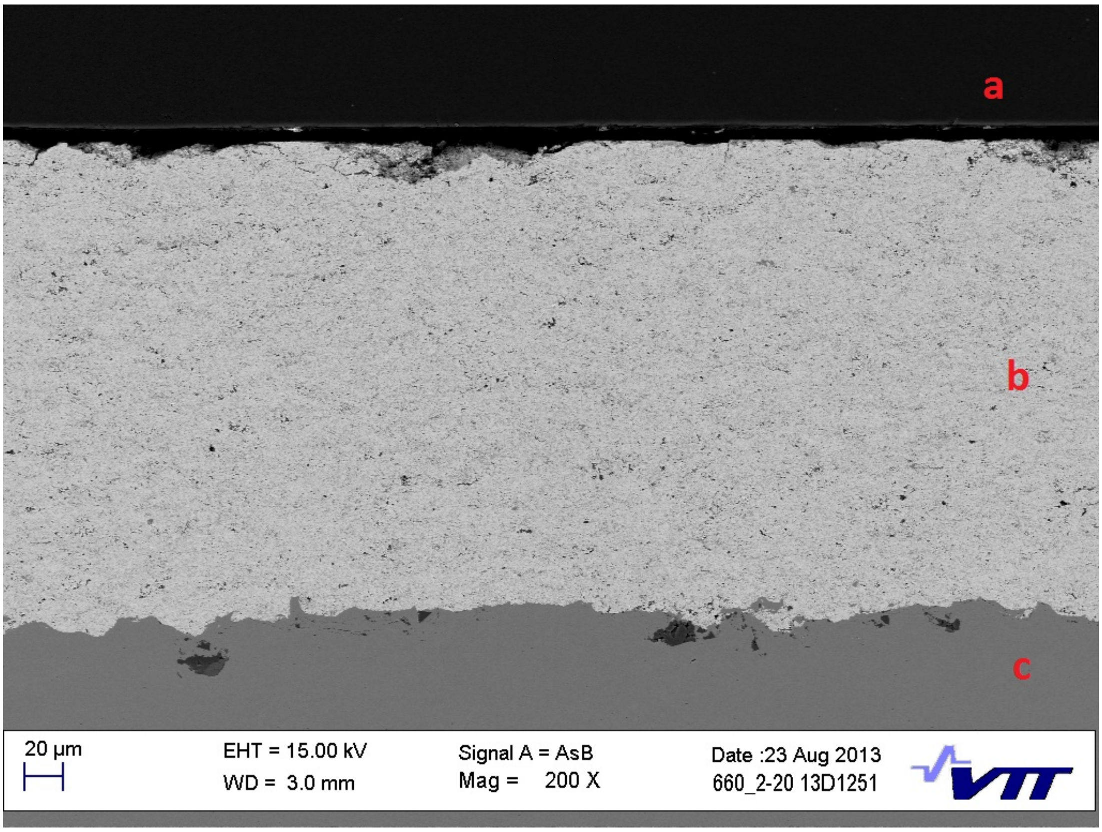

*Note that the features labelled 'a', 'b' and 'c' are the resin binder, coating and substrate volumes respectively

Figure 3.21: An annotated SEM image of the microstructure of EXP2, through the cross-section of the coating

Figure 3.22 shows that the coating is reasonly dense, without any clear splat boundaries as observed for EXP1. However, carbide/ grain pullout is plentyful, due to metallographic processes. Otherwise at this magnification, it looks similar to that of EXP1 as shown in Figure 3.19.

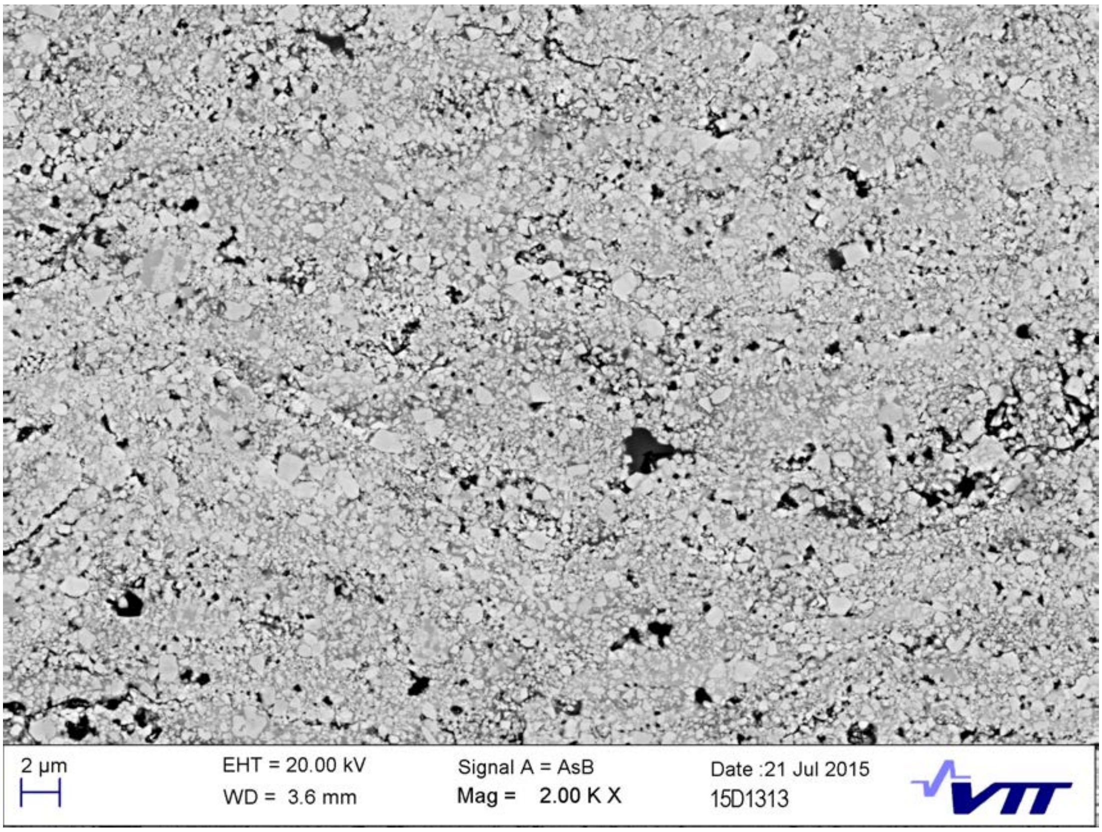

Figure 3.22: A SEM image of the microstructure of EXP2, through the cross-section of the coating

At high magnification, there are numerous points of interest, as shown in Figure 3.23.. The carbides appear very angular with minimal roundening of the edge. This is in contrast to EXP1, as seen in Figure 3.20. The carbides appear to vary in terms of their local size distribution, as there are areas which appear to be tightly packed with small carbides and other areas which are loosely packed with large angular carbides. The carbides are not uniformly spread. Whilst the effect of carbide distribution on the impact and tribological behaviour is not a core aim of this research work, it is interesting to note. Additionally, the distinct regions appear to be quite sharply seperated, potentially by a splat boundary. This may indicate variance in the control of carbide size and agglomeration at the powder processing stage, which is not investigated for this work.

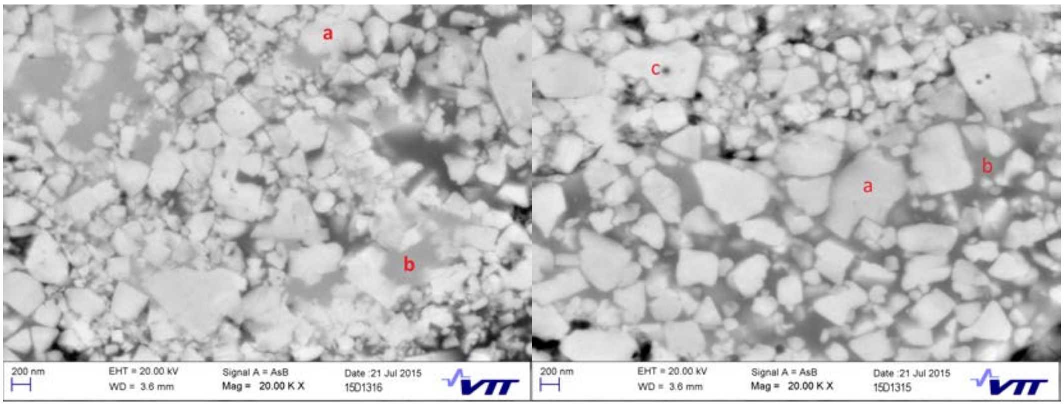

*Note that the features labelled ’a’, ’b’ and ’c’ show examples of the carbide, matrix and pore volumes respectively

Figure 3.23: Two annotated SEM images of the microstructure of EXP2, through the cross-section of the coating

EXP3

As a result of the high particle velocity processing (HVAF), the coating is dense and displays minimal porosity. A cross-sectional image through the coating and steel substrate is shown in Figure 3.24. The coating is well adhered to the substrate with low interfacial porosity and no visible interfacial cracking.

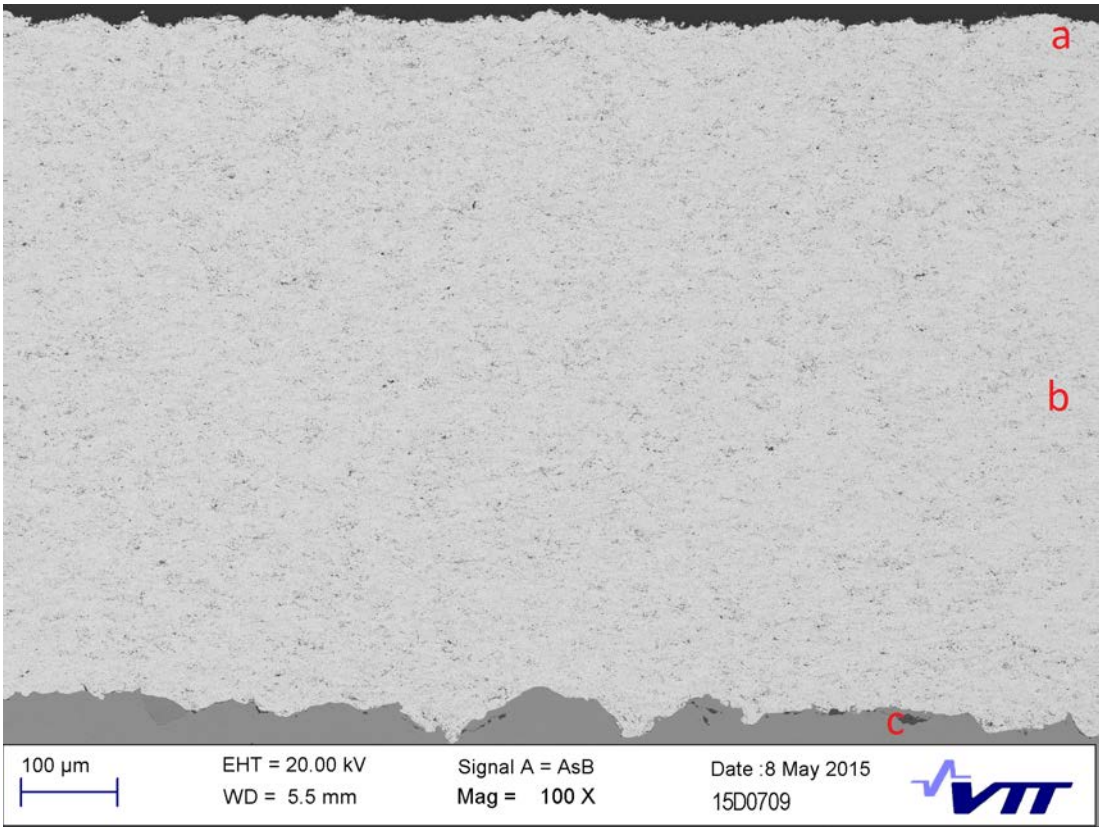

*Note that the features labelled ’a’, ’b’ and ’c’ are the resin binder, coating and substrate volumes respectively

Figure 3.24: An annotated SEM image of the microstructure of EXP3, through the cross-section of the coating

At higher resolution, the coating reveals connected porosity, as seen in Figure 3.25. This may be due to the relatively cool spraying process being unable to sufficiently melt the powder particle surface prior to impact and application. A molten, or atleast sufficiently energetic powder particle surface, may encourage diffusion between its impacted self (splat) and the impact site, which may reduce the porosity.

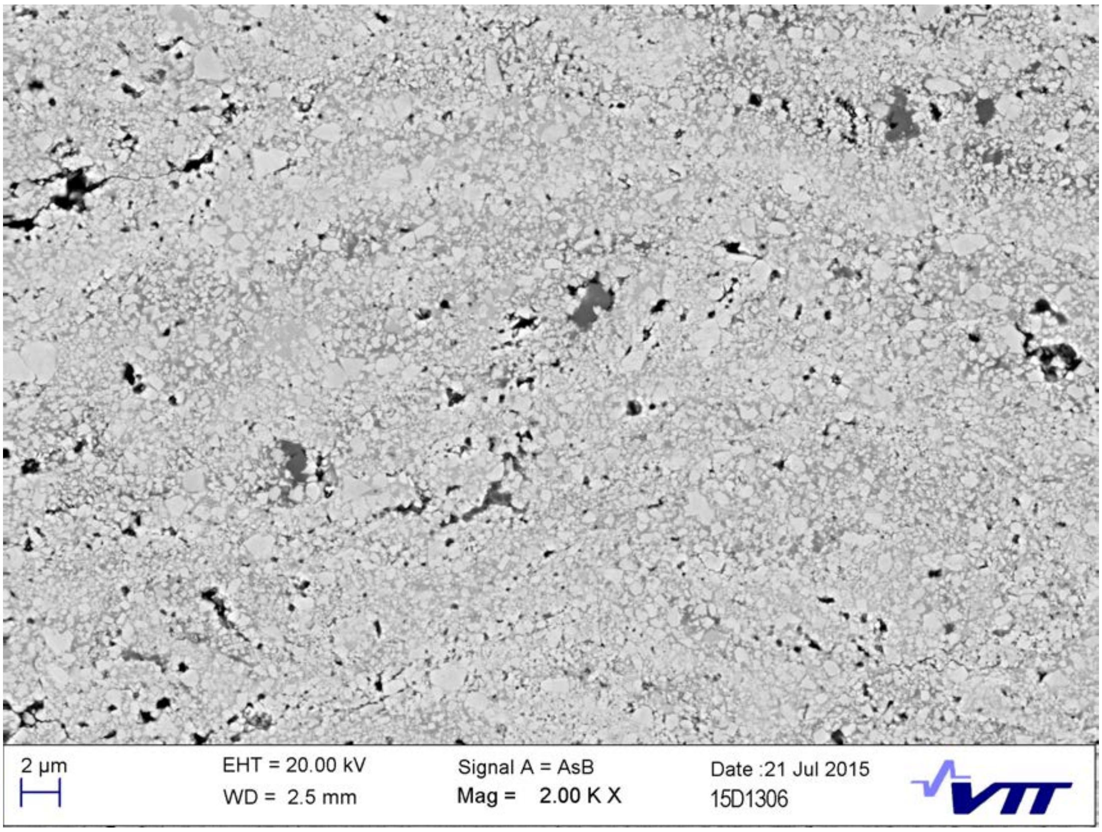

Figure 3.25: A SEM image of the microstructure of EXP3, through the cross-section of the coating

The carbides have not displayed evidence of significant diffusion from the carbide to matrix binder volumes, as the carbides remain angular. Additionally, the matrix volume has a reasonably consistant greyscale tone, indicating that it has a relatively consistent elemental composition. A high resolution image of the carbide and matrix volumes for EXP3 is given in Figure 3.26. Some porosity is observed in the ductile matrix, which may be explained by the low spray temperatures reasoned in the previous paragraph.

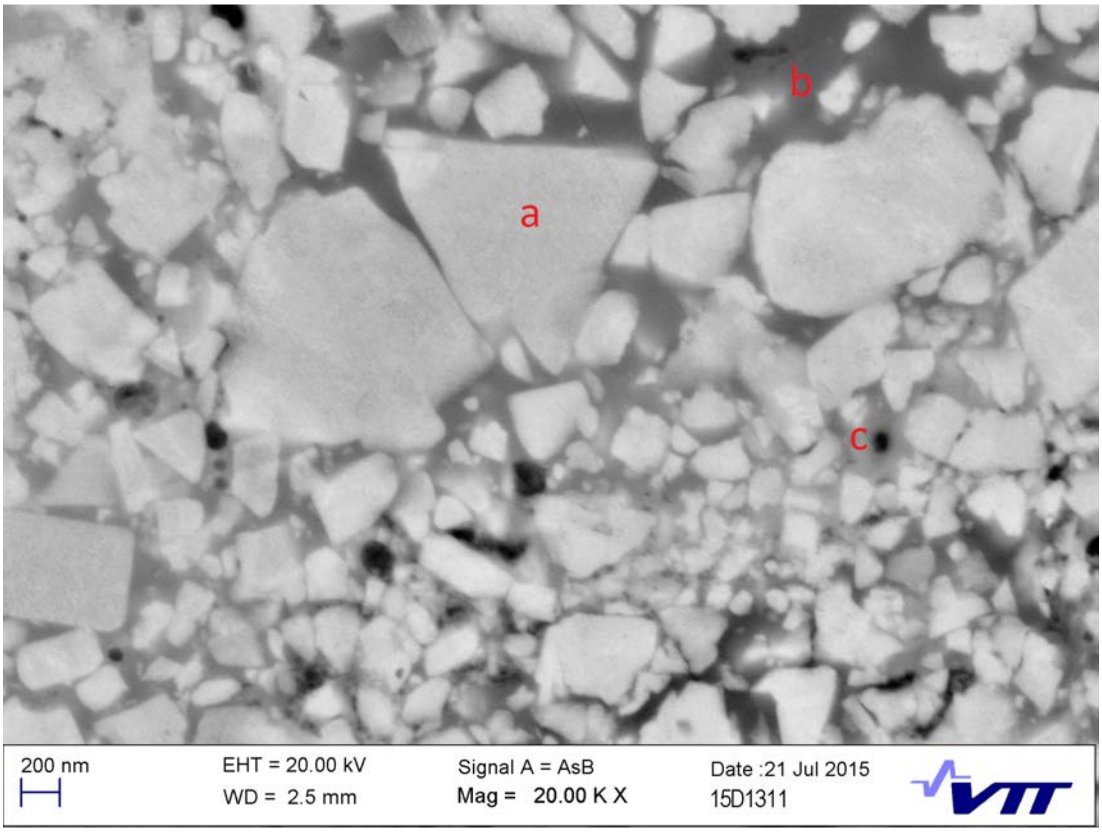

*Note that the features labelled 'a', 'b' and 'c' show examples of the carbide, matrix and pore volumes respectively

Figure 3.26: An annotated SEM image of the microstructure of EXP3, through the cross-section of the coating

EXP4

A cross-section of the steel substrate and thermal spray midlayer is given in Figure 3.27. Please note that the multilayer thin film architecture is not easily identified at this magnification. As per EXP2, of which the thermal spray midlayer and substrate is identical, the coating is well adhered with no significant porosity or cracking along the substrate-midlayer interface.

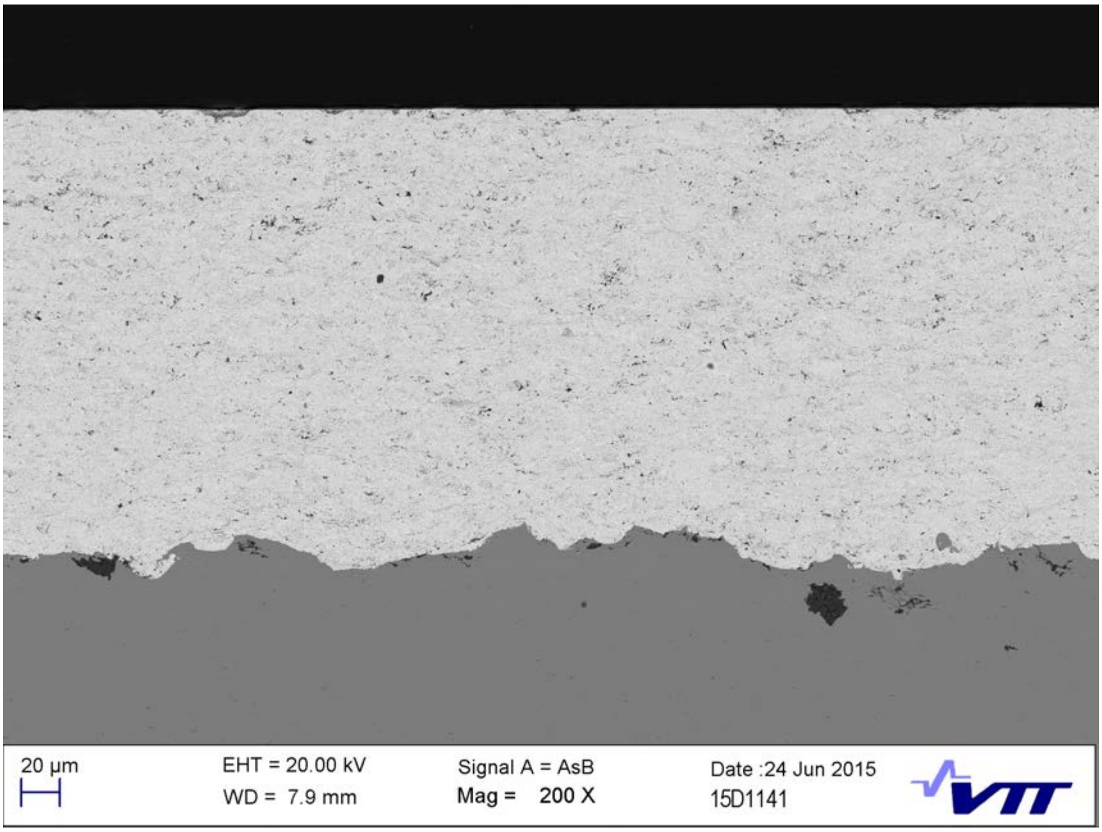

Figure 3.27: A SEM image of the microstructure of EXP4, through the cross-section of the coating

A similar coating was assessed by Holmberg et al. [ref]. The assessed coating features the same DLC, bond coat and gradient layer as EXP4 as they were produced under identical conditions with the same equipment in the same facility at City University of Hong Kong. The substrate is different (M2 steel) and there is no thermal spray interlayer. The thin-film multilayer thicknesses were assessed by FIB-SEM and are seen as representative of EXP4. An example of the FIB-SEM analysis, along with measured thicknesses, is given in Figure 3.28.

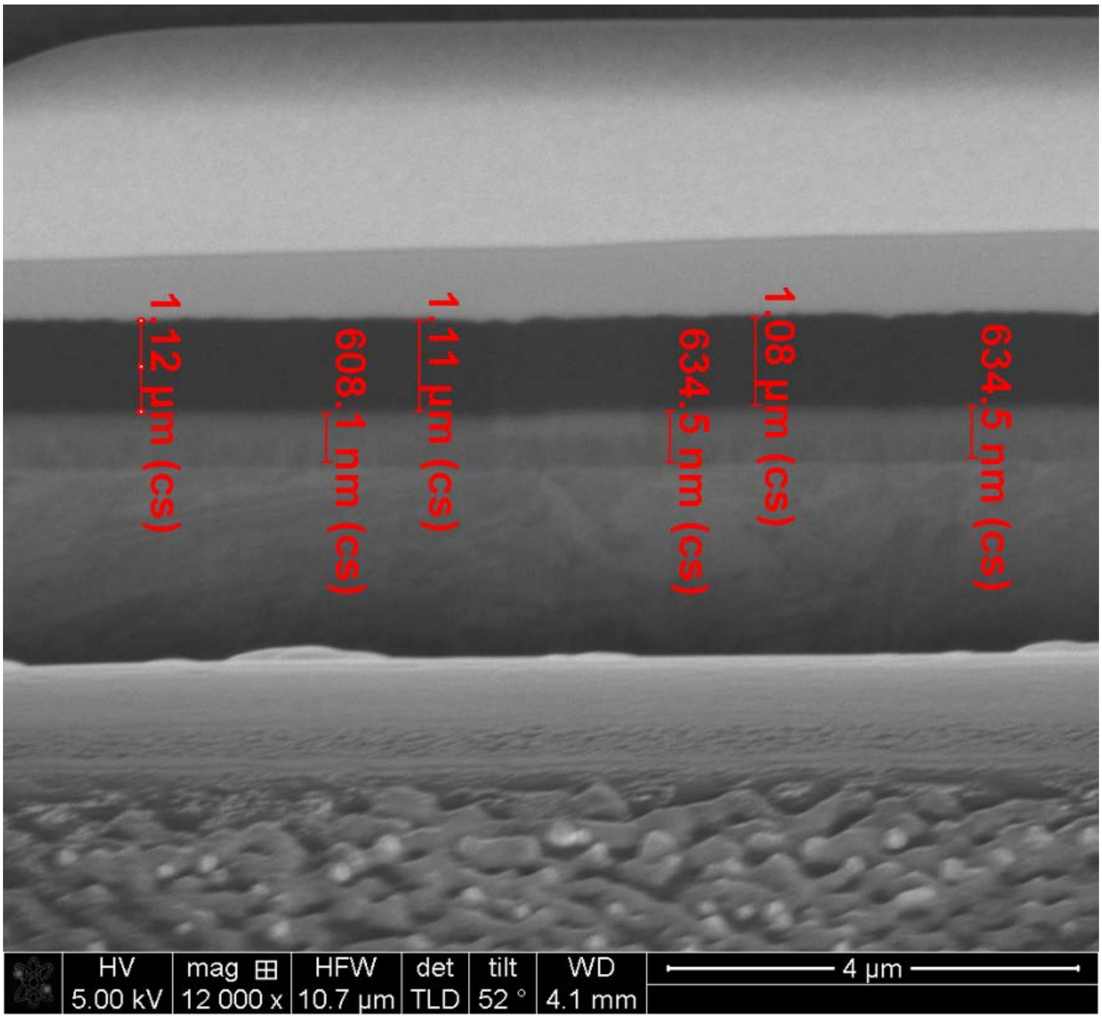

Figure 3.28: Cross-sectional thickness measurements of a similar thin film multilayer coating to EXP4, subject to FIB-SEM analysis

3.3.4 Mechanical properties

The mechanical properties of the coatings were assessed using indentation. Results are presented in Tables 3.9 and 3.10.

	Top surface			Cross section		
Sample code	HV0.3	H_{IT}	E_{IT}	HV0.3	H_{IT}	E_{IT}
EXP1	1349	13,3	268	1201	11,9	266
EXP2	1331	13,1	254	1242	13,2	325
EXP3	1445	14,2	337	1301	19,9	308
EXP4*	-	18	205	-	-	-
COMM1	1146	12,4	218	1109	11,3	238
COMM2	1334	13,3	311	1310	12,6	286
COMM3	1097	10,6	214	1063	10,1	195
Uddeholm Formax	195	2,3	221	195	2,3	221
Bohler K490						

*Note that indentation values for EXP4 are for the top surface, i.e. thin film layer, only. Values are obtained from [117], as described earlier in Table 3.5.

Table 3.9: Mechanical properties of coatings found by micro-instrumented indentation testing

	Top surface		Cross section	
Sample code	Evans-Wilshaw	Anstis	Evans-Wilshaw	Anstis
EXP1				
EXP2				
EXP3				
EXP4	#			
COMM1				
COMM2				
COMM3				

Key: # Cracks did not form with load of 20 kgf (196.1 N) and is thus immeasurable with IIT

Table 3.10: Fracture toughness of coatings found by instrumented indentation testing

Material	Mean free path (µm)	Average carbide diameter (µm)	Carbide aspect ratio
COMM1			
COMM2			
COMM3			
EXP1			
EXP2			
EXP3			
EXP4			

Table 3.11: Important statistical descriptors of the microstructures of the investigated materials

Chapter 4

Scratch Performance

4.1 Introduction

Scratch testing has been well applied for a variety of coated and uncoated materials. Generally, a scratch test involves a relative sliding motion between a test surface and a countersurface of known material, shape and size. The aim of a scratch test is to subject the test surface to loading from the normal direction and the tangential direction as a result of a sliding contact. This loading case is named 'scratch loading'. There are numerous methods available to investigate the scratch performance of materials; these are generally split between scratch adhesion testing and scratch hardness testing.

Scratch hardness investigations offer insight into the deformation behaviour of investigated materials under a scratch loading contact. Examples include the Mohs hardness test and ASTM G171-03 [20]. A definition for scratch hardness is given in ASTM G171-03; "...the resistance of a solid surface to penetration by a moving stylus of given tip radius under constant normal force and speed". This can be used to demonstrate that despite similar loading conditions, scratch hardness testing is considerably different to scratch adhesion testing. Scratch hardness test methods are most commonly used for bulk materials and are discussed further in Section 4.2.1.

Scratch adhesion testing is generally used to investigate the adhesive qualities between two or more joined materials under scratch loading. The use of a scratch test to assess coating adhesion was pioneered by researchers including Valli, Matthews et al. [105], and Burnett and Rickerby [122]. When assessing a pool of different materials, the normal loads at which pre-defined events occur are compared. These are called critical loads (Lc). The definition of the specific critical loads vary depending upon the class of materials, the nature of the experiment and even between researchers. Factors such as friction force, acoustic emission, indenter penetration and material or interface failures should be considered. As such, it is important to clearly specify the criteria which are to be employed when assessing different materials with scratch testing and to ensure that these are consistent with those of other researchers to ensure that results can be compared accurately. For all scratch tests considered in this text, the assessment records the normal force (Fn) applied by the indenter, the tangential frictional force (Ft) and acoustic emission (AE) readings through the indenter. More information of scratch adhesion tests with regards to thin films is is given in Section 4.2.2.

4.2 The analysis of instrumented scratch test scars in published literature

This section describes the current and previous state of scratch test methods for bulk materials, thin hard coatings and thick hard coatings. It is important to understand the different methods used to assess the scratch performance of each of these groups of materials and how they can be used when assessing thermal spray coatings, thin films and multilayer coatings.

4.2.1 Bulk materials

Bulk materials are primarily assessed by scratch hardness testing, unless they can demonstrate repeatable failures which can be compared according to the loading condition at the time of contact. Bulk materials are not coated and are assumed to have similar mechanical behaviour and composition through the material volume. The most general standard [20] can be applied to metals, ceramics, polymers and coated surfaces. Constant loading conditions are used, to create an observable scratch which does not extensively damage the surface through cracking, coating spallation or else. The assessment is based upon the formation of an observable scratch, from which the width of the scratch may be measured after a specified sliding distance. This allows the scratch hardness to be found. Essentially, this describes the degree of plastic deformation of the test material under a contact which was influenced by elastic and plastic deformation, as well friction. The equation for scratch hardness, HSp (GPa), is given in Equation 4.1, where k is a geometrical constant, P is the applied normal force (grams-force) and w is the width of the scratch (µm)[20].

$$HS_P = \frac{kP}{w^2} \tag{4.1}$$

There is a more specific standard for the assessment of plastics and their scratch hardness[109]. Fn, Ft and the form of the scratch are assessed. The scar is observed optically to find examples of damage including cutting and whitening. The ranking of plastics is achieved by comparing the load at which the scratch becomes visible optically, for a given luminance. Loading can be linearly-increasing or constant. Depending upon the contact condition, one can estimate the scratch strength with a point contact or the scratch resistance with a line contact indenter. To the authors best knowledge, there are no standard methods specifically written for either bulk metals, biomaterials, glasses or ceramics.

4.2.2 Thin, hard coatings

The assessment of thin, hard coatings with scratch testing can be performed with a number of methods. If the scratch hardness is being investigated and the coating is not taken to failure by extensive cracking or spallation, [20] may be used.

However, should the cracking or failure modes of the coating, interface and substrate be investigated, other methods should be used. This would demand a scratch adhesion assessment. Key papers describing scratch adhesion testing were given by a number of researchers including J. Valli [105] and P.J. Burnett and D.S. Rickerby in 1987[122]. A scratch adhesion test requires a stylus of known geometry, size and material to be drawn across a flat test specimen at uniform loading rate and sliding speed over a set distance. The loading rate may be equal to or greater than zero; i.e. constant load or linearly increasing load. For both [105] and [122], a 200 µm diameter Rockwell C diamond indenter was used. If the sliding distance, loading rate and sliding speed are known, it is possible to cross-reference the relative location of an adhesion failure against the normal load. Simultaneous recordings of the frictional force, acoustic emission and stylus penetration all add further detail to the description of the adhesive failure event. Typically, the normal force required to initiate an adhesive failure is reported, and it is usually quoted in Newtons.

Typically, the stylus is a Rockwell C diamond with a 200 µm radius although others may be used as required. When assessing very thin coatings (less than 500 nm), radii as low as 20 µm may be used. Other geometries are also available, such as Vickers, Beckovich and spheres when required.

Work by Valli et al. [105] used the friction recordings to define the critical loads, followed by confirmation by optical microscopy. It was shown that for the tested materials (TiN coated steels) that the coefficient of friction changes abruptly with respect to the normal load (Fn), that there may be a measurable, critical failure of the coating. In agreement with [1], the critical failure loads recorded were initial cracking around the indenter at lower friction forces and full coating penetration and interfacial spallation at high friction forces . A summary of the failures typically observed for thin, hard coatings is given in Section 4.4.1.

Burnett and Rickerby [122] investigated the morphology of adhesive failure modes for thin ceramic coatings on steel substrates. Their methodology is based upon identifying the key critical failures and recording the normal load for failure (Lc) using optical microscopy. The failures were assessed to establish links between the fracture patterns of the ceramic coating and how this can be used to identify the loading state. This approach was further developed to form the basis of "BS EN 1071-3:2005[1] which is now widely used. The key failures which were identified were spallation, buckling, chipping, conformal cracking and tensile cracking.

An accepted and published standard[1] details a method which uses a linearly increasing or constantly loaded indenter to scratch a coated surface until adhesive and/or cohesive failures are observed. These failures may be observed through changes in Ft, AE, indenter penetration or optically. A schematic of the failures is given in Figure 4.1.

The critical loads Lc1, Lc2 and Lc3 described in Figure 4.1 correspond to initial cracking of the coating inside or at the edge of the scratch, local interfacial spallation and gross interfacial spallation. In practice, the critical loads can be defined by using the Ft, AE or indenter penetration recordings or by microscopy.

4.2.3 Thick, hard coatings

Compared to bulk materials and thin, hard coatings, the guidelines to interpreting the scratch performance of thick, hard coatings are less comprehensive in terms of standard methodologies.

At the time of writing, to the author's knowledge, there no formal, accepted and published standard methodologies for thick, hard coatings when considering their scratch adhesion performance which are analogous to [1]. However, the generic ASTM G171-03 standard may be used when investigating scratch hardness [20].

There are a few examples of published research where scratch testing has been performed across a material cross-section. to assess coating adhesion. The sole example of a standard methodology is ISO 27307, which was developed to aid the investigation of the adhesive and cohesive strength of thick, plasma thermal spray oxide coatings [110]. The author was involved with this work and it is recently published. It is the result of a round-robin study between VTT in Finland and other resarch groups in Japan and

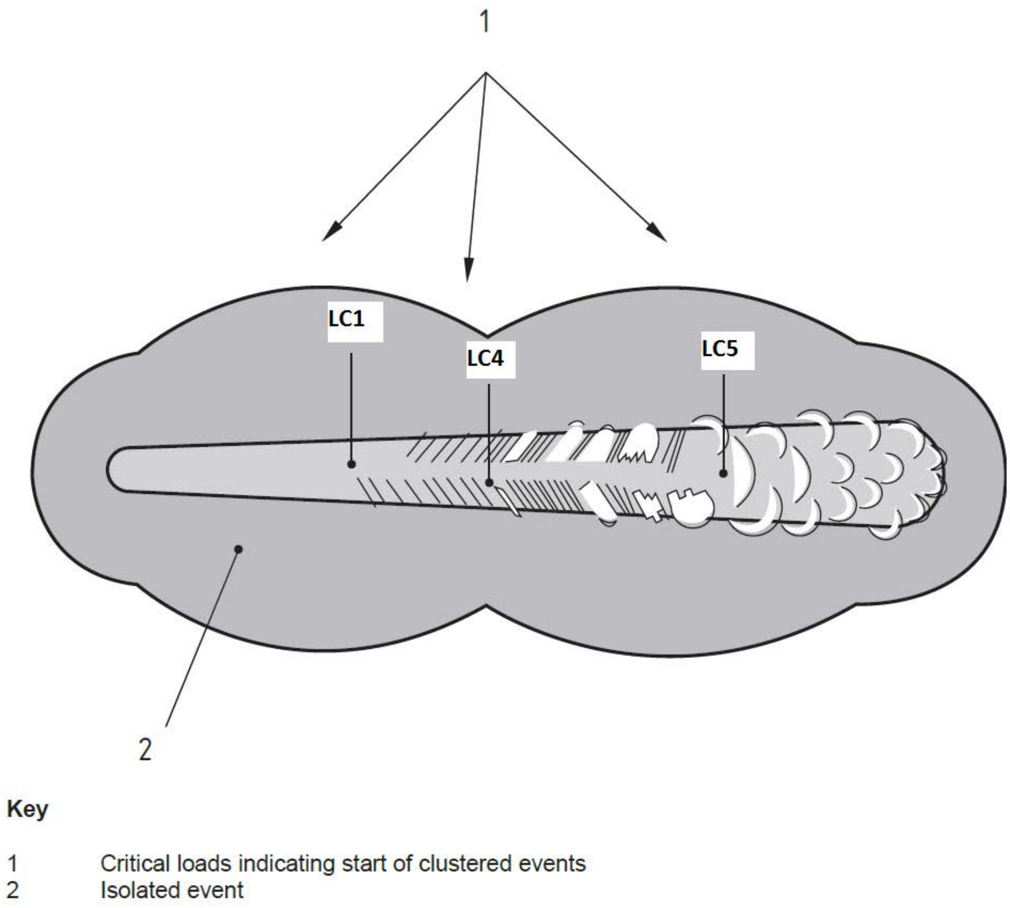

Figure 4.1: Schematic diagram showing the key critical failure mechanisms for thin, hard coatings, adapted to suit the Hybrid method[1]

Korea. The work focused primarily on scratch tests with a constant load. The scratch was made across the cross section of coated specimen, i.e. from the steel substrate into the coating across the coating-substrate interface. The nature of the adhesive and cohesive failure of the coating was recorded using optical microscopy. This work did not develop any criteria for critical failure loads as described in Section 4.2.2 and thus it is found to be lacking. Similar approaches have been used to investigate the role of bond coats for thermal barrier coatings (TBC) for aerospace applications [53, 123]. One problem with the method is that an increased penetration depth, caused by e.g. softer substrate, leads to a higher contact area between the indenter and investigated material for a given load.

The cross-sectional method is based on the work of Beltzung et al. [124]. It relies on the formation of a cone-shaped failure in the coating, whose size and geometry can be used to describe the toughness of the coating. The cone failure is defined as the area which has suffered complete detachment and material removal. . In addition, there may be interfacial failures and cohesive fractures as described in [53, 110, 123]. Jones used the method to qualitively rank thermal barrier oxide coatings by comparing coating crack length to the scratch normal load with no consideration for the cone shape. It has been suggested by Nohava et al. that the methodology may need revision to revise the cone shape to include the side cracks which demonstrate a cohesive coating failure [123], however no significant efforts have been made to accomodate this suggestion.

Some efforts have been made to adapt the methods of [1]. For HVOF metal-carbide based thick coatings, some guidance is available from Ghabchi et al. [2, 60]. Ghabchi developed a test method based upon [1], where key failures based on the first observation of adhesive failure of the interface, cohesive failure of the coating and various crack morphologies were compared to the applied normal load. A description of each critical load by Ghabchi is given in Section 4.4.2. Primarily, Ghabchi defined the first observed failure for each mode by optical microscopy. This is in contrast to earlier work at VTT [105] suggesting the use of the tangential friction measurements, as well as acoustic emission, and their change as a function of the applied normal force. It is suspected that the complexities of the carbide coating microstructure tested leading to complex cracking, make acoustic emission derivation of the critical failure loads unreliable. Likewise, the thickness and resiliance of the coating, demands extremely high load to encourage interfacial spallation over delamination by a cohesive failure. Regardless, the author is unaware of published critical loads for thick, hard composite coatings found by methods using changes of tangential friction force or acoustic emission, as Valli [105] had done for thin, ceramic coatings.

4.3 A new method to assess the scratch response of thick, hard thermal spray coatings vs. thin, hard coatings

Consistency is needed when developing a framework to enable the comparison of the investigated materials. It is possible to use the method described by Ghabci [60] to assess materials EXP1 - 3 and COMM1 - 3. For EXP4, it is possible to use the approach developed by Burnett and Rickerby [122], as performed by Bolelli et al. [92] for a similar thermal spray - DLC multilayer coating. Both approaches assume

Failure	Critical load			
	[122]	[60]	[92]	Hybrid
Collapse	-	Lc1	-	Lc0
Edge (Angular) crack	Lc1	Lc2	Lc1	Lc1
Semi-circular crack	-	Lc3 and Lc4	-	Lc2
Cohesive spallation	-	Lc5	-	Lc3
Edge adhesive spallation	Lc2	-	Lc2	Lc4
Severe adhesive spallation	Lc3	-	Lc3	Lc5

Table 4.1: A guiding framework to aid the comparison of the critical failures described in the literature and those developed in this work

that the underlying material (i.e. substrate metal or thermal spray interlayer) do not suffer damage beyond plastic deformation. For multilayer, multi-process coatings both approaches are ultimately simplistic and need adapting to suit the varying individual failures which develop as a result of a scratch adhesion test.

A guiding framework has been developed, to aid the interpretation of thin, hard films, thick thermal spray coatings and hybrids. The guiding framework is presented in Table 4.1 and a schematic drawing is presented in Figure 4.2. The critical failure criteria for thin, ceramic coatings [122], thick thermal spray coatings [60] and hybrid TS-DLC coatings [92] are presented alongside a new proposal, under the column named Hybrid. The new method includes failures observed for both thin and thick coatings. The failures have been ranked numerically according to their severeity. The new method has been used consistently throughout this document.

The collapse of material is can be observed for both thin and thick coatings. For thin coatings, the collapse can be attributed to plastic deformation substrate whilst the coating is still adhered to the substrate. For thick coatings, the substrate and the coating may deform simultaneously or seperately.

Edge cracks or angular cracks are observed for both thin and thick coatings. These failures form reliably and consistently for the investigated materials. It is possible to use this as a means to define the fracture toughness of a material under a scratch contact and to use it to validate a computational model [125].

Semi-circular cracks, as described in Section 4.4.2, were observed for the investigated thermal spray materials but not for EXP4. These have been observed for some thin film coatings, as shown in [1].

Cohesive spallation is the loss of coating material due to fracture and cleavage within the coating. After a single contact event, the substrate should not be exposed and a remainder of the lower thickness of the coating should still be adhered. Cohesive

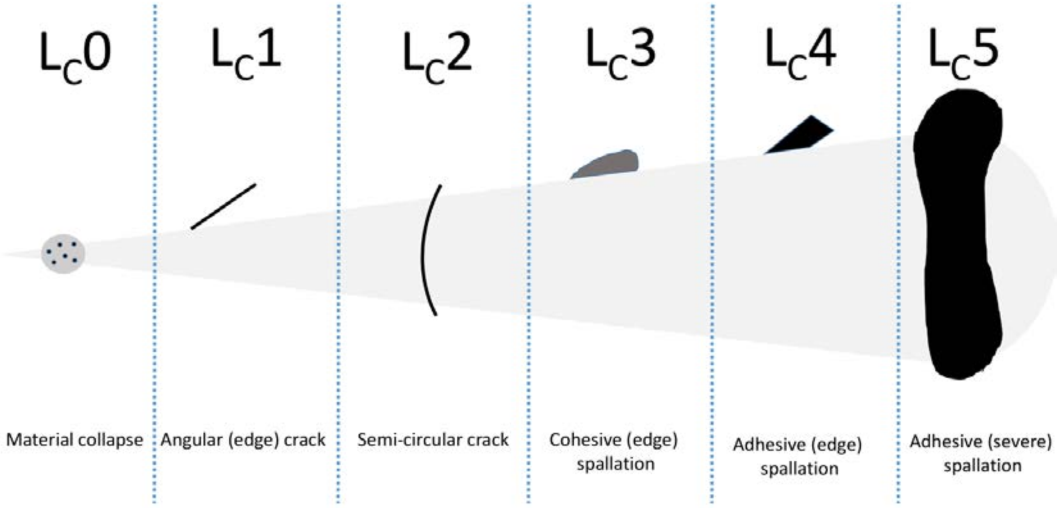

Figure 4.2: A schematic drawing of the typical failures observed for a scratch adhesion test of thin, hard coatings or thick, hard coatings using the Hybrid method

spallation is easily observed for thick, thermal spray coatings where the substrate-coating interface is not loaded to failure. However, as seen in [1], cohesive failures can be observed for both relatively thin metal and ceramic coatings on metal substrates.

Under the investigated conditions, with a maximum scratch normal load of 100 N, adhesive spallation was not observed for the thermal spray coatings. As for [1] and [122], adhesive spallation is divided into two categories; local spallation primarily observed on the edge of the scratch scar and severe spallation across the scratch scar and beyond.

4.4 The analysis of the investigated materials with instrumented scratch test methods

Scratch test techniques have been used to assess failure mechanisms of thick carbide coatings under single asperity loaded contacts [60, 110]. The employed technique applies a linearly increasing normal load onto the investigated surface through a known counterface. The experimental details are given in Section 2.3.1 and Table 2.3. The scratch performance of thin film, hard coatings has researched well [20, 106, 107, 126], where it is possible to investigate critical failure loads [127], coating system failure modes [20] and adhesive fracture strength [128] . For the latter, the significantly higher thickness and complex microstructure of thick TS coatings do not allow easy analysis due to the different roles performed by different constituent volumes [51], as well as the possibility for cohesive failure of the coating by splat-splat bonding interface failure[60].

4.4.1 Thin, hard coatings

The critical failures for EXP4 are described in detail and compared with similar results in published literature. Analysis is based on methods by Valli [105] and [122]. The average critical failure loads are given in Table 4.4.1.

Description of critical failures for thin, hard coatings

Angular (edge) cracking, Lc1

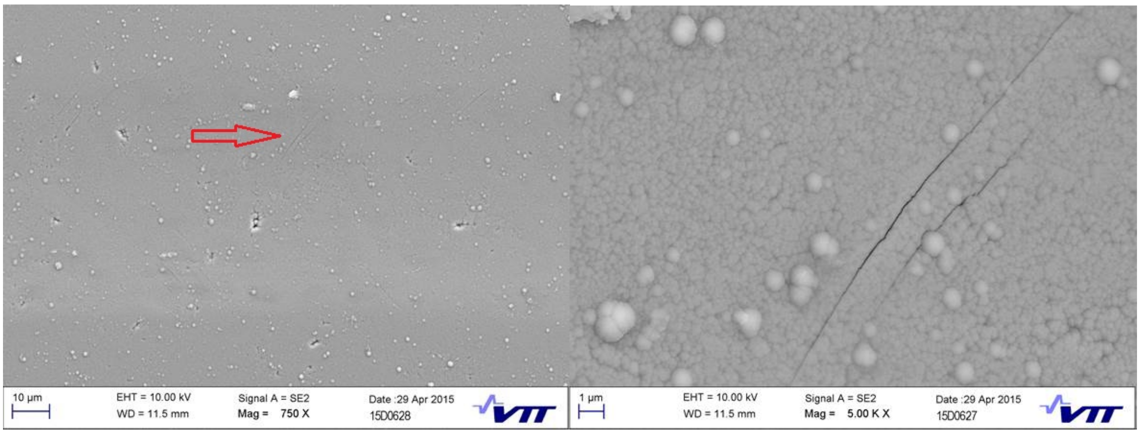

Figure 4.3: SEM images of forward edge chevron cracks for EXP4, at low magnification (left) and high magnification (right)

Cracks are the most often recorded first failures for thin, hard coatings under scratch testing. Cracks may be either conformal or tensile. The conformal cracks arise to the high penetration of the indenter leading to tensile bending underneath the indenter. Tensile cracks form due to high tensile frictional stresses behind the indenter, which act to balance the high compressive frictional stresses ahead of the indenter. Tensile cracks tend to grow in size, originating from the scratch itself and propagating beyond the edges of the scratch. Conformal scratches do not typically reach beyond the edges of the scratch scar. For the assessed material, EXP4, only tensile cracks were observed under the described test conditions. Edge cracks are observed for EXP4 for test parameter sets VTT1. The edge cracks are similar to the forward chevron cracks described in [1].

Local adhesive spallation, Lc4

Significant damage to the coating is caused by spallation and buckling of the coating. This is where compressive stresses accumulate ahead of the sliding indenter. Spallation is where the coating detaches itself completely from the substrate material and can be regarded as an adhesive failure. As such, determining the conditions at which the adhesive failure occurs can be used to rate the quality of adhesion between the coating and its substrate. Spallation is also commonly refered to as delamination. Buckling occurs due to partial spallation of the coating, where semi-circular cracks develop due to compressive stresses ahead of the sliding indenter. The nominal compressive stress for total spallation is greater than that for buckling.

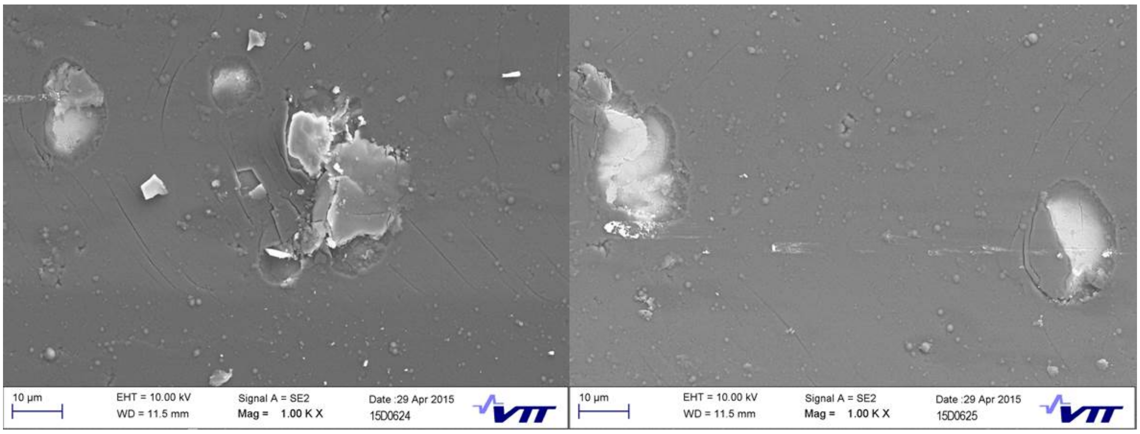

Figure 4.4: SEM images of local interfacial spallation of EXP4

In the case of EXP4, loss of material is observed solely due to spallation alongside edge cracks, as seen in Figure 4.4. The ejected debris does not appear to embed itself into the substrate or coating, when assessed by optical microscopy.

Severe adhesive spallation, Lc5

Gross interfacial spallation was not observed for EXP4. The adhesion between the thin film and the thick coating was sufficient to prevent spallation under the test conditions. Buckling was not observed as conformal cracks did not develop ahead of the sliding indenter.

Critical failure loads results for thin, hard coatings

The average critical failure loads for the investigated thin, hard coating (EXP4) are presented alongside results of similar materials in Table 4.2.

Material	Test parameter set	Lc1	Lc4	Lc5
	Unit	N	N	N
EXP4	VTT 1	25.80	44.97	> 100
EXP4	CSM	20.53	> 30	> 30
DLC-S	[117]	9.6	> 30	-

Table 4.2: Scratch test critical failure loads for thin, hard coatings

Discussion

The observed failures for the EXP4 coating do not match those of the investigated thick, hard coatings (Section 4.2.2). The recorded failure modes for thick, hard coatings may be present in EXP4 under the test conditions, yet these may be visibly obscured due to the thin coating on top. Without detailed characterisation of the thermal spray volume underneath the thin film, it is difficult to describe the scratch performance of EXP4 with the same critical failure modes as in Section 4.2.2. Thus, the EXP4 coating system is assessed according to criteria for thin, hard coatings and not for thick, hard coatings.

The EXP4 coating system was assessed with two different parameters sets (VTT1, CSM). For both sets, the critical failure loads are fairly consistent. The first angular crack (Lc1) was first observed between 20 N and 25 N. The higher load VTT 1 set caused failure by local spallation (Lc4) at 44.97 N, whilst the CSM set did not due to a lower maximum normal force (Fn). For both sets, severe spallation was not observed as described in [122].

One interesting observation is that the EXP4 coating displayed a significantly higher Lc1 value compared to that of a similar coated specimen, DLC-S [117], as seen in Table 4.2. DLC-S is comprised of the same thin film multilayer profile as EXP4 with a different substrate metal (Bearing steel, AISI52100) and no thick thermal spray interlayer. The thin, hard coatings were made according under near-identical processing conditions at the same facility. The scratch tests were performed at VTT using the same equipment and similar test conditions. If one disregards the effect of the substrate on the critical load Lc1, it clear that EXP4 offers significant fracture resistance. If the substrates are considered, it suggests that increasing the hardness and elastic modulus of the volume underneath the thin coating architecture leads to increases in the Lc1 value.

$$a_c = \frac{V_F}{V} \tag{4.2}$$

$$V = V_F + \chi . V_S \tag{4.3}$$

$$\chi \propto \left(\frac{E_F . H_S}{E_S . H_F} \right)^q \; for \; H_F > H_S \tag{4.4}$$

*Note that a_c is the indentation zone radius, V_F and V_S are the respective deforming volumes of the coating and substrate whilst V is the overall deformation, \chi is an interface constraint parameter found experimentally, H_F and H_S are the respective hardnesses of the film and substrate and E_F and E_S are the respective Elastic Modulii of the film and substrate.

In [117], DLC-S did not exhibit spallation (Lc4) under the test conditions. This result is shared by EXP4. Thus, it is not possible to determine by experimental resultswhether the thick, thermal spray layer improves the adhesion of the DLC multilayer to the under layer. As seen in Equations 4.2 - 4.4, Burnett and Rickerby [122] suggested that a critical shear stress determined the critical failure load for a given coating system and substrate material. When a rule of mixtures relationship is assigned to the deformed volume, V, it is seen that it is proportional to the ratio H_S:H_F for an ideally smooth interface. Thus, a harder substrate reduces the deformed volume and minimises plastic deformation and interfacial strain. This may lead to an increased critical failure load for local spallation. Thus, it is expected that EXP4 will give a higher Lc4 value than DLC-S under identical test conditions.

4.4.2 Thick, hard coatings

Description of critical failures for thick, thermal spray coatings

A summary of the critical failure loads is given, along with a schematic in Figure4.5. Please note that the identification and numbering (e.g. LcX, where X is a positive integer or zero) is used consistently in the given form throughout this document.

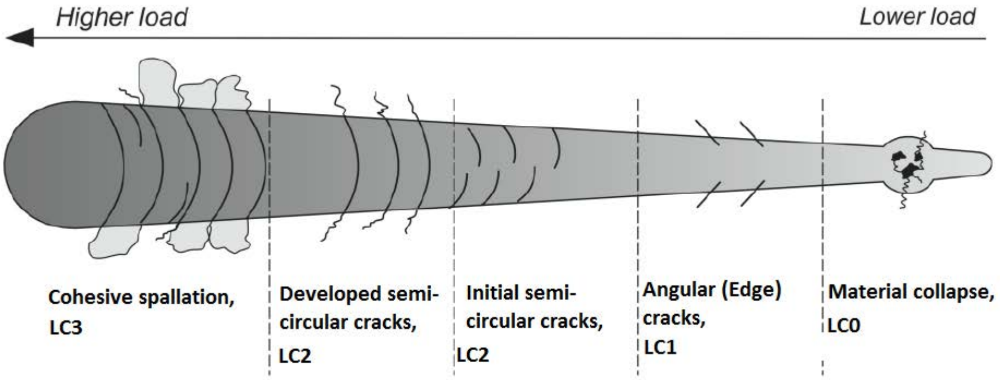

Figure 4.5: Schematic diagram showing the key critical failure mechanisms for thick, carbide coatings, adapted to suit the Hybrid method[2]

Collapse of material, Lc0

In the base of the scratch, the coating may leave visible voids. These voids arise due to a local inability to sustain the load applied by the sliding indenter. There may be surface porosity, near-surface porosity, easily compressible solid volumes or localised, heavy cracking. With regards to thermal spray carbide coatings, the origin of the void is likely to be collapse of material around a surface [60] or near-surface pore. Regardless, collapse of material in the base of the scratch was not observed sufficiently often to record an accurate value for investigated materials for most tests. To reliably detect Lc0, the porosity should be high enough so that the scratch path has a significant chance of overlapping near-surface porosity. As such, it is an unreliable failure critera which cannot be recommended for dense and wellformed thermal spray coatings.

Angular Crack, Lc1

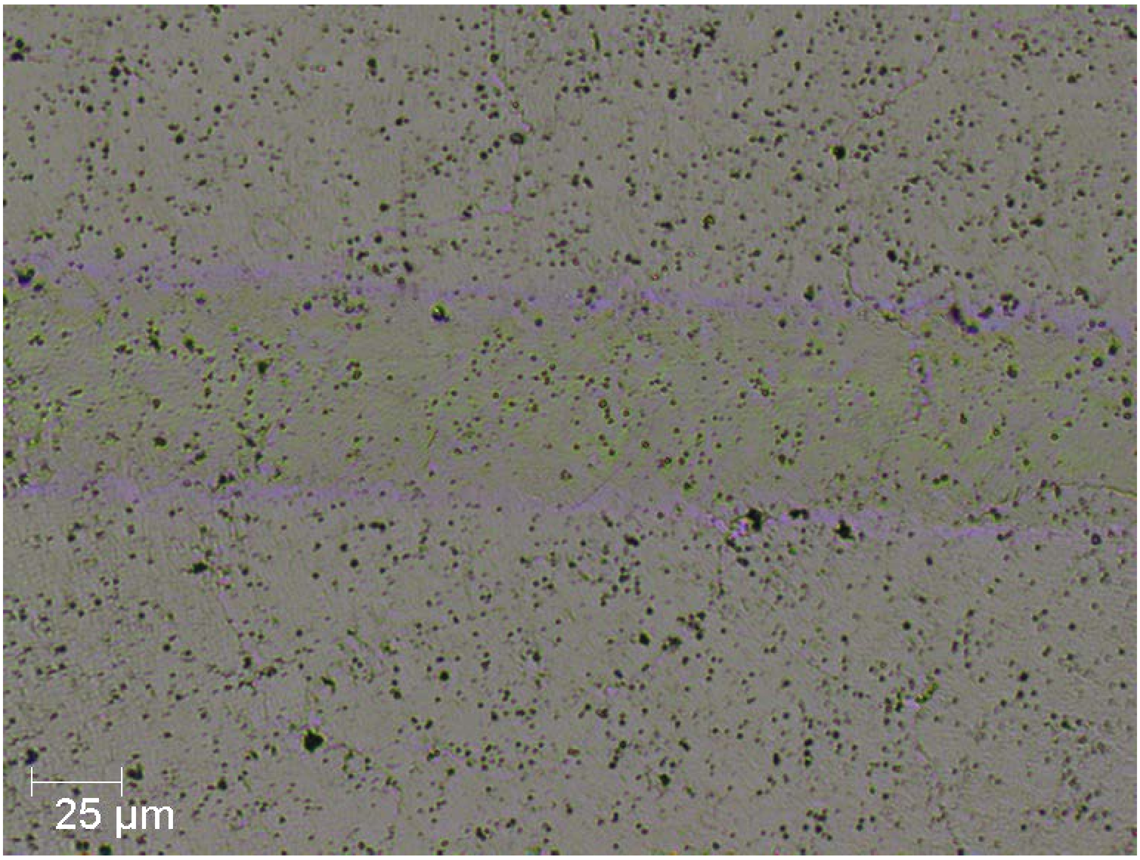

Figure 4.6: Example of an angular crack observed for a thermal spray coating (EXP2)

Angular cracks develop at the edge of the scratchs, according to criteria given by Ghabci et al. [2]. They become more well defined as the load is increased. The critical load, Lc1, is first observed angular crack. An angular crack is relatively easy to identify in comparison to Lc2. Additionally, angular cracks were observed for all materials and share the same appearance as for angular cracks of thin, hard ceramic coatings [1].

Initial semi-circular crack and developed semi-circular crack, Lc2

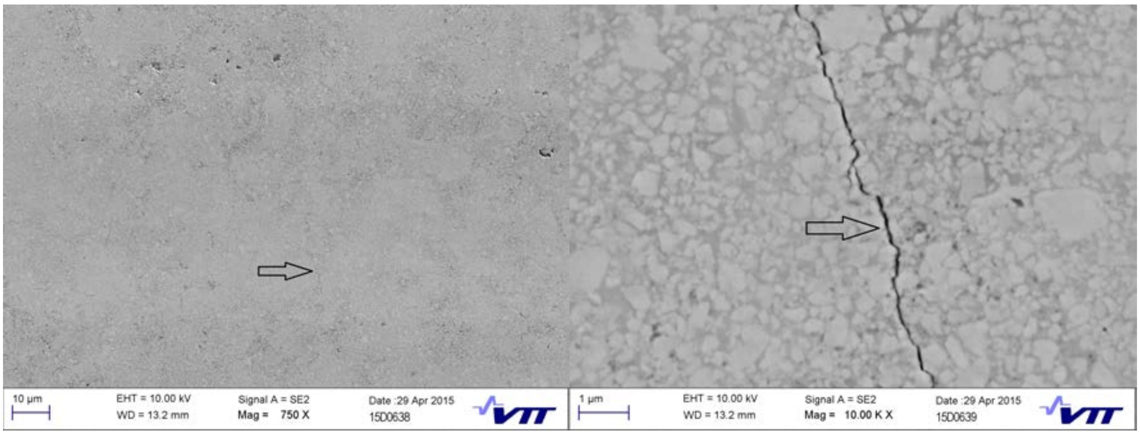

Figure 4.7: Examples of initial semi-circular cracks observed for a thermal spray coating (EXP3)

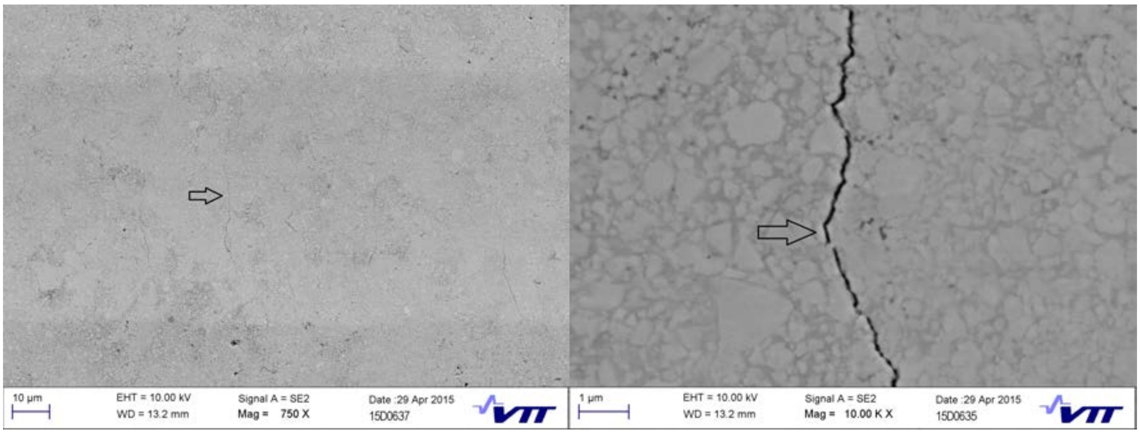

Figure 4.8: Examples of developed semi-circular cracks observed for a thermal spray coating (EXP3)

Semi-circular cracks develop inside the scratch, on the edges. Initial semi-circular cracks are not fully formed, i.e. fully extended across the width of the scratch perpendicular to the scratch direction. Developed semi-circular cracks which have propagated along the whole width. Ghabci [60] suggested that the cracks arise due to high tensile stresses behind the indenter. For both cases, it was shown that the cracks remain close to the surface and do not propagate to the substrate-coating interface under similar test conditions to those investigated.

It is difficult to distinguish partially developed and fully developed semi-circular failures. For EXP3 the cracks were very fine under optical microscope observation, which served as the primary method to observe and record fracture. It is recommended that either initial or developed semi-circular cracks are investigated, but not both, in an effort to save resources.

Cohesive (edge) spallation, Lc3

For thermal spray coatings, the edge failure of coating generally occurs as a result of cohesive failure between splats, leading to ejection of coating material and wear and internal splat cleavage. The first measureable failure is usually limited to a fraction of the coating thickness near to the surface; there is no interfacial failure between the coating and the substrate at under the investigations performed. The splat-splat interfaces are considered to be weak with respect to that of the inner volume of a single splat [2] and offer a pathway for crack propagation which would lead to delamination. In that sense, Lc3 is a value which can be used to define the intersplat cohesion of the thermal sprayed coating.

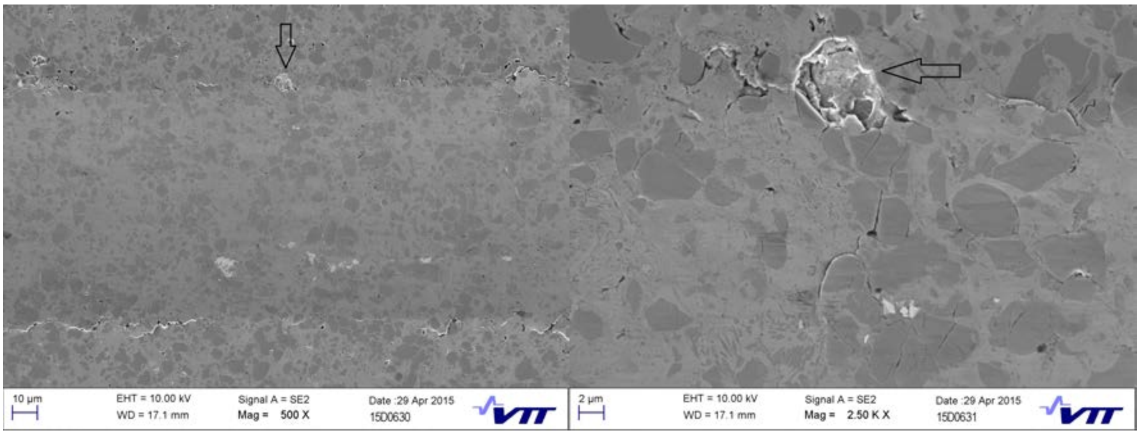

Figure 4.9: Example of a complete edge delamination observed for a thermal spray coating (COMM1) at two different magnifications

As for thin, ceramic coatings, edge failures are easily observed. For thin film coatings on ductile substrates, where the coatings are considered to be relatively homogeneous, a delamination event often leads to a through-thickness failure whereby the delaminated particle exposes the substrate[1]. This is in contrast to that of the thermal spray coatings which are tested. The thermal spray coatings did not demonstrate failure of the substrate-coating interface nor subsequent debonding.

$$P_0 = \frac{3P}{2\pi a^2} \tag{4.5}$$

By using Equation 4.5, the peak pressure may be calculated for a static sphere indenting a flat plane when using a Hertzian sphere-sphere contact method. Note that $P_0$is the peak pressure, W is the load and a is the radius of the contact area. The peak pressure is found to be ${}^{3w}/{}_{2a^2}$ below the contact point. A higher load is required to increase the depth of the peak pressure region. If the contact is assumed to be sliding, maximum pressure moves ahead of the indenter and closer to the surface. Thus, great loads are required to cause substrate-coating debonding and are not observed under the test conditions. As such, it is not reasonable to compare the critical failure Lc3 found for thermal spray materials with delamination failure of thin ceramic coatings.

Instead, a thermal spray coating fails by two methods; splat-splat debonding and cleavage of individual splats. It is difficult to differentiate between the two as they are likely to occur simultaneously when developing features as shown in Figure 4.9. In order to be consistent with the work related to scratch adhesion testing of thin, ceramic coatings [1, 122], the failure is termed as a critical edge failure and not as delamination.

Critical failure load results for thick, thermal spray coatings

The average critical failure loads are given in Table 4.3 for the thick, thermal spray materials.

Material	Test parameter set	Unit	Lc0	Lc1	Lc2		Lc3
					Initial	Developed	
EXP1	VTT 1	N	-	2.5	6.6	8.8	23.9
EXP2	VTT 1	N	-	7.7	5.8	12.7	47.1
EXP3	VTT 2	N	-	14.8	18.8	27.1	42.4
COMM1	VTT 1	N	-	7.2	16.8	-	46.2
COMM2	VTT 1	N	-	5.6	15.1	33.7	62.0
COMM3	VTT 1	N	-	4.3	5.4	18.3	50.5

Table 4.3: Scratch test critical failure loads

Discussion

The scratch tests produced visible scars enabling identification of failures related to crack formation (Lc1 and Lc2) and cohesive failure (Lc3). The failures were observed for most coatings and it is possible to assign ranking of these materials based on the magnitude of their average critical load values. The ranking of the investigated materials according to criteria related to crack resistance and cohesive strength is given in Table 4.4.

Ranking	Fracture resistance (Lc1)	Fracture resistance (Lc2)	Cohesive strength (Lc3)
1	EXP3	EXP3	COMM2
2	EXP2	COMM1	COMM3
3	COMM1	COMM2	EXP2
4	COMM2	EXP1	COMM1
5	COMM3	EXP2	EXP3
6	EXP1	COMM3	EXP1

Table 4.4: The ranking of thick, thermal spray materials according to different criteria based on average scratch test critical loads

In terms of resistance to failure by fracture, EXP3 is the best performer whilst COMM3 and EXP1 perform comparatively poorly. The materials are ranked according to the average position from Table 4.4.

4.5 Summary

The investigated coatings were assessed by scratch testing. The response of thermal spray coatings was compared to that of a DLC multilayer coating and against published results from other researchers. The distinction between scratch hardness and scratch adhesion testing was made, with an assessment of the available techniques to measure both. The test materials were subject to a new assessment criteria, based upon the work of Burnett and Rickerby [122], Valli et al. [105] and Ghabci [60]. An analysis method is developed which can offer direct comparison of the scratch performance of both thin, hard coatings and thick, composite coatings from the perspective of adhesion and cohesion assessment.

The assessment of the thermal spray coatings (EXP1 - 3 and COMM1 - 3) was based on the work of Ghabci [60] with a view to updating the definitions of each critical failure to provide easier comparison with the work of Burnett and Rickerby [122]. The

. The coatings varied by their mechanical properties (e.g. hardness, elastic modulus), fracture toughness and microstructure. Scratch testing was used as the contact is a dynamic loading contact with subjects the coatings to complex and, sometimes, aggressive stress and strain conditions. This is somewhat similar to an impact experiment.

The thermal spray coatings were assessed according to criteria developed by Ghabci [60] where five failures modes are investigated. The failure modes are defined as different cracking patterns. leading to impaired functionality of the coating. These lead to failure through various means, including intersplat cracking, intercarbide cracking and intracarbide cracking, and delamination of the coating through cohesive failure. For the thermal sprayed coatings investigated, the spallation events were not able to expose the substrate and as such each coating affords a degree of protection to the steel substrate. By comparing Lc3 values it is possible to quantify the level of protection.

The critical load values were compared against the test results for hardness, elastic modulus and fracture toughness for both top-surface and cross-sectional loading directions.

Chapter 5

Percussive normal impact

5.1 Introduction

The percussive normal impact tests were performed to investigate the performance of the test materials under high cycle impact conditions with minimal shear forces in the coating, substrate or at the interface between the two, which would arise from a partial sliding contact. Additionally, a limited FEA simulation was developed to investigate the deformation behaviour of select investigated materials. The FEA simulation work, presented in Section **??** is validated against the results of the experimental testing, presented in Section 5.2.

5.2 Experimental assessment of percussive normal impact

The low load tests (peak impact force of 100 ±5 N) were designed to reduce the influence of the mechanical support of the substrate under dynamic loading by minimising the deformation under impact. Likewise, for some tests the peak stress was hoped to be below the Yield Strength (σ_{Y}) of the coating. It can be regarded as a fatigue test when one considers the damage evolution around, but not inside, the impact crater where the coating was not directly loaded by the impacting body.

The high load tests (peak impact force of 1750 ±50 N) were designed to assess both the coating and substrate together as a coating system. For the industrial applications with which DesiCri was assigned to investigate (minerals handling, mining), testing the coating system is appropriate. Difficulties with regard to interpretation of the impact performance arise as a result of deformation behaviour of the substrate and how this affects the performance of the coating. The substrate materials employed were not those which are commonly used by the industrial sponsors and were instead chosen due to VTT's good experience of using these as substrates for thermal spray coating application.

The impact tests were checked using Hertzian contact analysis, with the results presented in Table 5.1. This analysis is based on a static contact, however it is used due to a lack of a suitable alternative for a dynamic impact. The radius of the effective modulus (E*), contact areas of the two bodies (a), maximum contact pressure (P_0) and indentation depth (δ) were calculated using Equations 5.1, 5.2, 5.3 and 5.4 respectively. The top-surface elastic modulus values from Table 3.9 were used, along with a ball of radius of 3 mm indenting a flat and infinite plane.

$$\frac{1}{E*} = \frac{1-\nu_1^2}{E_1} - \frac{1-\nu_2^2}{E_2} \tag{5.1}$$

$$A = \sqrt[3]{\frac{3F}{8}\frac{\left(\frac{1-\nu_12}{E_1} + \frac{1-\nu_22}{E_2}\right)}{\left(\frac{1}{2R_1} + \frac{1}{2R_2}\right)}} \tag{5.2}$$

$$P_0 = \frac{3F}{2\pi A^2} \tag{5.3}$$

$$\delta = \frac{A^2}{R} = \sqrt[3]{\left(\frac{9F^2}{16RE*^{*2}}\right)} \tag{5.4}$$

Note that the Effective modulus, E, is calculated using the Poisson's ratio, \nu, and Elastic Modulus, E of both materials. In addition, the contact area of the two bodies, A, is calculated using the Force, F, and the radius of the elastic sphere, R. The Peak Pressure, P_0, and the Indentation Depth, δ, can also be calculated.

According to a static Hertzian analysis, the indentation depth, δ, is over 3 µm for all low-load tests. Thus, for the thermal spray coatings, it's possible that a volume equivalent to 2 or more splats may be impacted for the low load tests. In the case of EXP4, the hybrid thermal spray- diamond-like carbon multilayer, the indentation depth is greater than the total thickness of the thin film components, roughly 1.6 µm. Thus, thin film components and upper splats of the thermal spray interlayer subject to high stresses. In the case of the high load tests, similar results are obtained, except that the indented depth and volume is inherently larger due to higher applied loads.

[compare hertzian to impact].

Material	Poisson's ratio	Ref.	Low load	(100 N)	High load	(1750 N)
			P_0	δ	P_0	δ
			GPa	μm	GPa	μm
EXP1	0.26	-	4.41	3.61	11.45	24.32
EXP2	0.26	-	4.30	3.70	11.17	24.94
EXP3	0.26	-	4.89	3.26	12.69	21.96
EXP4	0.202	[117]	3.82	4.16	9.92	28.07
COMM1	0.26	-	4.00	3.98	10.38	26.84
COMM2	0.26	-	4.72	3.37	12.25	22.74
COMM3	0.26	-	3.96	4.02	10.28	27.09
Substrate	0.30	-	4.07	3.91	10.57	26.35

Table 5.1: Hertzian contact parameters for percussive normal impact testing

5.2.1 Description of the primary impact failures for percussive normal impact

There are clear differences in the results of the tested materials under percussive impact testing, at low and high impact loads. Figure 5.1 describes the failures in the coated samples after percussive impact testing by a schematic drawing. Each failure is described and discussed below.

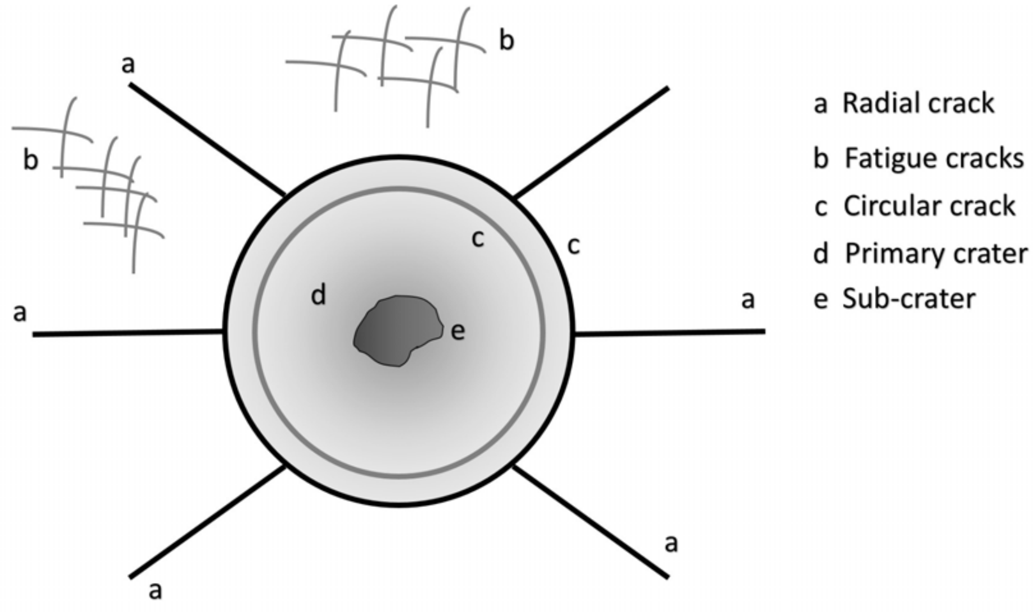

Figure 5.1: Schematic diagram of typical failures for TS coatings during percussive normal impact tests

Crater formation

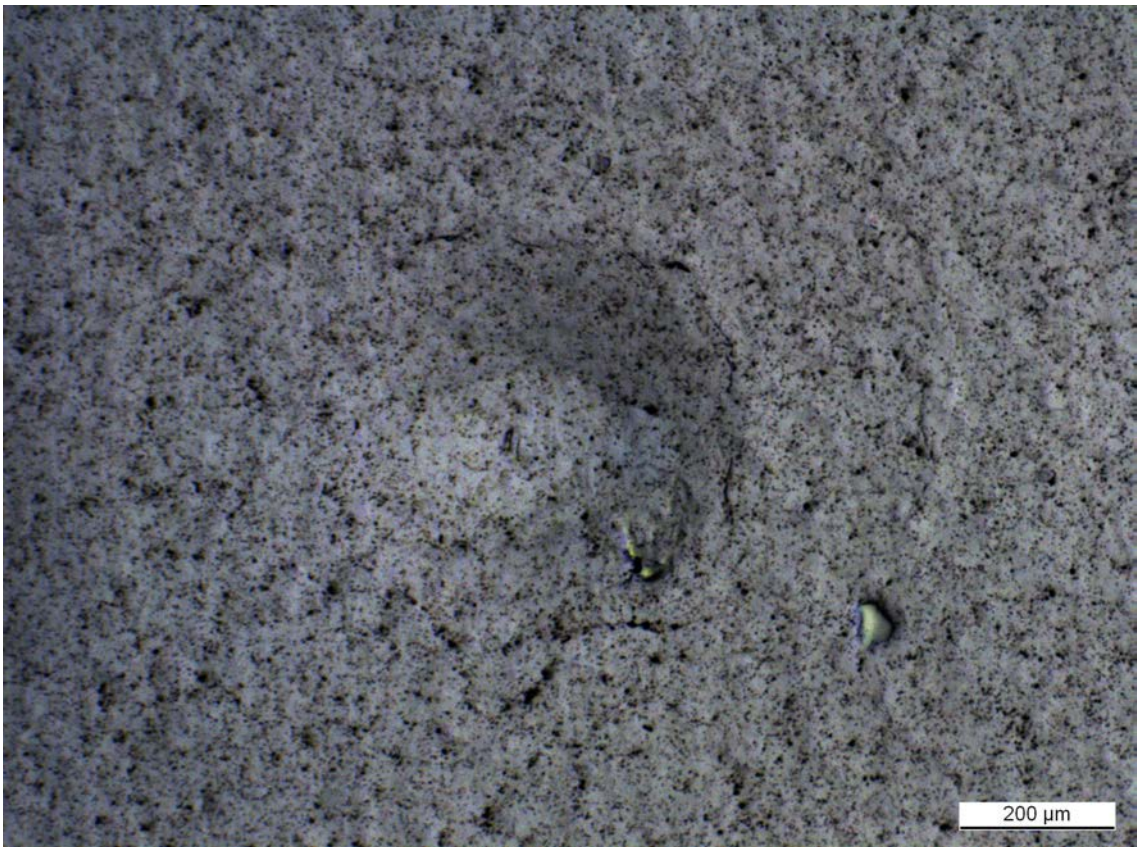

Figure 5.2: Optical micrograph showing the plastic deformation of a thermal spray coating system (EXP4) after percussive normal impact (100 N, 1k cycles)

The most common first indication of damage to the coating was by the formation of an impact crater. The process is dominated by plastic deformation of the coating and substrate. The crater is circular when viewed from the impact direction and is conformal to the shape of the spherical counterface when elastic deformation of the coating system is disregarded. Wear is not considered as fracture or adhesive transfer of material are not observed on the impact surface. The onset and development of crater formation and plastic deformation may be used to validate FEA efforts.

Circular crack

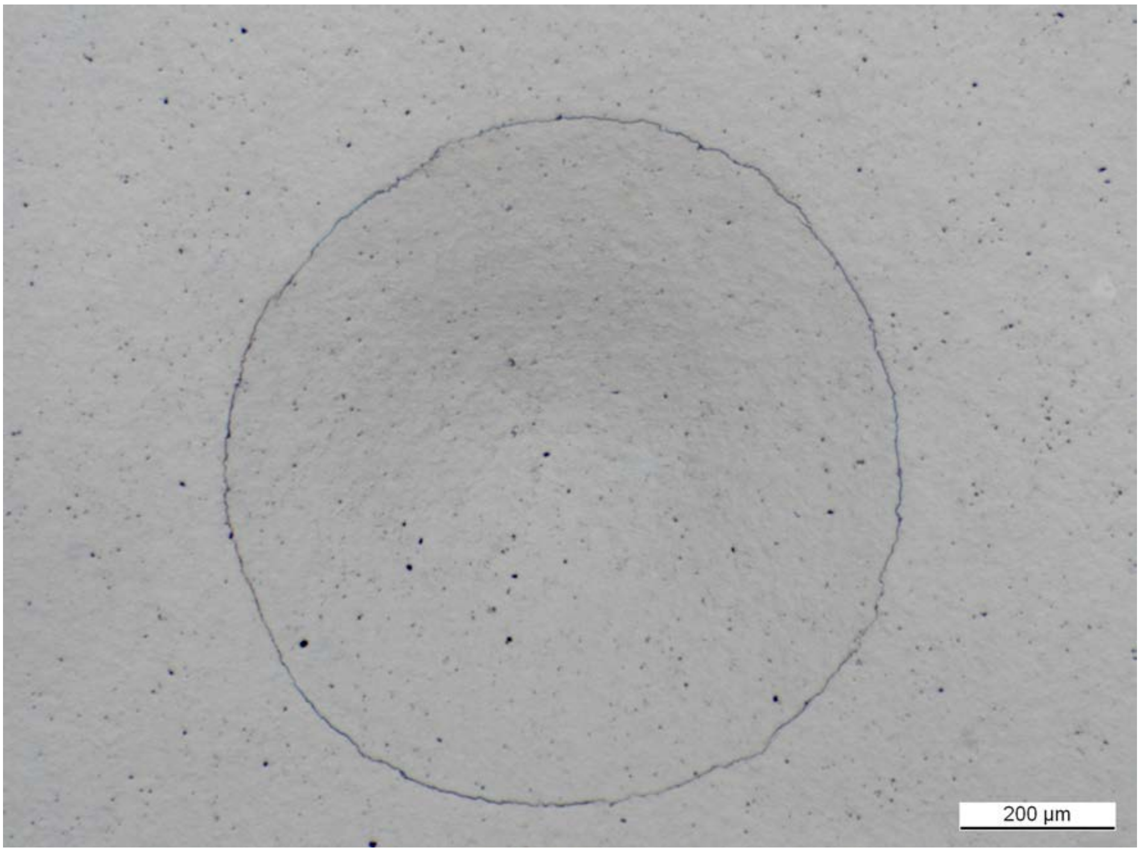

Figure 5.3: Optical micrograph showing a circular crack in a thermal spray coating (COMM1) after percussive normal impact (100 N, <100 cycles)

A circular crack typically forms on the around the edge of the impact crater. These are seen in other published work investigating brittle materials, including the fracture of glass [129] and ceramic thin film coatings on ceramic substrates[36]. Tillet [129] suggests that a ring forms when the tensile strength of a material is exceed at the edge of the contact, i.e. the crater edge, for a static or dynamic impact loading condition with a spherical counterface. If one considers the coating to act as an isotropic, homogeneous solid then such a criterion is useful when determining the point at which ring cracks appear with FEM techniques.

Radial crack

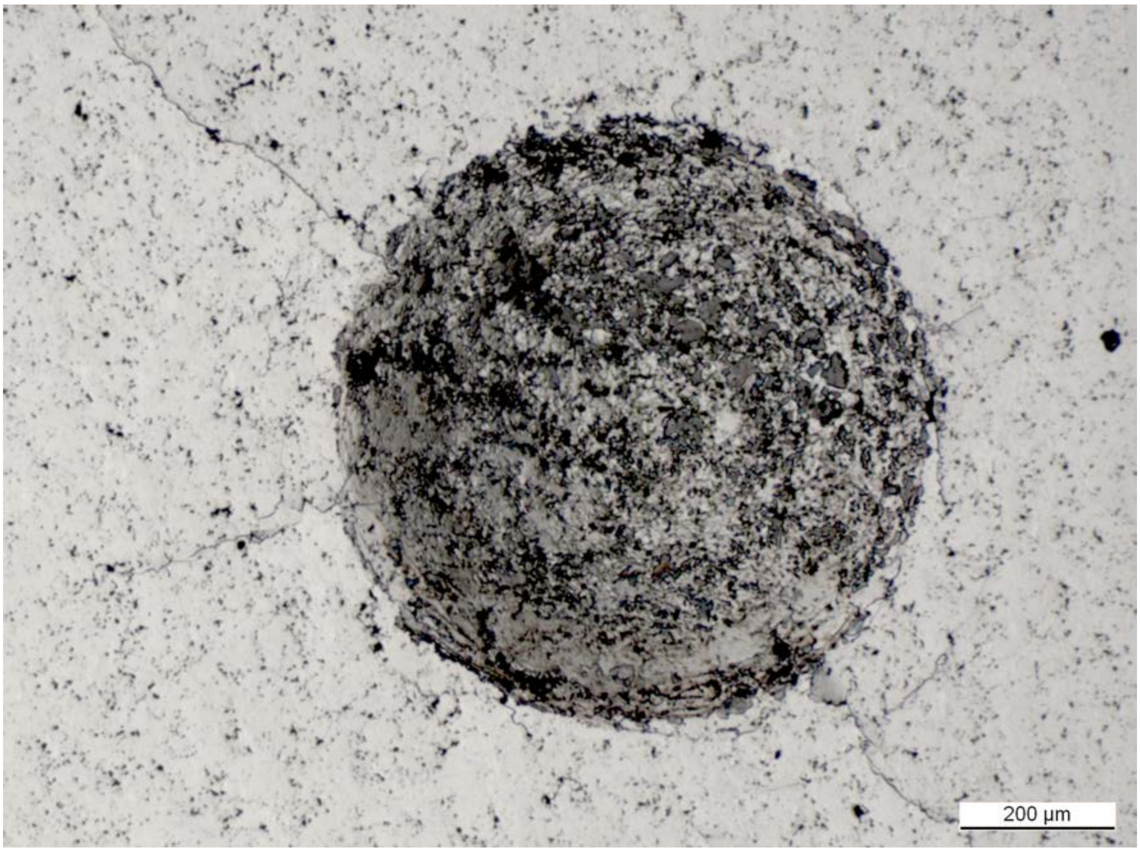

Figure 5.4: Optical micrograph showing a series of radial cracks in a thermal spray coating (EXP1) after percussive normal impact (100 N, 10k cycles)

Radial cracks are those which typically originate from the edge of the impact crater and propagate outwards. The cracks are often seen inside the impact crater, which implies that the impact crater diameter has increased over time. These generally develop after initial plastic deformation and the formation of the initial circular crack.

Blistering

Unique to EXP4, blistering of the upper layers of the multilayer coating was observed in the impact crater. Blistering is where the DLC film spalls from the thermal spray innerlayer. The blistered film may be partially worn or not present. An example of a blistering failure is given in Figure 5.5, with the site marked by the red circle in Figure 5.5a shown at increasing magnification in Figures 5.5b-d.

The DLC film appears to blister along cracks which form in the thermal spray innerlayer, directly below the impact crater. The cracks which enable blistering may be radial or circular. Where the TS innerlayer has not suffered significant cracking (i.e. visible by optical microscopy) , the DLC film does not show signs of blistering.

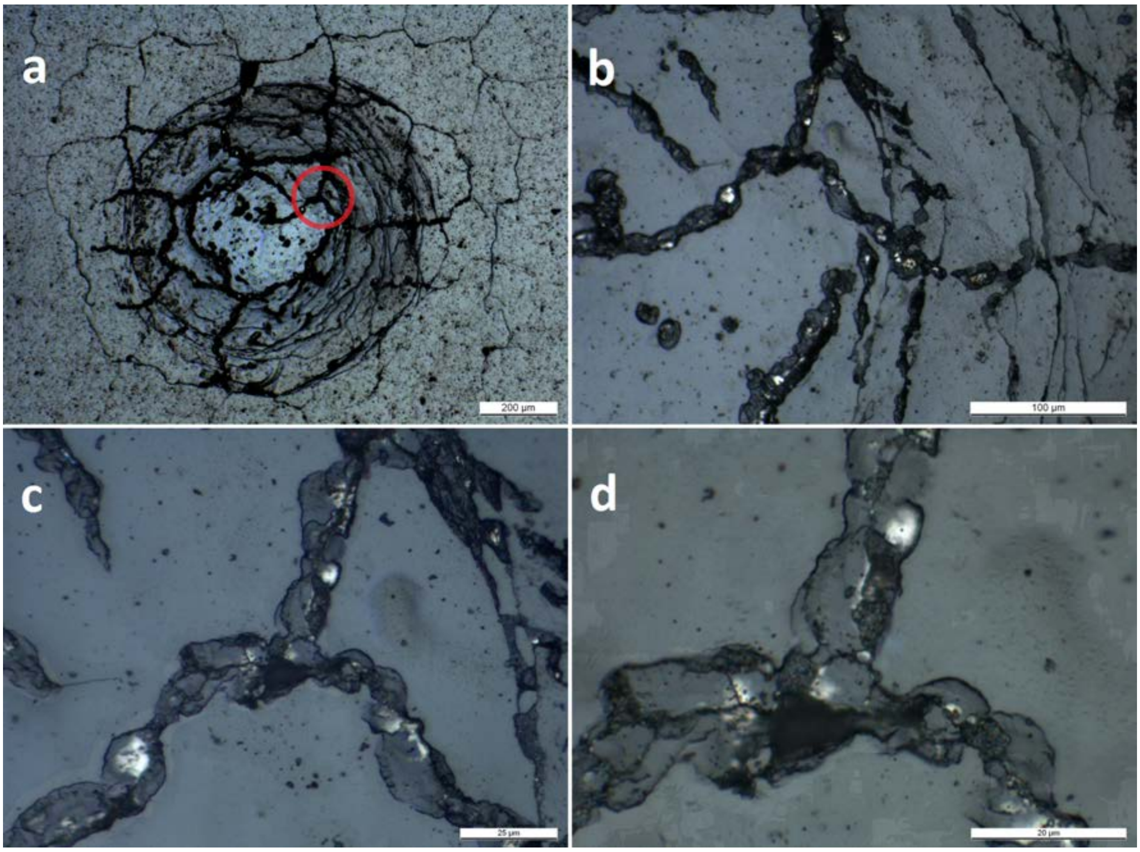

Figure 5.5: Optical micrograph showing blistering of the thin DLC film from the thermal spray innerlayer, after percussive normal impact (100 N, 50k cycles)

The cracking of the thermal spray (TS) inner layer may cause unfavourable stresses to develop at the interface between the TS innerlayer and the thin film DLC. Coupled with repetitive impact, this may cause the spallation and wear of the DLC film. As the TS innerlayer is damaged due to impact, it can be stated that the DLC film does not provide total protection against impact damage.

Pile up

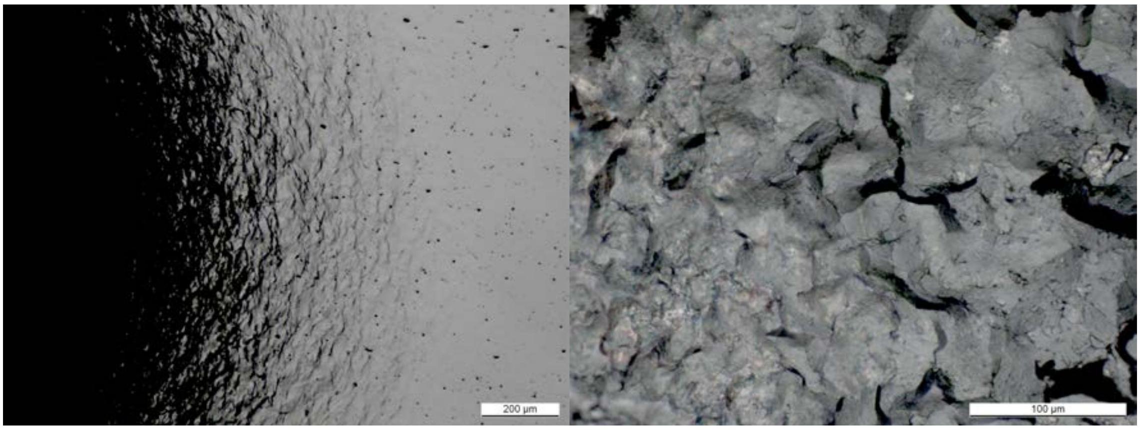

Figure 5.6: Optical micrograph showing high plastic deformation leading to pile-up of material around the crater edge for the substrate steel, Uddeholm Formax, after percussive normal impact (100 N, 50k cycles)

Pile-up is observed for those materials which tend to fail due to ductile failure leading to the build-up of material around the crater edge. It is observed for materials which failure due to ductile failure, i.e. the substrate material, Uddeholm Formax. As there is a positive build-up of material at the edge of the impact crater, it amplifies the effective crater dimensions (total depth, diameter) and leads to impressions above and below the surface. This would be problematic for a tribosystem which was prone to damage by impact and sliding conditions and where tight dimensional tolerances must be kept, e.g. for a good seal. A good example are the suspension stanchtions of a heavy, digger truck.

5.2.2 Description of the secondary impact failures for percussive normal impact

Sliding contact

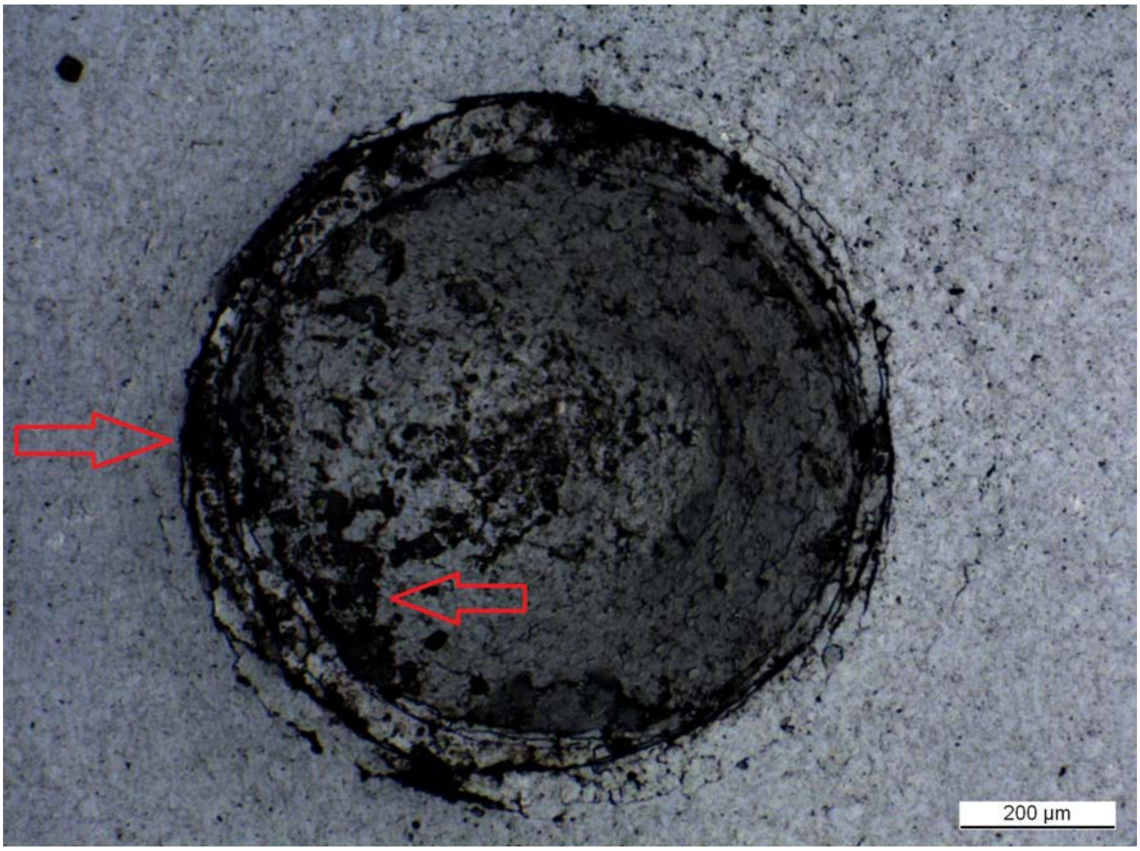

* Note that the regions marked with the red arrows demonstrate material loss due to fatigue and sliding wear

Figure 5.7: Optical micrograph showing a secondary damage caused by a sliding contact in a thermal spray coating (EXP2) after percussive normal impact (1750 N, 10k cycles)

Despite being a minor consideration, damage due to a sliding contact is observed. It is not a major failure mode. Contact between asperities of the counterface and impact specimen surface (i.e. two body abrasion and/or adhesion) and the counterface, impact specimen and wear particles (i.e. three body abrasion) are the key mechanisms responsible. Gouge marks are typically seen on the inside edge of the impact crater, often after a high number of impact cycles. See Figure 5.7.

Fatigue

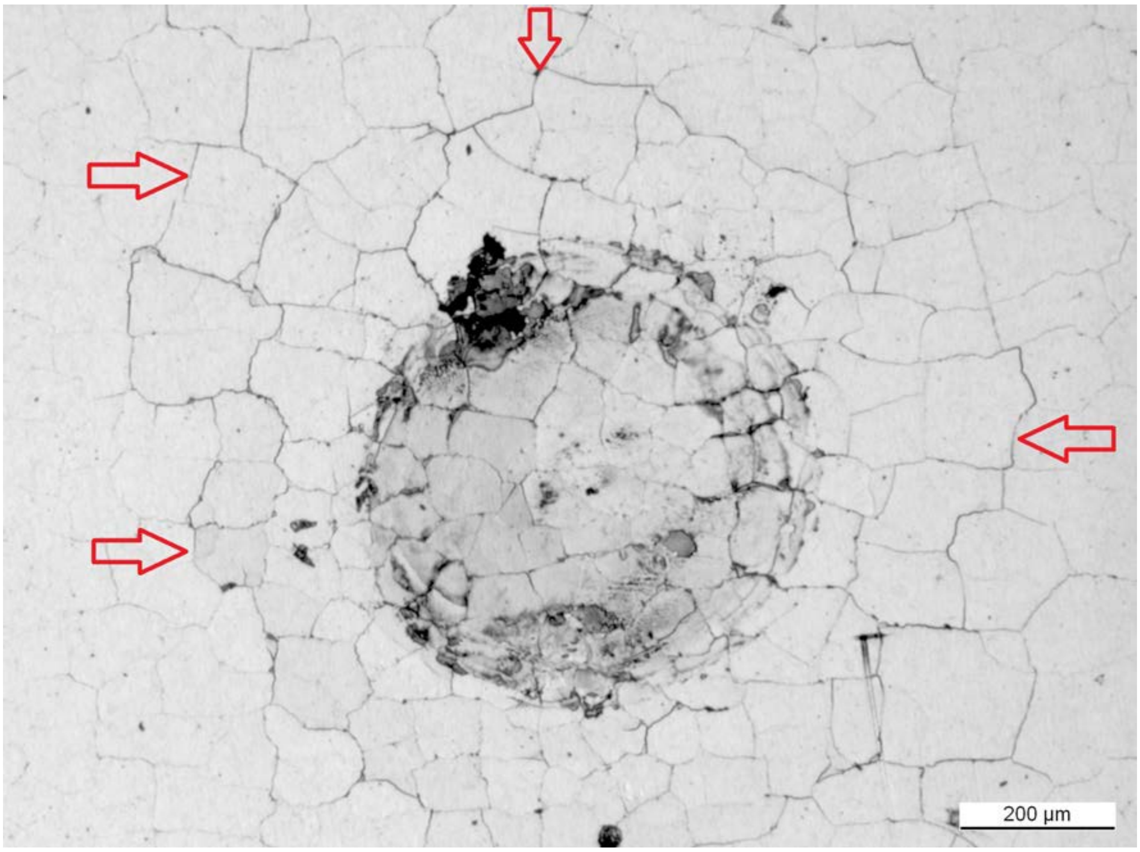

* Note that the red arrows mark fractures which formed due to fatigue away from the impact site

Figure 5.8: Optical micrograph showing a series of fatigue cracks in a thermal spray coating (EXP2) after percussive normal impact (100 N, 1k cycles)

In areas local to the evolving impact crater itself, but not within, the coating is damaged due to the repetitive dynamic loading contact. It is observed that the convergence of radial cracks and circular cracks leads to loss of coating material. An example is shown in Figure 5.8. The cracks quickly become thinner further from the crater edge.

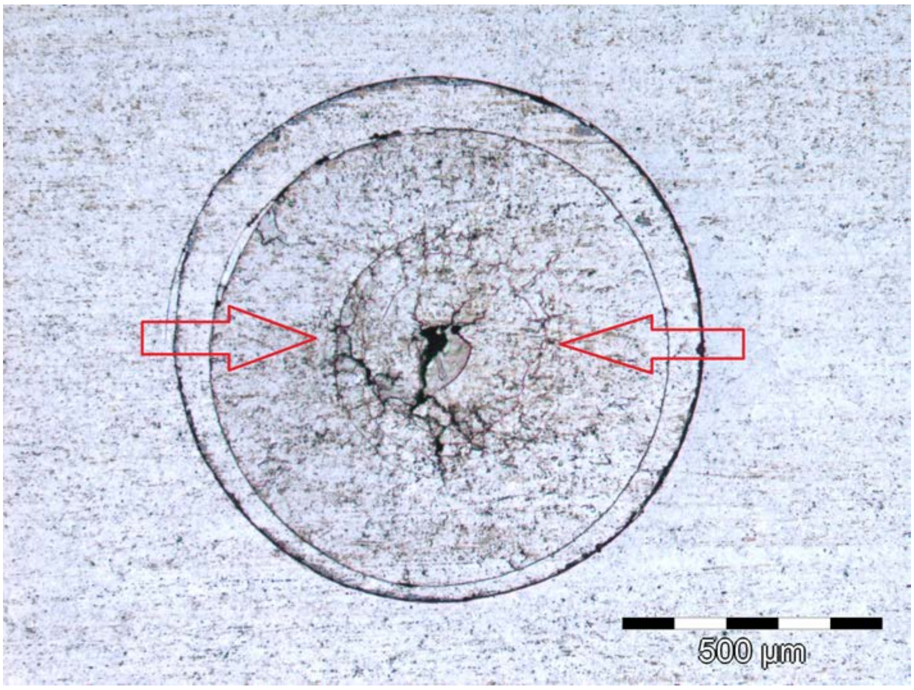

Figure 5.9: Optical micrograph showing fatigue damage due to contact loading, for EXP3 after percussive normal impact (1750 N, 1000 cycles)

Additionally, fatigue is also observed in the centre of impact crater, where it is subject to repeated loading by the impacting counterface. An example of this is given in Figure 5.9.

5.2.3 The evolution of failure and wear for percussive normal impact

The evolution of the failures described in Figure 5.1 correspond with the primary test parameters; impact load and number of impact cycles. Tables 5.2 and 5.3 give the first observation of each failure under percussive impact testing for low load and high loads respectively, as a function of the number of impact events.

Low load percussive normal impact

After successive impact events with a peak force of 100 N, it is clear that there is a spectrum of performance levels amongst the investigated materials. The minimum number of impact events, along with the maximum number of impact events at which it is observable, were recorded in Table 5.2. The failures were observed by optical or scanning electron microscopy.

Material	units	Crater formation	Circular crack	Radial crack	Blistering
EXP1	k	0.1 to 50	1 to 50	2.5 to 50	-
EXP2	k	0.1 to 50	1 to 50	-	-
EXP3	k	0.1 to 50	2.5 to 50	-	-
EXP4	k	1 to 50	2.5 to 50	-	1 to 50
COMM1	k	0.1 to 50	0.1 to 10	-	-
COMM2	k	0.1 to 50	0.1 to 5	-	-
COMM3	k	0.1 to 50	1 to 2.5	1 to 2.5	-
Steel	k	0.1 to 50	-	-	-

*Note that ’ - ’ indicates that the specified failure was not observed under the investigated conditions

Table 5.2: The range of impact cycles that key failures are observed for the investigated materials under percussive normal impact at peak impact force of 100 N

Of the four failure modes presented in Table 5.2, only two failure modes are consistently observed for the coated materials: crater formation and circular cracking.

Onset of crater formation After 100 impact cycles, a measurable crater has formed for all coatings except for EXP3. An impact crater is deemed measurable if a depression greater than 0.5 µm in depth can be measured using optical profilometry. An impact crater was always observable after 1000 impact cycles under the test conditions. With a sufficiently high number of impact cycles and sufficient impact loading, the test specimen may demonstrate gross spallation leading to total and widespread coating loss, however this was not observed. Under the test conditions, it is not possible to rank the materials with the onset of crater formation. For EXP3, a minimal impact crater was detected after 1000 impact cycles, with a depth of no more than two micrometers. Due to a strong resistance to plastic deformation, the coating did not exhibit measureable pile-up of material at the edge of the impact site.

Onset of circular cracking The next failure to occur was the formation of a circular crack. These formed early, generally by 1000 impact cycles and after no more than 2500 impact cycles. The experiemental arramgement did not allow online observation of the impact site and so it is not possible to identify the exact number of impact cycles that were required to form a circular crack. This is true for all of the other investigated failures. If the resistance to the formation of circular cracks can be used to imply impact resistance, EXP3 and EXP4 are the best performing coatings as they generally first appear after 2500 impact cycles. These two materials have significantly higher top-surface hardnesses compared to the other materials. As EXP4 is most similar to EXP2, with the addition of a DLC thin film multilayer, it can be stated that the DLC thin film multilayer offers some protection against circular cracking.

When comparing the role of coating material on the formation of circular cracks, it is clear that the harder WC-based coatings (EXP1-4, COMM2) offer significant protection compared to COMM2 (CrC-NiCr) and COMM3 (Mo-MoB-CoCr). In terms of materials processing for the experimental coatings (EXP1-4), it appears that the low temperature, high velocity (EXP3, HVAF) process is preferable.

The circular cracks were generally observable until 50000 impact cycles for EXP1-4. However, for COMM1-3, the circular cracks were not observable after a certain number of impact cycles. The impact crater edges are well defined with minimal cracking around the edge.

Tillett [129] suggested that a circular crack forms when the tensile strength is exceeded at the edge of contact between the spherical impacting body and the investigated sample for a single impact against spheres of varying diameter. [how can this be used?].

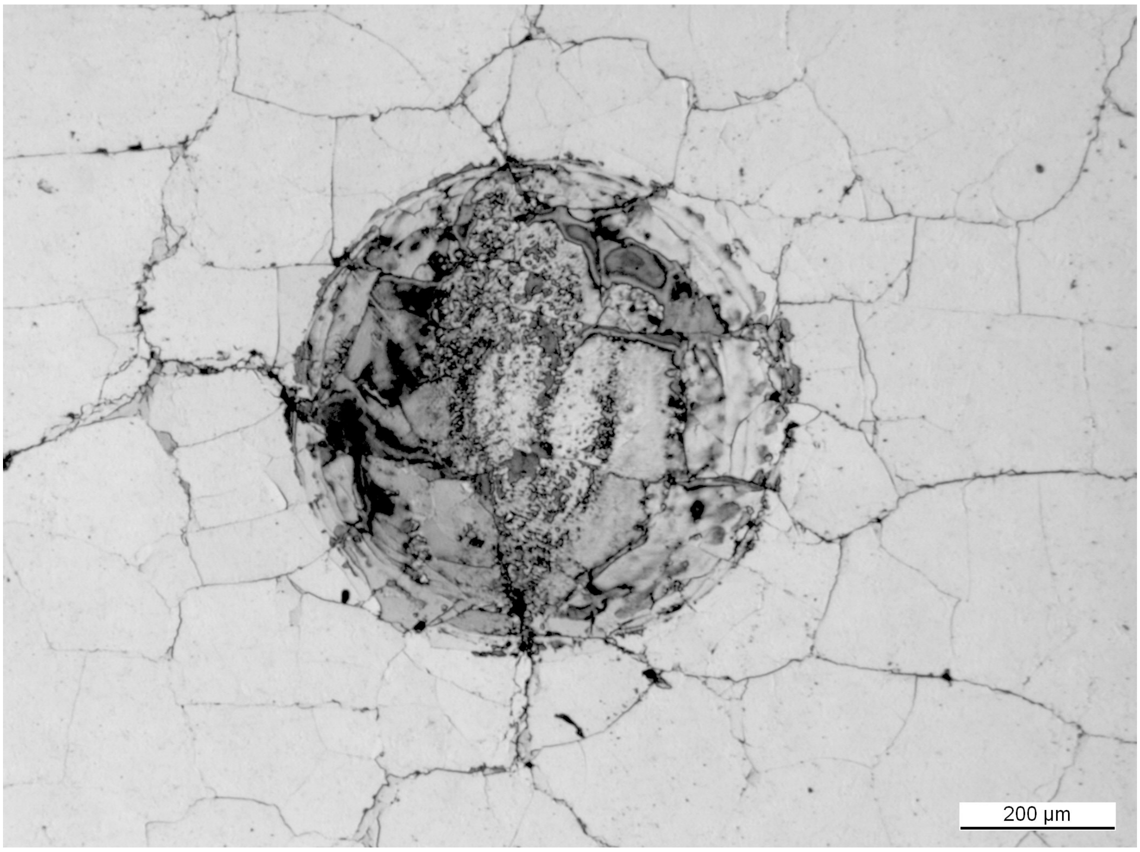

Figure 5.10: Extensive radial cracking of EXP1

Onset of radial cracking Radial cracks are primarily observed for EXP1 and COMM3. These materials also tended to develop well defined impact craters and clear circular cracks. The radial cracks may propagate 1-2 millimeters after 50000 impact cycles. Impact tests were performed to minimise the possibility that radial cracks from different impact sites could interact. Radial cracking indicates that the coating performs poorly under the investigated impact conditions.

Typically multiply radial cracks are observed, propagating from the impact crater outwards and they are reasonably evenly dispersed. They tend to initiate in the impact crater. It is suspected that they develop close to or from a circular crack or a local defect. It indicates the coating has insufficient fracture toughness and facilitates crack propagation more easily than the other coatings.

Onset of blistering Blistering is observed for EXP4 only and cannot be used as a means to compare the impact resistance of EXP4 against the other investigated materials. These materials do not have a thin film top multilayer and thus cannot demonstrate its local spallation. However it could be used to investigate similarly structured materials. The blisters formed over circular and radial cracks in the TS innerlayer which were not observed for EXP2. This indicates that the thin film multilayer promotes the formation of radial cracks.

In summary, the investigated failures had generally formed by 5000 impact events. After some critical number of impacts, the crater had formed sufficiently so that the peak stress due to impact was not sufficient to cause fracture. This is due to an increase in contact area, if the mechanical properties of the impacted surface material are assumed to have not changed. Thus, impact testing by this method is immediately useful when assessing the onset of failure modes (primarily by fracture) or an assessment of the deformation and wear by crater morphology assessment.

High load percussive normal impact

After successive impact events with a peak force of 1750 N, there is a spectrum of performance levels amongst the investigated materials. The minimum number of impact events cause each failure mode was recorded. The failures were observed by optical or scanning electron microscopy. Only materials EXP1-4 were assessed, due to limitations regarding access to the Caterpillar IonCoat I10 equipment, equipment reliability and that knowledge of the processing parameters is available.

Material	units	Crater formation	Circular crack	Radial crack	Blistering
EXP1	k	0.1 to 250	0.1 to 50	0.1 to 250	-
EXP2	k	0.1 to 250	0.1 to 20	-	-
EXP3	k	0.1 to 250	1 to 100	-	-
EXP4	k	0.1 to 250	1 to 250	-	1 to 250
Steel	k	0.1 to 250	-	-	-

*Note that '-' indicates that the specified failure was not observed under the investigated conditions

Table 5.3: The range of impact cycles that key failures are observed for the investigated materials under percussive normal impact at peak impact force of 1750 N

Onset of impact crater formation All coatings developed a visible impact crater after 100 impact events. This is in constrast to the low load investigation where EXP3 resolutely resisted crater formation by deformation or wear. The peak impact force strongly influences the onset of impact crater formation.

Onset of circular cracking As seen for low load tests, circular crack formation follows crater formation. Typically, a higher number of circular cracks are observed for a given number of impacts. This likely to be due to different loading conditions (e.g. peak impact load, impulse). As seen for the low load tests, EXP3 and EXP4 form circular cracks after a greater number of impact cycles compared to EXP1 and EXP2. For materials EXP1-3, circular cracks are not observed beyond a critical number of impact cycles (e.g. 20000 impact cycles for EXP2).

Onset of radial cracking As observed for the low load tests, EXP1 is the only coating which develops radial cracking. This is seen for all tests and it does not appear to terminate after a critical number of impact cycles.

Onset of blistering As for low load tests, EX4 is the only coating which develops blistering. It is observed for all impact tests and appears to increase in severity with the number of impact cycles. Unlike the low load tests, blistering is also observed in areas which appear to be unaffected by large circular or radial cracks. An example is given in Figure 5.11 where the blister sites can be observed in the centre of impact crater.

Zero wear and measurable wear

The onset of wear is difficult to identify, with respect to the number of impact cycles applied to the investigated material. Engel reasoned that a material will resist impact wear until a critical point, at which wear begins [3]. Henceforth, this shall be known as the zero-wear point (N_0). In most cases, the onset of wear is given in relation to the number of impact cycles. The impact curve is consistent and repeated for laboratory assessment, although this is unlikely to be true in an industrial environment. Thus, the zero-wear point is useful when comparing the impact resistance during laboratory assessments, yet additional work should be performed to enable correlation with the more variable impact cycling of industrial environments.

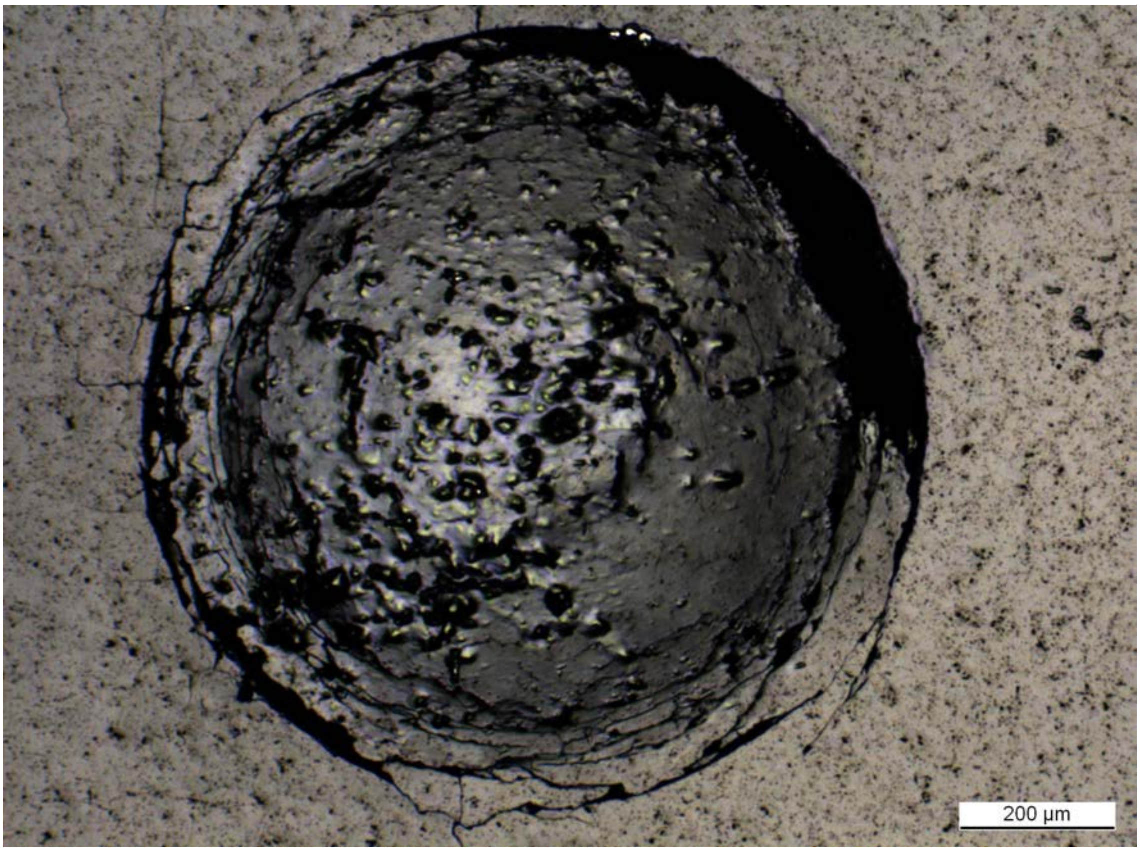

Figure 5.11: Optical micrograph showing blistering of EXP4 after percussive normal impact (1750 N, 50000 cycles)

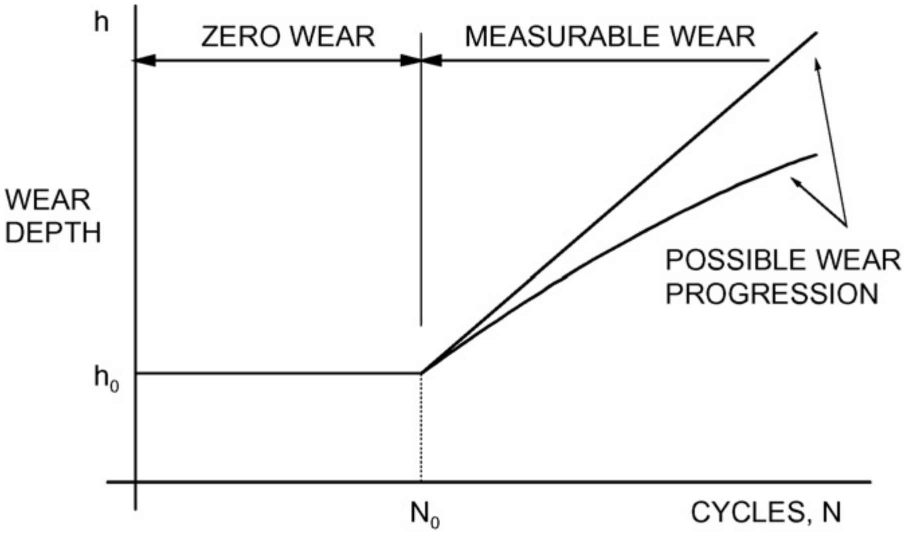

Figure 5.12: Engel's zero wear and measurable wear [3]

For the low load percussive normal impact assessment, all the investigated materials except for EXP3 demonstated crater formation before wear was visible from the crater surface. Thus, as it is difficult to distinguish wear from plastic deformation, the zero-wear point for those materials cannot be identified. However, for EXP3, the zero-wear point is beyond 50,000 impact cycles under the test conditions. Thus, EXP3 is the displays the highest percussive normal impact resistance under low load test conditions as wear nor plastic deformation are observed.

5.2.4 Crater morphology

The craters were assessed with confocal profilometry to define the crater shape, area and volume. For a given coating thickness, the crater dimensions can be used as a means to define the resistance to deformation and wear by percussive normal impact.

The peak crater depth was measured by recorded the difference in height (along the z-axis) between the lowest observed point of the impact crater and the assumed zero-plane of the undeformed top surface. The 3D profile was levelled and assumed to be flat. This is reasonable if the sample preparation was performed to a good standard. The peak crater depth does not differentiate between localised pitting, subcrater formation or wide-cracking. It is a simple measurement which can give an indication of the impact resistance. In some regards, it can be regarded as a measure of the dynamic hardness of the investigated materials.

Peak crater depth

At low impact force (100 N), the coatings offer a significant level of protection against deformation by impact loading. As shown in Figure 5.13, most coatings have a lower peak crater depth than the uncoated steel substrate material under the same conditions. All coatings, except COMM3, offered lower peak crater depths upto 35k impact cycles at 100 N. After 50k impact cycles, both COMM1 and COMM3 showed greater peak impact crater depths than for the uncoated steel.

At high impact force (1750 N), the the impact craters of the assessed coatings (EXP1-4) are generally lower than that for the reference steel when the total number of impact cycles is 100,000 or less. After 250,000 impact cycles, EXP2 and EXP3 have craters that are deeper than the reference steel. After 5000 impact cycles, the impact crater depth for the reference steel substrate does not increase proportionally with the increasing number of impact cycles. The steel will have undergone a significant degree of work hardening. Additionally, the contact area between the Tungsten Carbide counterface and the steel impact crater will be significantly higher than for the harder coated materials, which leads to lower stresses in the impacted volume.

Crater volume

The wear scar volume was found by the analysis software, PLμ Optical Imaging Software v2.31, when a base zero plane is establised. The reported wear scar volume did not take into account any material which was above the zero plane. Essentially, plastic flow of material above the base line was not considered. The effects of impact crater roughness, sub-craters and fracture surfaces on volume are all considered as the analysis uses the recorded profilometry data. Other researchers [3, 41] have assumed the wear scar shape as a spherical cap for ductile metals. However, this is not appropriate for the investigated materials which demonstrate brittle failure as well as ductile failure.

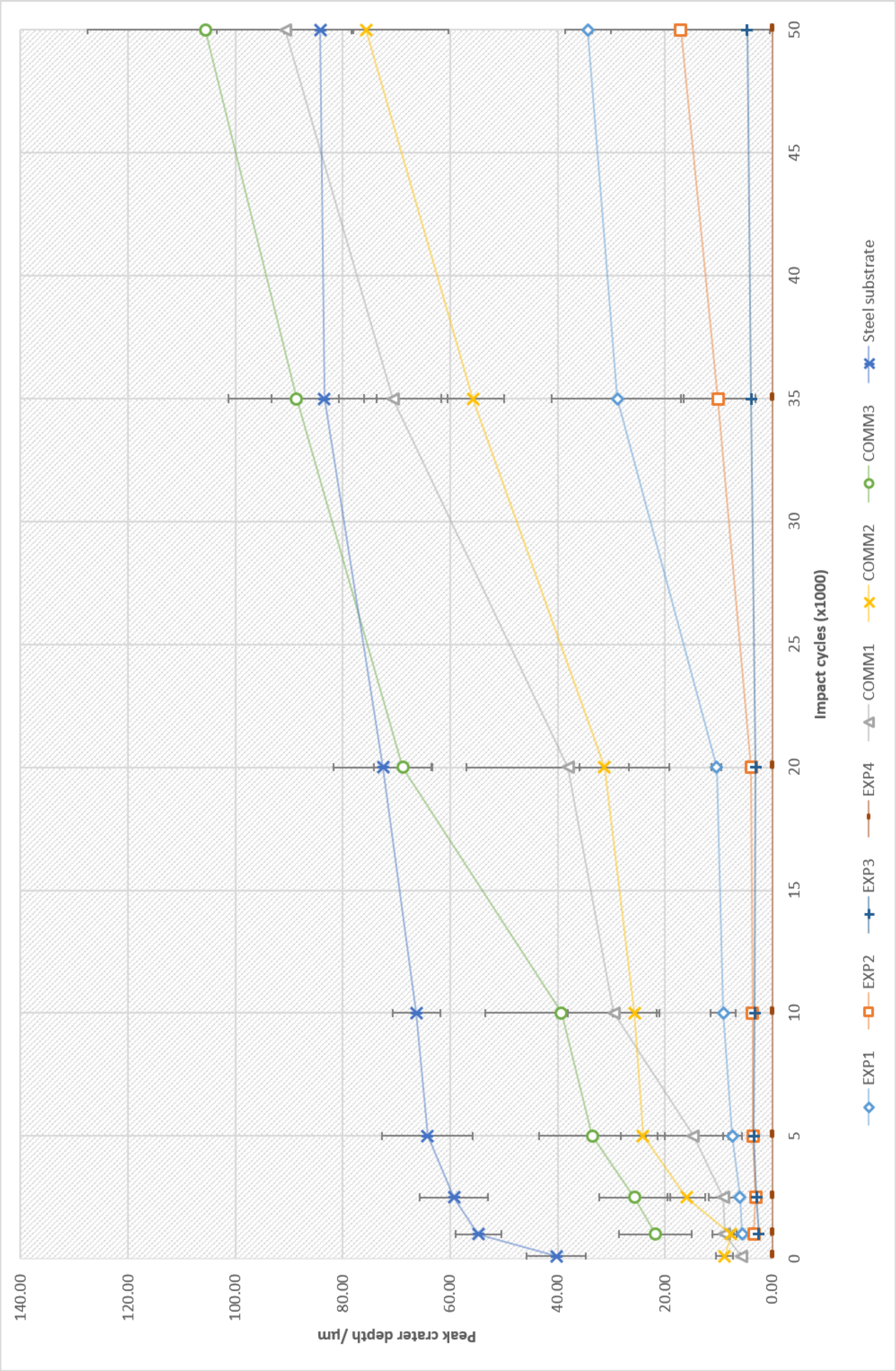

Figure 5.13: Scatter plot showing the peak crater depth vs. impact cycles for the investigated materials after low load percussive normal impact testing at 100 N

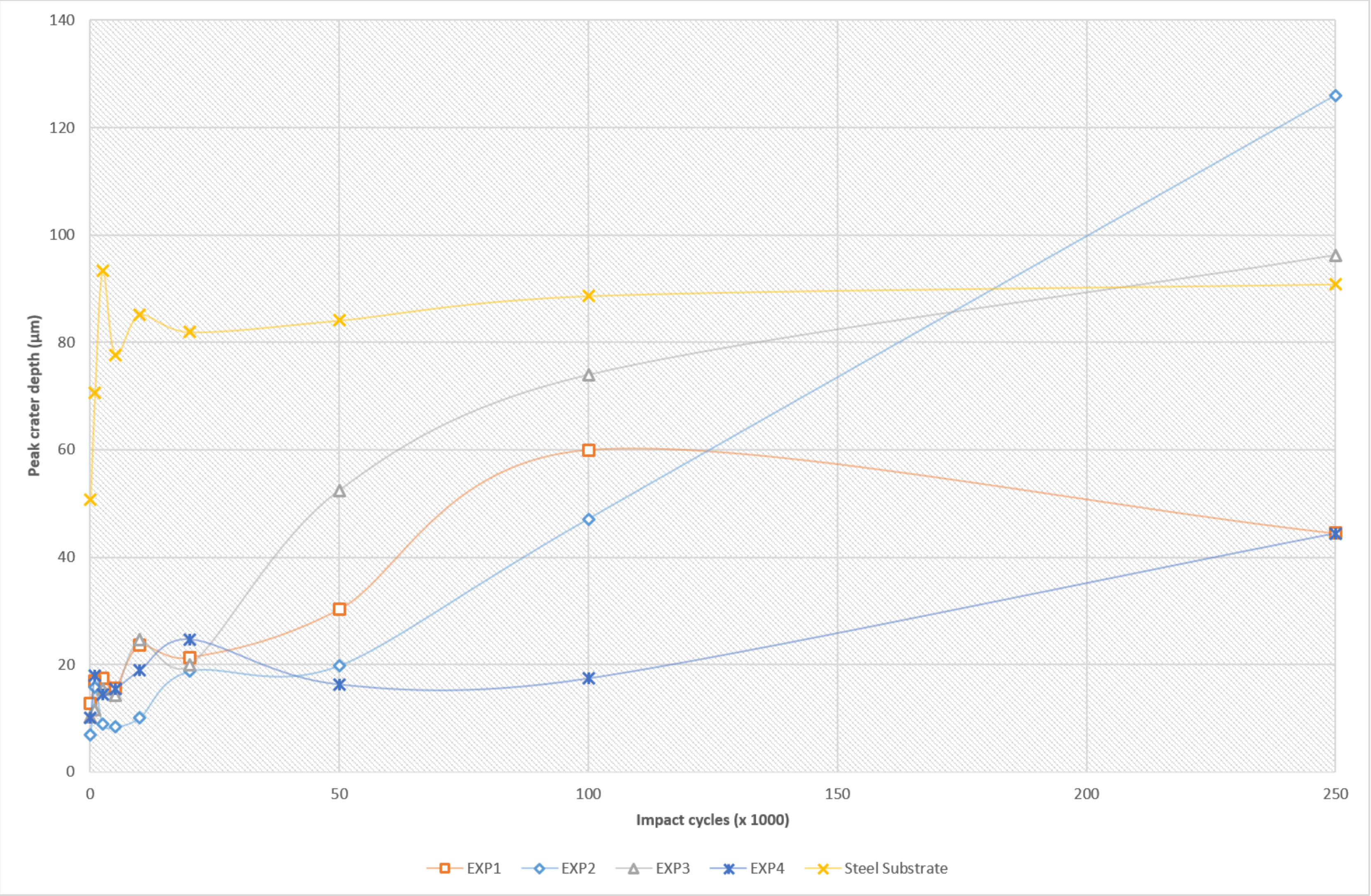

Figure 5.14: Scatter plot showing the peak crater depth vs. impact cycles for the investigated materials after high load percussive normal impact testing at 1750 N

5.3 Summary

The impact tests were performed with a hard, tungsten carbide ball. The number of impact events and the peak impact force were controlled.

Distinct failure modes were observed for the investigated materials. For the thermal spray coatings, the main failure modes are crater formation, circular cracking, radial cracking and fatigue. These coatings fail by ductile and brittle fracture. Conversely, the uncoated steel substrate demonstrated crater formation and pile-up of material due to plastic flow of ductile steel from the impact crater to the crater edge. The failure mechanisms for coated and uncoated steels are very different, making direct comparision difficult.

It is difficult to identify a clear zero-point for wear, i.e. the number of impacts that can be applied before the investigated material loses mass. Due to significant plastic deformation after a low number of impact events, measuring crater volumes does not accurately describe the wear of the system under percussive impact conditions. The wear rate could be better assessed by measuring mass loss, which was not performed. This is due to the suspected heavy compaction and adherence of wear debris in the impact crater which is difficult to remove. Thus, a mass loss method would underestimate the real wear rate.

When testing with low impact load (100 N), EXP3 did not develop a meaningful impact crater under the investigated conditions. It can be inferred that the tests performed were under the zero-point for wear.

Chapter 6

Single body compound sliding impact

6.1 Introduction

The investigated materials were subject to single, compound sliding impact assessment to investigate their performane under severe impact conditions. Tests were performed with the High Velocity Particle Impactor (HVPI) equipment at the Technical University of Tampere. The HVPI equipment propels a spherical projectile at the target sample. Features such as high deformation, significant wear and substantial fractures develop as a result of the test method. The impact events were monitored by high speed camera photography. The specimens are subject to impacts of increasing kinetic energy. A description of the investigation is given in Section 2.3.3. The impact sites were assessed by optical microscopy, SEM imaging and optical profilometry as described in Sections 2.1 and 2.3.3.

6.2 Description of primary impact failures for single compound sliding impact

The interpretation of the results is complicated as the contact evolves markedly over a short time period. A schematic diagram detailing the evolving contact is given in Figure 6.1. Just before the impact event, the target specimen is relaxed whilst the projectile is moving towards the impact site by translation and rotation. Upon impact, the projectile and target specimen deform as neither part can be can considered truly rigid.

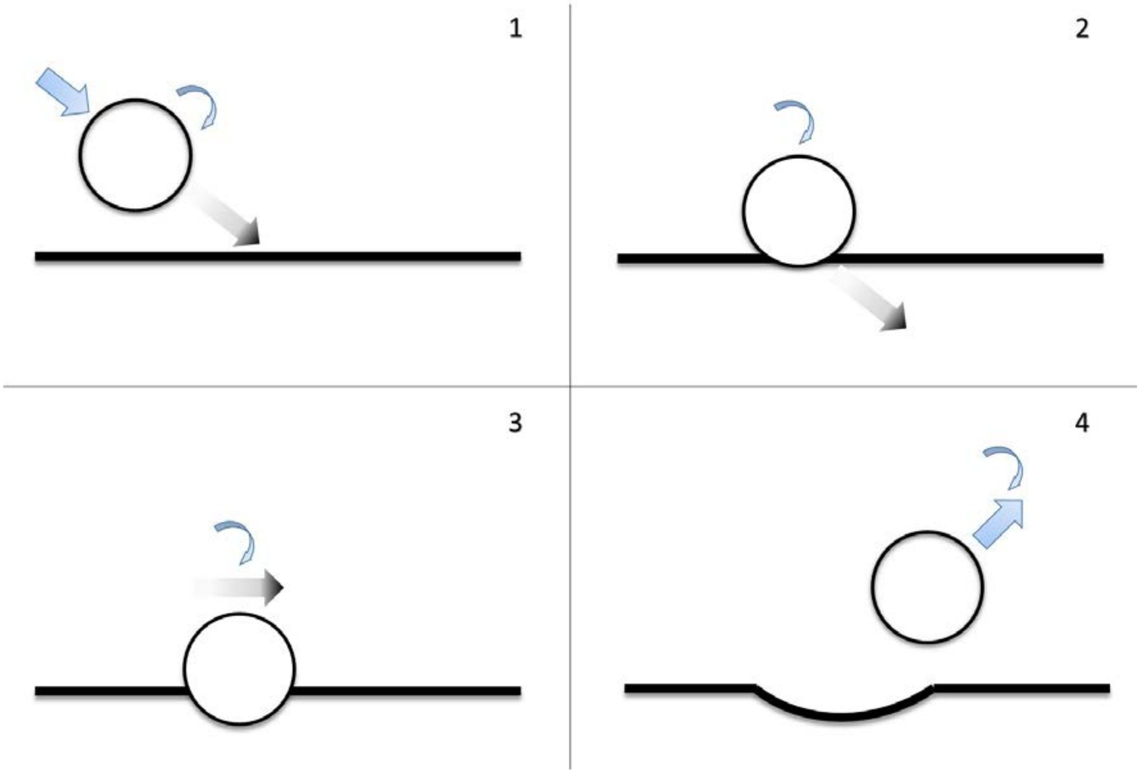

Figure 6.1: Schematic diagram describing the evolving contact between the target specimen and project for a single , compound sliding impact investigation

A schematic diagram presenting the typical failures is given in Figure 6.2. Every impact event created an impact crater which is visible by naked eye. Several circular and radial cracks also formed, which are usually observable with optical microscopy. The width and length of the circular and radial cracks increased with impact kinetic energy. Occaisionally, other features such as sub-craters, basal cracks, coating failures and delaminated regions were observed. These are described on the following pages.

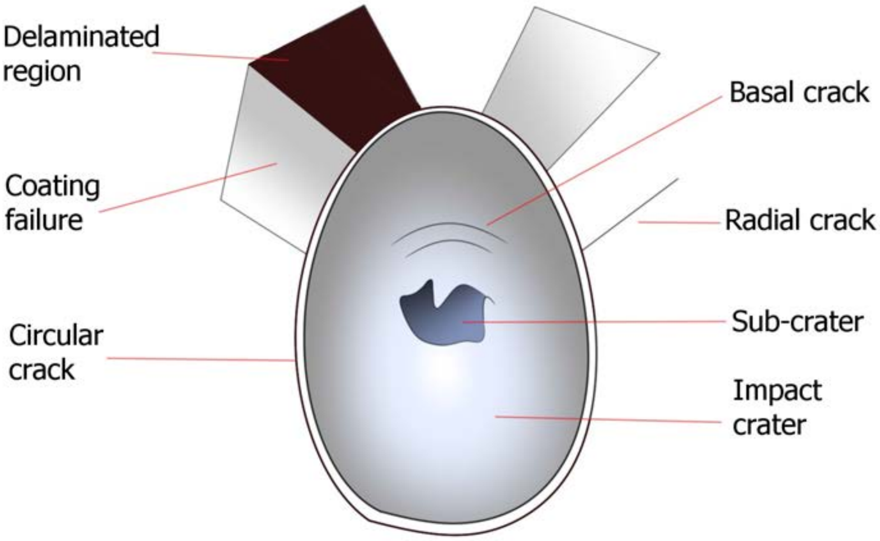

Figure 6.2: Schematic diagram showing the typical failures observed for the investigated thick, composite coatings after single body compound sliding impact testing

6.2.1 Crater formation

Crater formation is observed for all impacts. It caused by deformation of coating and substrate, and wear of the coating. The approximate impact crater length, width, area and volumes, as a function of impact kinetic energy, are presented in Figure 6.15. Craters can be observed in Figures 6.3 to 6.9.

6.2.2 Circular crack

All impacted surfaces have developed a circular crack which has propagated atleast 50 % of the crater perimeter. The circular crack is always observed behind the impact point and it may be observed along the crater perimeter in the general impact direction.

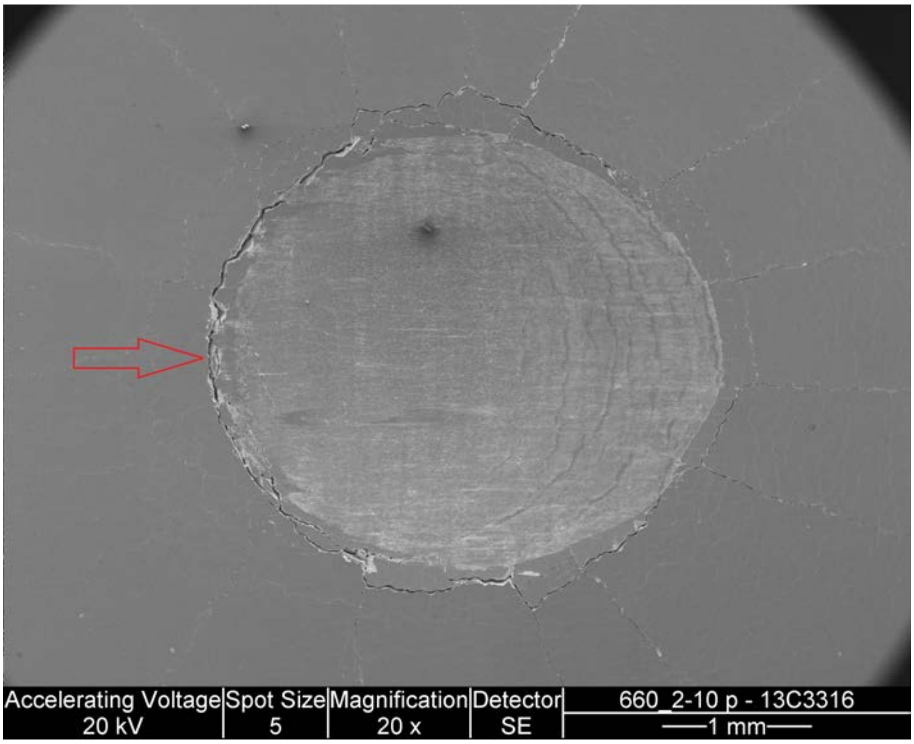

*The circular crack is shown by the red arrow. The projectile impact direction is left to right.

Figure 6.3: Scanning electronmicrograph showing high plastic deformation leading to plastic deformation of material around the crater edge for EXP2, after compound impact at 30º and XXX m/s

It is thought that a circular crack forms under similar condition for both normal percussive (see Chapter 5) and compound-sliding impact. As described earlier in Section 5.2.1, a circular crack forms due to high tensile stresses around the edge of the contact area between the impacting counterface and the static sample.

6.2.3 Radial crack

Numerous radial cracks are observed for impact tests across the range of kinetic energies tested. The radial cracks extend from the crater outwards in a radial manner. The radial cracks do not appear to originate from the circular crack and are assumed to form independantly.

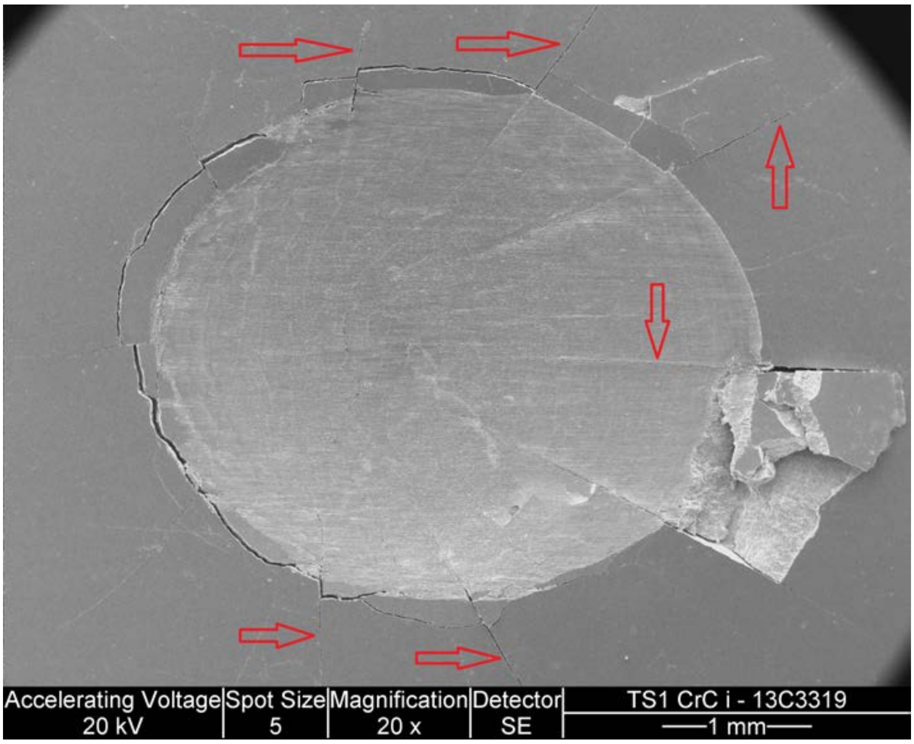

*The radial cracks are shown by the red arrows. The projectile impact direction is left to right.

Figure 6.4: Scanning electron micrograph showing radial cracks for COMM1, after compound impact at 30º and (4.5 bar) m/s

6.2.4 Cohesive spallation

For the investigated materials, there are two spallation-type failures; a cohesive spallation of the coating or an interfacial spallation between the steel substrate and the coating. These are comparable to the criteria defined for percussive impact testing in Figure 5.1. A cohesive delamination is discussed in this section, whilst an interfacial delamination event is discussed in Section 6.2.5.

An example of a cohesive spallation failure is seen in Figure 6.5, with a higher magnification image given in Figure 6.6. The cohesive spallation is seen to the right of the impact crater, where the projectile has impacted, slid and rebounded. The cohesive spallation is bordered by two radial cracks and the circular crack, whilst the exposed fracture surface propagates away from the impact crater.

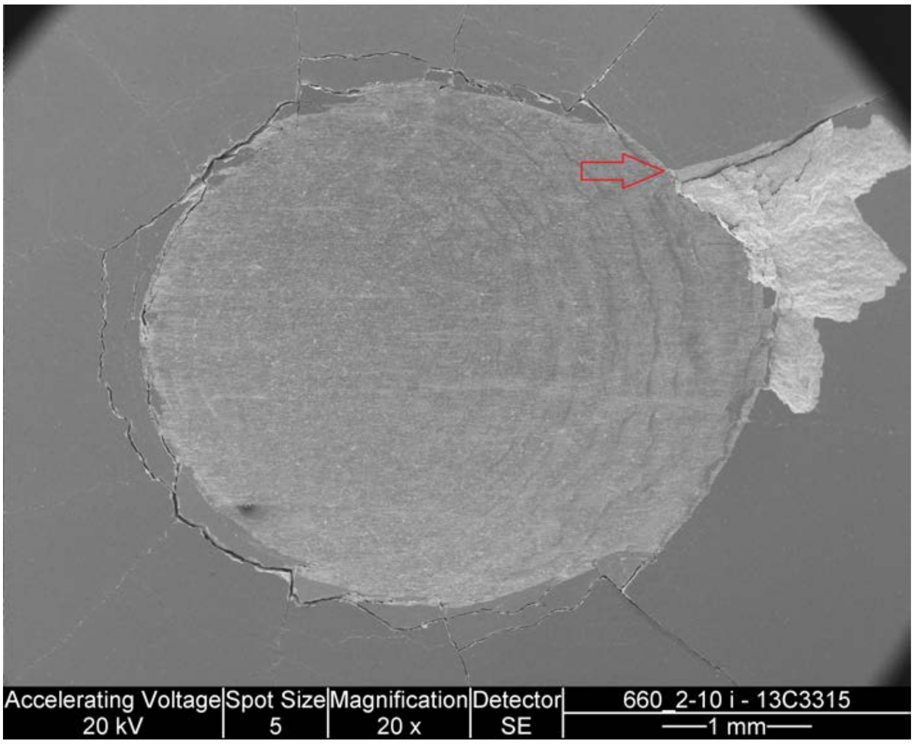

*Note that the delamination site is shown by the red arrow. The projectile impact direction is left to right.

Figure 6.5: Scanning electron micrograph showing high plastic deformation leading toloss of material around the crater edge for EXP2 by cohesive spallation, after compound impact at 30º and XXX m/s.

A cohesive spallation failure is where the peak depth of the exposed region ahead of the impact crater is less than the expected coating thickness. The material ahead of the impact crater is not expect to suffer any plastic deformation, i.e. volume loss, as it has not been directly loaded by the projectile and some material may even be pushed forwards to create a positive lip. However, wear may develop due to the action of elastic stress waves in the coating after impact, due to microfracture.

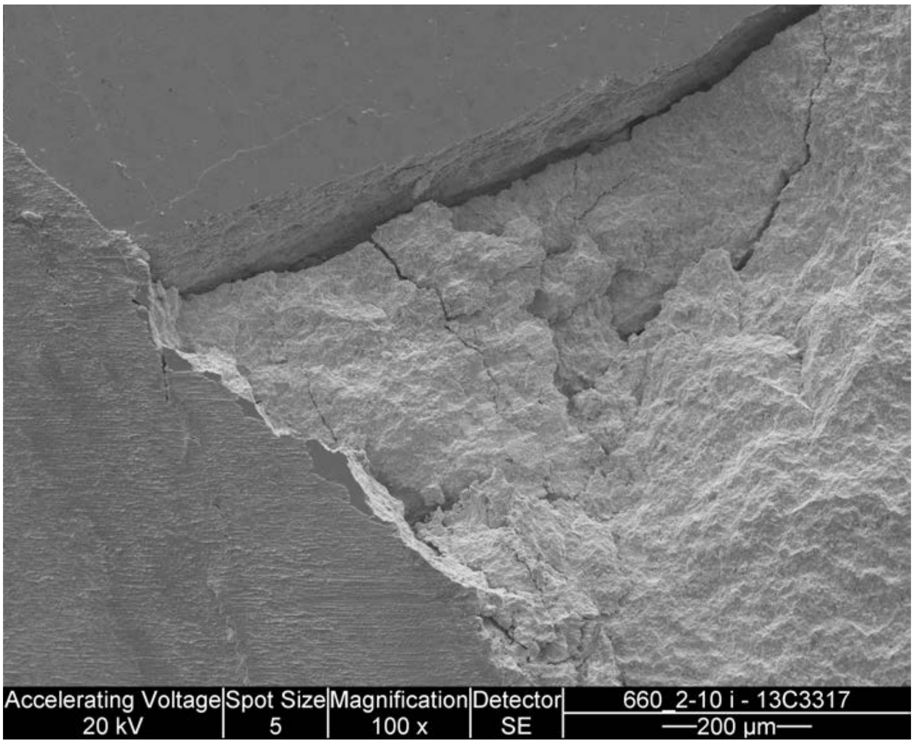

*Note that the image shows the delamination site shown in Figure 6.5 at higher magnification. The projectile impact direction is left to right.

Figure 6.6: Scanning electron micrograph showing a cohesive spallation failure site around the crater edge for EXP2, after compound impact at 30º and XXX m/s.

A cohesive spallation failure does not extend through to the substrate-coating interface and does not include plastic deformation of the substrate. The ejection of material as loose debris is confirmed by high speed video photography of the impact event. An high speed photography still for an impact test against COMM3 is given in Figure 6.7.

During the impact event, the projectile moves along the impact surface, eventually penetrating into the coating and substrate volume. This leads to material being pushed ahead of the projectile whilst the projectile is in contact with coated surface, as shown in Figure 6.2. The contact time is low and so the loading rate is high. At high loading rates, the coating is likely to behave as a brittle material capable of fast fracture,

Figure 6.7: High speed video frame of an impact event showing the ejection of debris due to a compound impact sliding event for a spherical steel projectile against COMM3

which is demonstrated by the heavy wear and large size of debris.

Beyond the investigated conditions, it is possible that the cohesive spallation volume may extend beyond the confines of two radial cracks or the circular crack if the impact conditions are sufficiently severe. The severity may increase by an increase of the frictional losses, increased contact pressure due to increased projectile kinetic energy prior to impact, change of projectile material or reduced cohesive coating strength (e.g. splat-splat interfacial strength).

An image of a damaged impact speciemen showing severe cohesive spallation is given in Figure 6.8. The failure zone has undergone high wear. A number of radial cracks which propagate from the inner impact crater are visible and these clearly influence the wear pattern ahead of the impact crater by the formation of ridges.

The majority of the fracture surface lies ahead of the impact crater, however some material is lost in the lower section of the impact crater presented in Figure6.8. In this case, the locally worn volume appears to be partially confined by the remains of two radial cracks, yet the perimeter circular crack does not contribute. Numerous minor circular cracks are visible inside the crater and these may be cruicial to the formation of cohesive delaminations within the impact crater.

It is seen in Figure 6.6 that the fracture surface is rough and highly textured. It

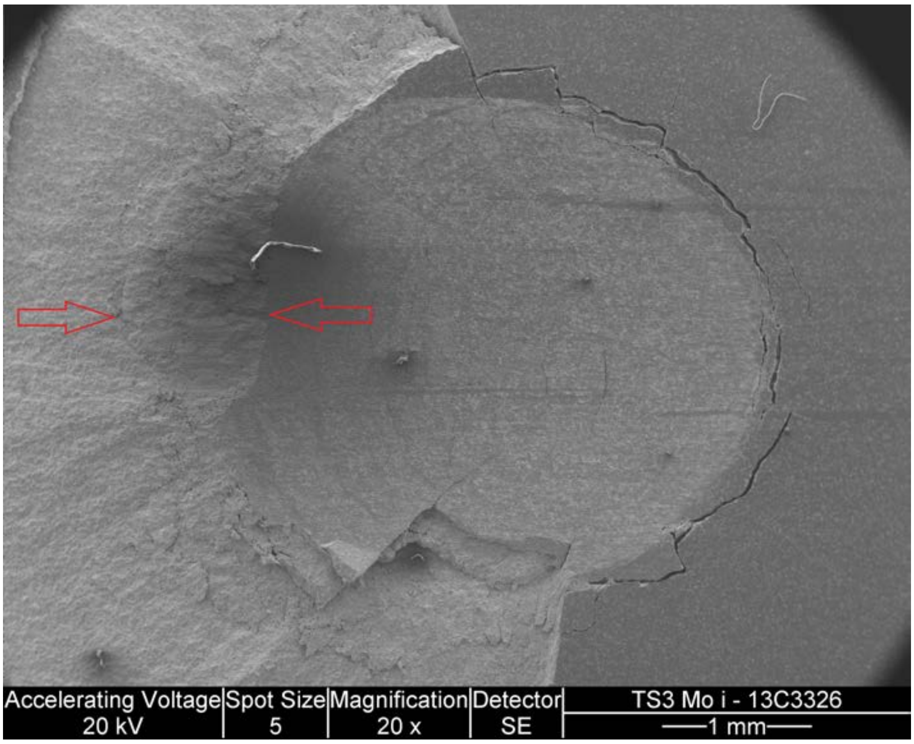

* Note that the region between the two red arrows is the severe cohesive delamination failure zone

Figure 6.8: Severe cohesive spallation of COMM3 after a single compound impact-sliding contact of XXX m/s and an impact angle of 30 °

is likely that the fast fracture propagated through components of the thermal spray coating which are characteristically weak. These may include splat-splat interfaces, carbide-matrix interfaces, other such interfaces and through brittle volumes themselves. Typically, these components are small and may encourage a rough fracture surface to develop.

Additionally, the circular crack and radial crack seen in Figure 6.6 are seen alongside fine cracks in the fracture surface. When assessing such impact craters, it is important to recognise that not all cracks are visible optically.

6.2.5 Interfacial spallation

A limited number of impact tests lead to a spallation event where the substrate-coating was exposed, which is called an interfacial spallation.. The coating has failed completely and it is not able to protect the substrate material. Under some operation conditions, such as impact-corrosion where the coating provides corrosion protection, this may be a terminal failure and force the retirement of the product until repair or replacement.

An example of an interfacial spallation is given in Figure 6.9, with a higher magnification image of the exposed substrate in Figure 6.10. The failure is similar to that observed for cohesive spallation (see Section 6.2.4, as it is bordered by two radial cracks. The edge of the impact crater overlaps the interfacial spallation site, as observed for a severe cohesive spallation, as shown in Figure 6.8.

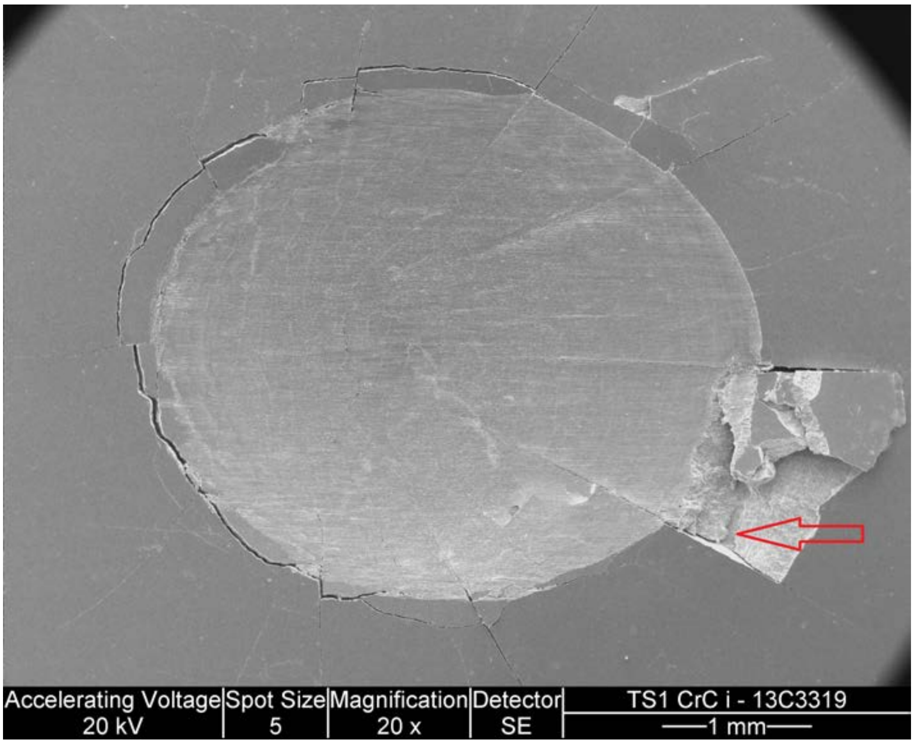

*Note that the interfacial spallation failure site is marked by the red arrow

Figure 6.9: Interfacial spallation failure for COMM1 after a single compound impact-sliding contact of XXX m/s and an impact angle of 30 º

As seen in Figure 6.10, the radial crack appears to extend through the coating thickness to the substrate top surface. The exposed area, as noted by the red arrow and site 4 in Figure 6.10, has a similar texture to the fracture surfaces of the coating inside the interfacial spallation site (sites 2 and 3). Sites 2 and 3 are essentially formed due to cohesive spallation failures. It is possible that a thin coating layer is still adhered to the interfacial spallation area (site 4) at the supposed interface, which would be in good agreement with the observation about similar surface texture.

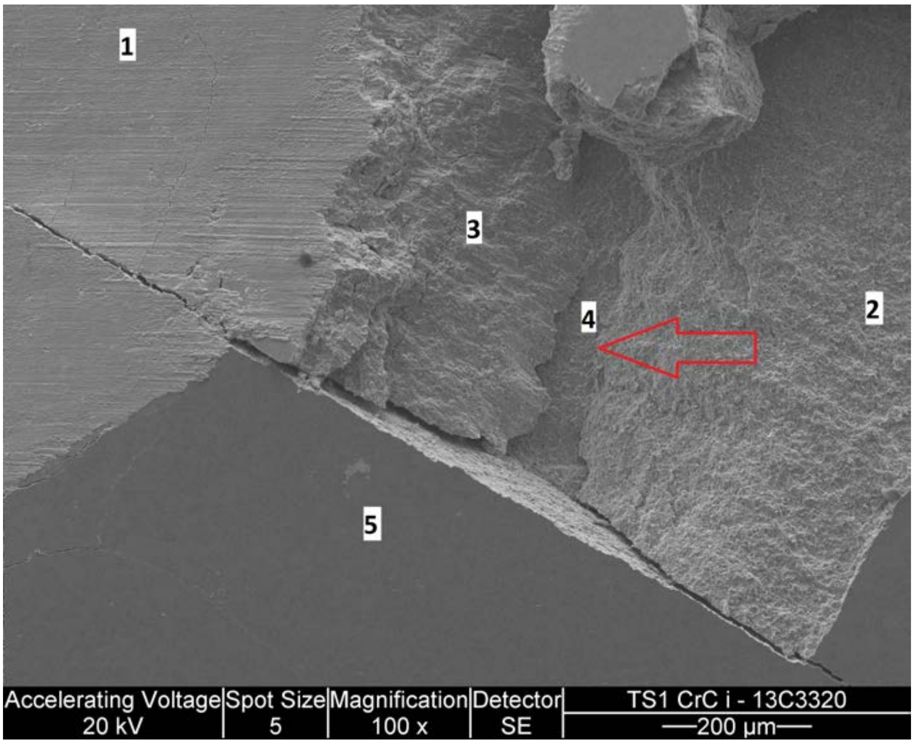

*Note that the interfacial spallation failure site is marked by the red arrow

Figure 6.10: High magnification SEM image of an interfacial spallation failure for COMM1 after a single compound impact-sliding contact of XXX m/s and an impact angle of 30

The atomic composition of sites 1, 4 and 5 were checked by SEM-EDS. Sprectra indicating which elements are found for area analysis are presented in Figure 6.11. Site 5 is the reference from which sites 1 and 4 will be compared. Site 5 is relatively undamaged as it has neither been in direct contact with the projectile, it has not suffered severe fracture and the coating appears to be flat and level, i.e. in the same condition as found before impact. Site 5 should be representative of an untested, polished coating. EDS analysis indicates the presence of Chromium (Cr), Carbon (C) and Nickel (Ni), which is consistent with the expected elemental composition of this coating.

Site 1 is inside the impact crater, nearer to the exit region which is in contact

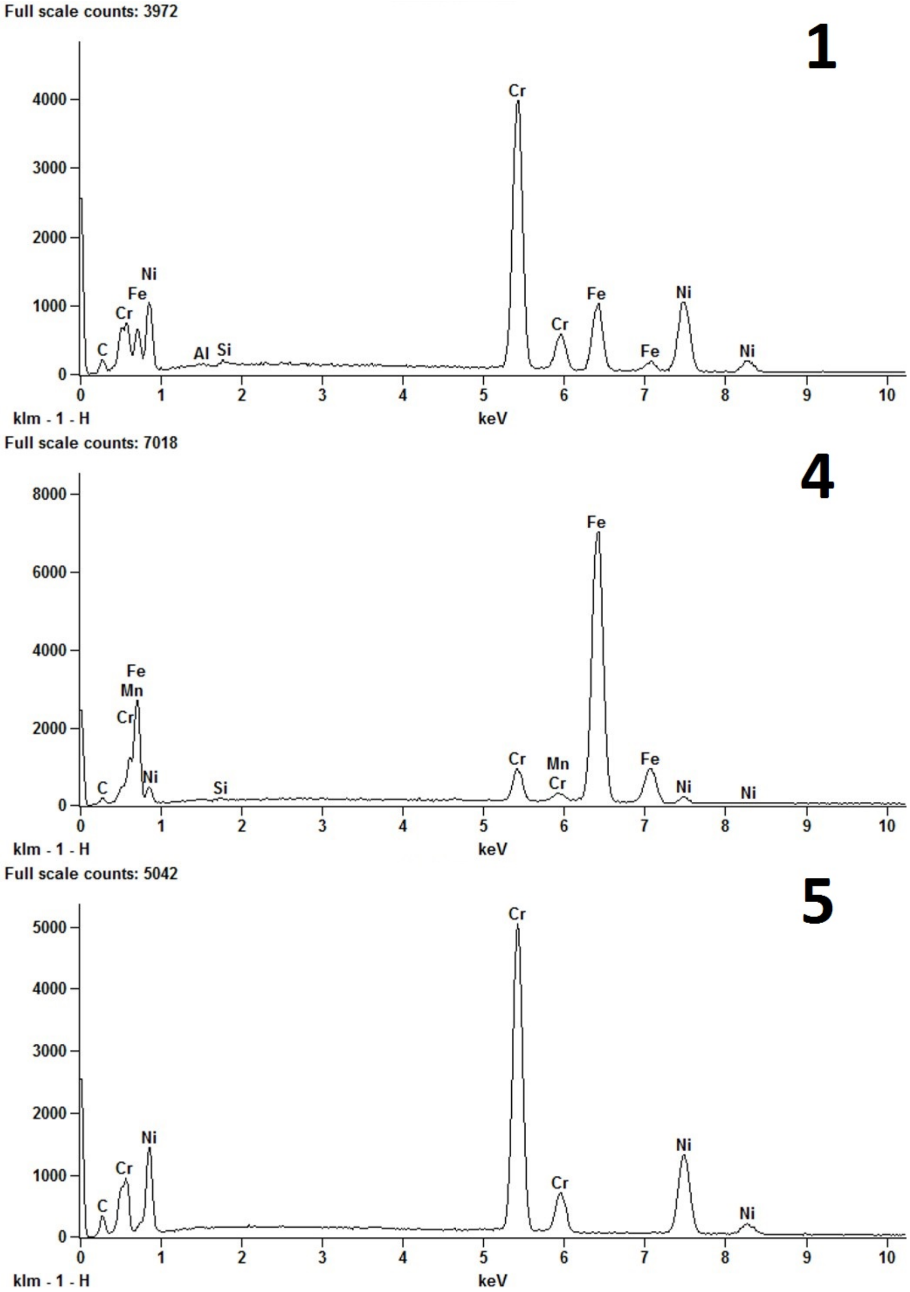

Figure 6.11: SEM-EDS results for an interfacial delamination failure site for COMM1 after a single compound impact-sliding event at XXX m/s and 30º impact angle

with the steel projectile during the impact event. According to EDS spectrum 1, Iron (Fe) is detected in addition to the expected Cr, C and Ni. Manganese (Mn) is also detected however the detected peaks are very similar to those of Fe and should be disregarded. The detection of Iron confirms the transfer of material from the steel projectile to the impact surface. This is reasonable as the coating is still very thick and the coating-substrate system has been significantly deformed plastically whilst maintaining a thick layer of adhered CrC-NiCr coating. The surface at Site 1 is marked with globular features which are striated along the impacting direction. It is likely that these globules are elemental Iron, Iron Oxide or a compound of Iron, Oxygen and another of the constituent elements of COMM1.

At the suspected interfacial spallation failure area, site 4, SEM-EDS analysis detects a similar elemental spectrum as for site 1. The key primary difference is that a greater relative quantity of Iron is detected, if one assumes that the number of elemental counts is proportional to the atomic quantity of a particular element. The increased detection of Iron can be explained by the higher local Iron content in the electron interaction volume underneath the electron beam. As the coating is either non-existant or very thin at Site 4, it is reasonable that a significantly higher Iron count is present. As the electron interaction volume is likely to be larger than the potential coating thickness, it cannot be absolutely verified whether the coating is present or not. For this reason it is not certain whether the failure is due to a cohesive failure or an interfacial failure by SEM-EDS assessment.

6.2.6 Summary of compound sliding-impact failure modes

There are six distinct and identifyable failure modes for the investigated material after single compound sliding-impact assessment. These are crater formation, circular crack, radial crack, the formation of a subcrater, cohesive spallation and interfacial spallation. Crater formation, radial cracking and both spallation failures are visible by naked eye. In terms of maintaining the ability of the investigated materials to support an applied load, all failures listed except for crater, circular crack and subcrater formation can be regarded as critical, i.e. unable to sustain a high load without causing deformation or damage to the substrate material.

6.3 Evolution of failure and wear for single compound sliding impact

Each impact test was investigated to detect whether any of the failure modes described in Section 6.2 developed and at what projectile kinetic energy they had formed. In Table 6.1, the earliest occurance of each failure mode for the investigated materials under the described test conditions is presented. The failures were identified with optical microscopy, SEM and optical profilometry as detailed in Chapter 2.

Material	Crater formation	Circular crack	Radial crack	Subcrater formation	Minor spallation	Severe spallation
EXP1	5 J	5 J	5 J	6 J	11 J	17 J
EXP2	5 J	5 J	5 J	5 J	16 J	-
EXP3	5 J	5 J	5 J	5 J	11 J	-
EXP4	5 J	5 J	5 J	5 J	-	-
COMM1	5 J	5 J	5 J	-	16J	-
COMM2	5 J	5 J	5 J	5 J	-	17 J
COMM3	5 J	5 J	5 J	-	-	5 J

* Note that '-' indicates that the specific failure was not observed

Table 6.1: Observed failures for each tested material as a function of the peak kinetic energy of the projectile

All impacts created an impact crater which was visible by the naked eye. The crater is permanent and forms as a result of plastic deformation of both the coating and the substrate. The crater depth is never more than XX% of the sample thickness, yet it is comparable to the coating thickness. All of the investigated materials formed an impact crater at the lowest impact kinetic energy, 5 J. Thus, the onset of crater formation by impact kinetic energy cannot be used to quantitively rate the impact performance of the coatings under this impact loading regime. Regardless, the form of the impact crater (length, width, depth, aspect ratio, volume, area) can be used to infer which coatings offer greater protection for the steel substrate material. These results are presented in Figure 6.15 and are discussed in Section 6.3.1.

Additionally, all impact events caused the formation of a circular crack around a section of the impact crater. The circular crack was found at the end of the impact crater which is near to the initial impact, before the projectile ploughs and slides through the investigated coating system.

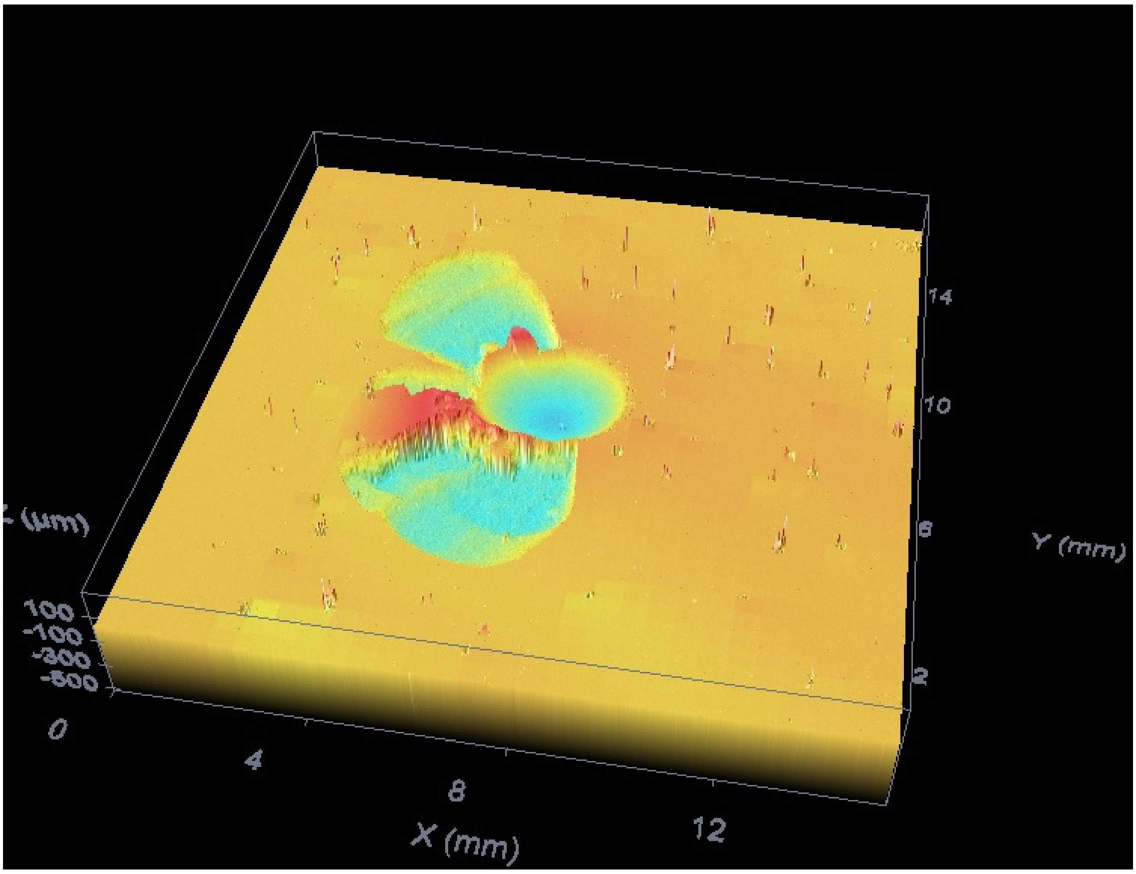

Figure 6.12: 3D interferometry profile of an impact crater for COMM3 after an impact event of 2 J at 30º

6.3.1 Crater morphology

The impact craters were assessed by optical microscopy, SEM imaging and 3D profilometry. Measurements including the crater length (a), crater width (b), crater depth (d) and crater top-surface area (A) were recorded. A diagram defining each measurement is given in Figures 6.13, 6.15.

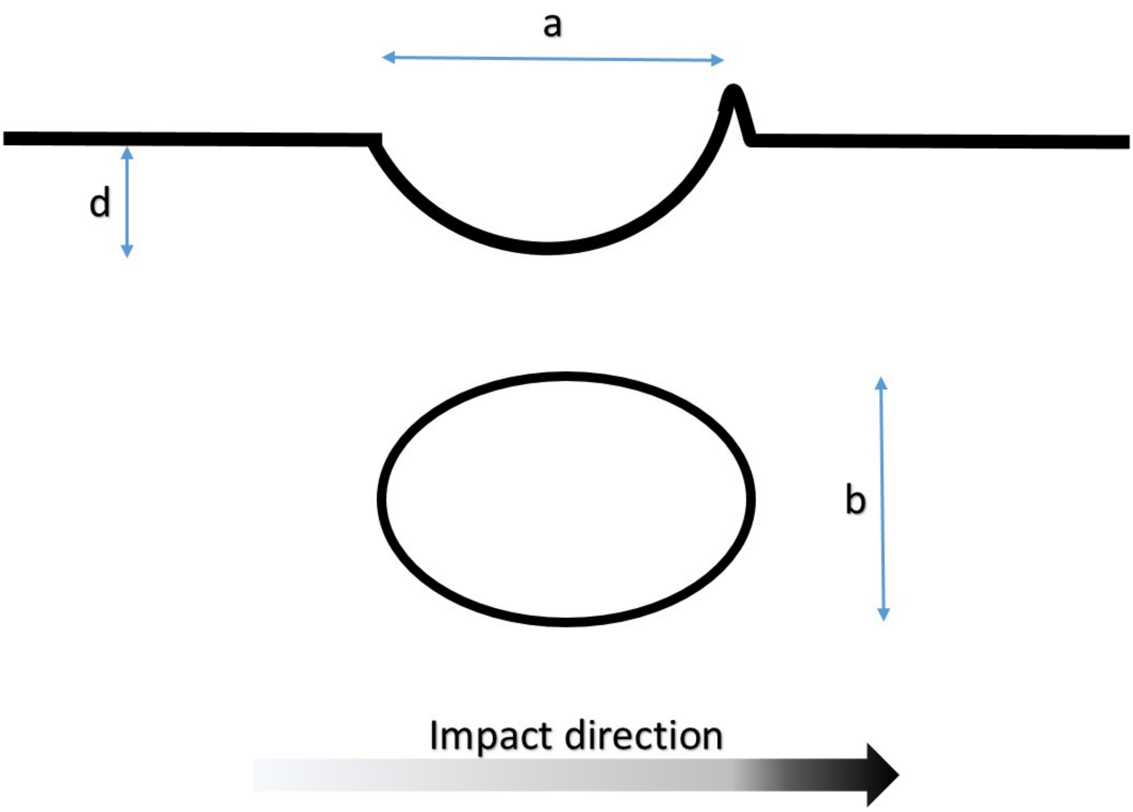

Figure 6.13: Schematic diagram showing the key dimensions used to define the morphology of a compound impact-sliding impact crater

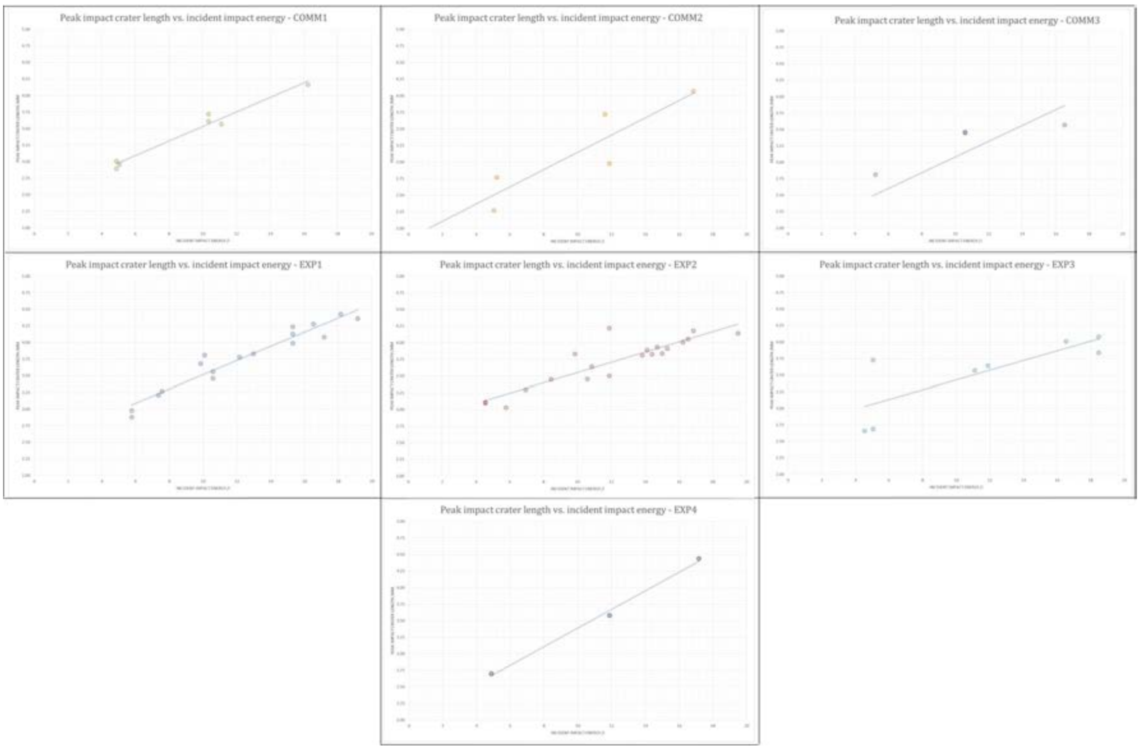

Peak impact crater length vs. incident impact energy - COMM1

Peak impact crater length vs. incident impact energy - COMM2

Peak impact crater length vs. incident impact energy - COMM3

Peak impact crater length vs. incident impact energy - EXP1

Peak impact crater length vs. incident impact energy - EXP2

Peak impact crater length vs. incident impact energy - EXP3

Peak impact crater length vs. incident impact energy - EXP4

Figure 6.14: Average peak length of impact crater for single compound impact sliding tests for the investigated materials

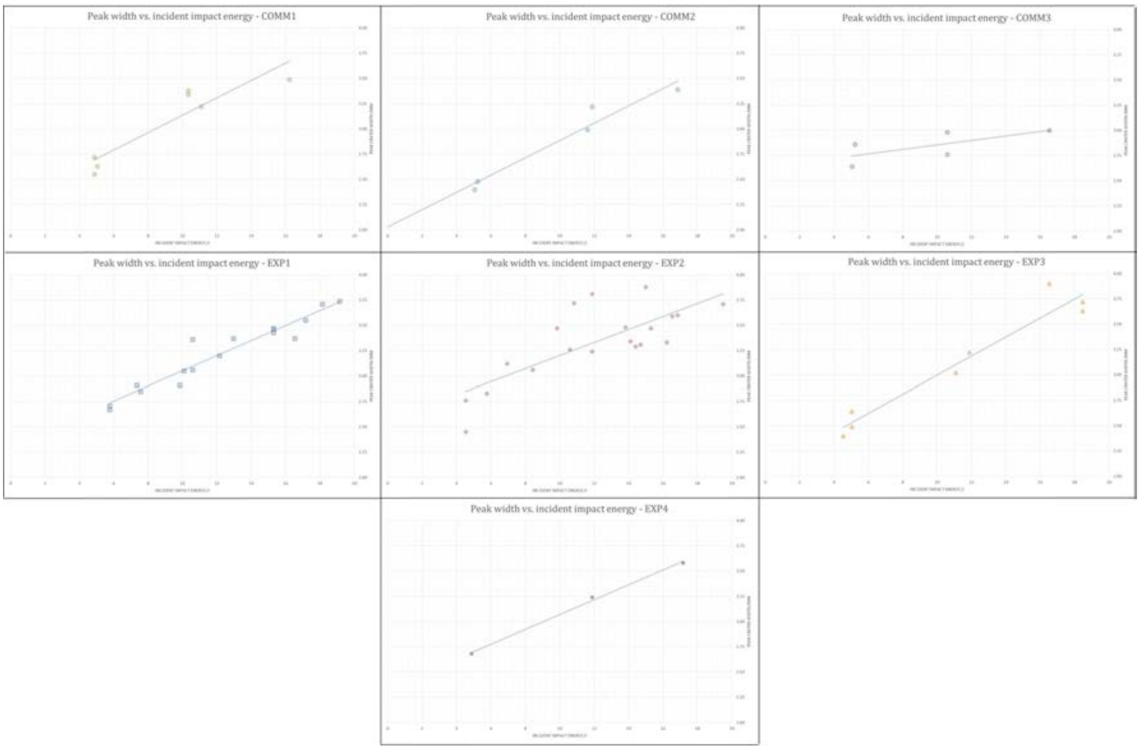

Figure 6.15: Average peak width of impact crater for single compound impact sliding tests for the investigated materials

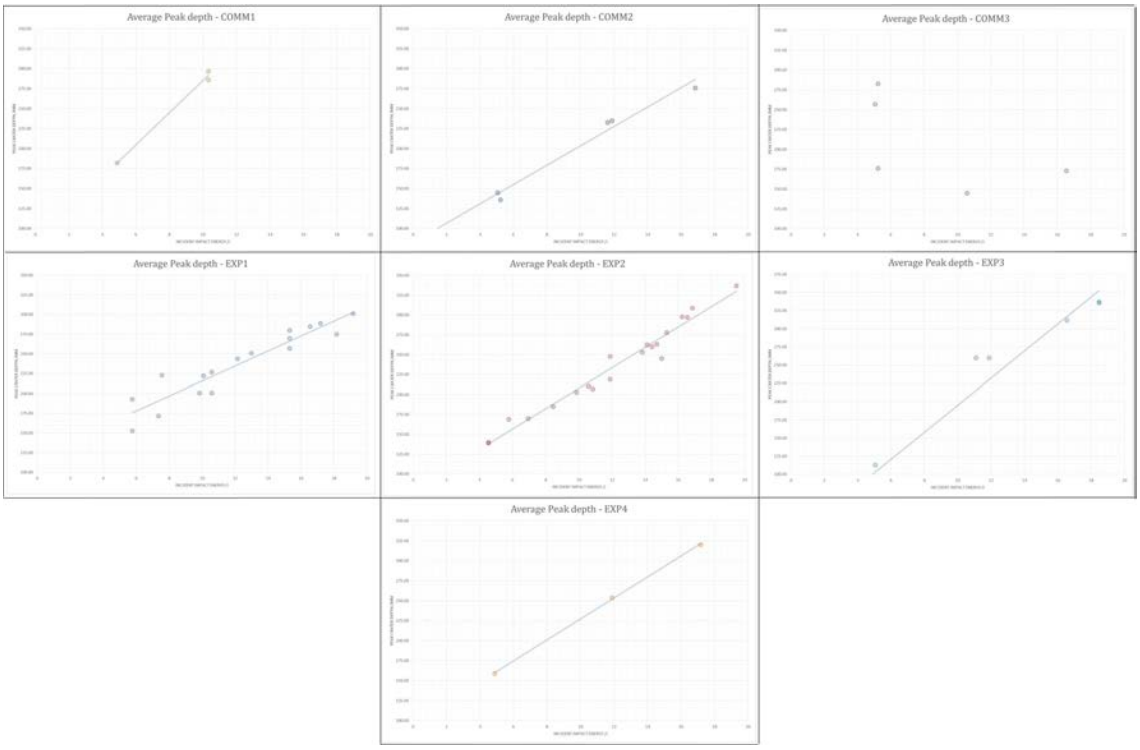

Figure 6.16: Average peak depth of impact crater for single compound impact sliding tests for the investigated materials

Figure 6.17: Approximate top-surface area of impact crater for single compound impact sliding tests for the investigated materials

6.4 Summary

Single body compound sliding impact tests were performed for the coating systems EXP1-4 and COMM1-3. These impact tests were chosen due to the ability to cause high deformation, fracture and wear of the coating(s) and substrate, by a controlled impact test. The primary independent variable was the air pressure to accelerate the projectile. The pressure of the highly pressurised air and its release caused acceleration of the projectile to a reasonably consistent projectile velocity. The tests were performed with equipment that accelerates a steel spherical projectile at the test sample at a known impact angle and reasonably consistent impact velocity. By using Equation 1.3, the impact energy can be calculated to better define the impact.

The impact caused the formation of several failures, as described in Section 6.2, which were observed by microscopy (optical, scanning electron) and optical profilometry. The impact craters were assessed to establish the key failures for each material and impact energy. Thus, it is possible to rank the investigated materials by comparing the minimum impact energy required to cause a failure to observed after impact. This offers a quantative means to rank the coatings for impact and wear protection against single body compound sliding impact.

The impact failures can be seen as being the product of plastic deformation, cohesive fracture or an interfacial spallation. This allows comparison of the failures observed for the same materials with different test methods (e.g. scratch, percussive impact and erosion). With different test methods, it is possible to introduce different loading conditions, which ultimately would change the stress-strain profile through the coating-substrate system. This would allow a comprehensive test matrix to be formed for an experimental laboratory investigation to assess the role of different components of the coating system under different loading conditions. Additionally, by knowing the impact energy to cause a failure to develop, it can be used to validate a computational model.

Chapter 7

Particle erosion

7.1 Introduction

For particulate erosion testing, accelerated particles are propelled towards a test speciment. These tests are inherently complex when considering the particle-to-particle and particle-to-test specimen interactions. Typically, multiple simultaneous impact events may occur over a wide area. Likewise, the particles will have a non-uniform distribution of kinetic energy, mass, rotation and shape. As such, each individual particulate erosion impact event is somewhat unique. Coupled with an evolving target specimen topography due to deformation and wear, the loading conditions are constantly varying.

From an industrial perspective, erosive wear is highly visible. Field tests may be used to qualitively assess different materials to ensure that the best material is chosen for a particular application. However, complexities due to the motion of multiple particles, varying environmental factors (e.g. temperature, humidity, etc.) and a degenerating erosion surface make scientific interpretation difficult. It is for the same reason that VTT is developing multiscale DEM-FEM models to predict erosion performance of key industrial materials, albeit at a high computational cost. For this reason, it is interesting to research whether the erosive wear of a material can be predicted by other simpler techniques. These may include scratch, percussive normal impact and compound sliding impact tests. One advantage of these techniques is that they are simpler to describe with current FEM software and are thus computationally less expensive.

The thick, thermal spray samples (EXP1-3, COMM1-3) were assessed with equipment at TUT. The eroded specimens were assessed quantitively according to mass loss and ranked. Low mass loss corresponds to high erosive wear resistance. The wear mechanisms were assessed using microscopy (optical, SEM) for each investigated material.

7.2 Wear characterisation

7.2.1 Wear quanitification

The materials were subject to erosion testing, with the average particle velocity set at 25, 50 or 80 m/s. The samples were weighed before and after testing, with the difference known as the mass loss. The average mass loss for each investigated material as a function of average particle velocity is given in Figure 7.1.

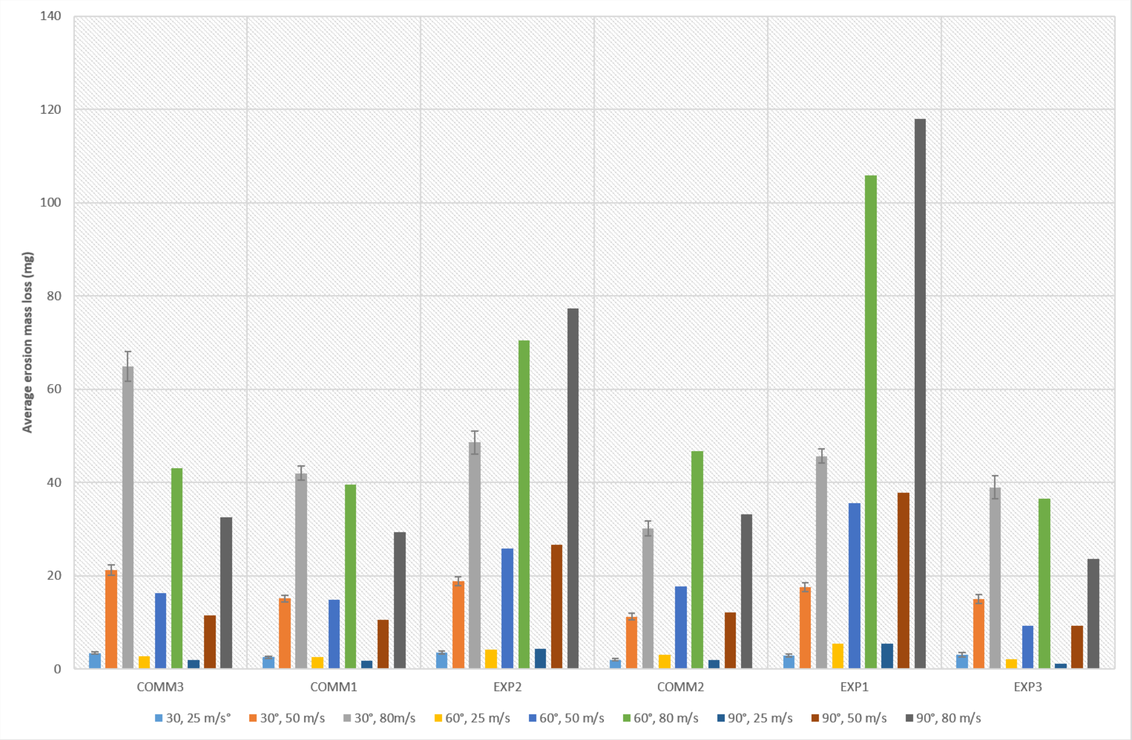

Figure 7.1: Average mass loss for the investigated materials after erosion testing

The mass loss increased significantly with increased average particle velocity, as shown in Figure 7.1. The mass loss at a given angle for all coating systems was relatively low in comparision with the mass losses at higher velocities. It is important to realise that the density of the coatings vary. The mass loss values do not offer a clear indication of the erosive wear resistance of the coating systems.

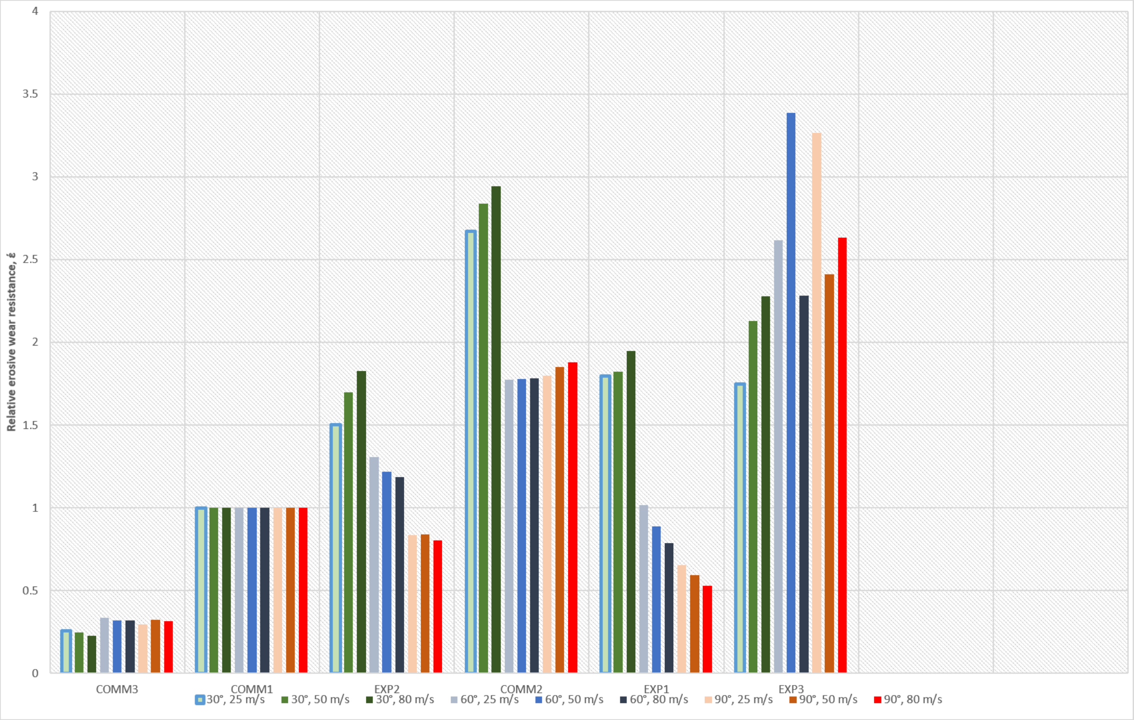

Figure 7.2: Relative erosive wear resistance of thick, thermal spray coatings

In order to determine the relative erosive wear resistance, έ, for a given material, it must be in comparison with a reference material. The mass loss and density for each material must be known. The reference material used for this assessment is COMM1, as it is commonly used in mineral and mining industrial environments. The derivation of the erosive wear resistance is given in Equation 7.1. Note that as the true density is not known for the investigated materials, it is assumed to be the 100%, i.e. free of pores or voids. As such, the density values are literature values for completely dense materials and are considered theoretical. It is also assumed that the densities of EXP1, EXP2, EXP3 and COMM2 are identical as their base composition is the same. Additionally, the mass of impacting particles per unit time and mass, also known as the particle flux rate, is assumed to be constant throughout testing. The results are given in Figure 7.2. If έ is greater than 1, the material has a higher relative erosive wear resistance than COMM1, and vice-versa.

$$\acute{\varepsilon} = \frac{G_e \rho}{G \rho_e} \tag{7.1}$$

Low-angle erosion

With low-angle erosion (30º), the tungsten-carbide based coatings (EXP1-3, COMM2) generally have higher $\dot{\varepsilon}$ values and are therefore more resistant to erosive wear than COMM1 or COMM3. The tungsten-carbide based coatings demonstrate higher hardness and elastic modulus values from both coating top-surface and cross-section orientations, as shown in Table 3.9 and in good agreement with [130]. High macro- hardness and -stiffness allow the coating to withstand scratching of the surface leading to improved erosive wear resistance. This is shown in Figure 7.2, where the coatings are ranked from left to right along the X-axis by increasing top-surface hardness with a general upwards trend.

Likewise, the tungsten-carbide based materials have a higher content of hard phases, around 85 wt% (i.e., primarily Tungsten Carbide with some minor amounts of Tungsten Semicarbide) which reduces the available quantity of relatively soft, ductile binder material (i.e. Cobalt) at the surface which is prone to rapid wear under low angle conditions. The reference material, COMM1, and also COMM3 have lower hard phase contents, around 75%, which results in higher amounts off exposed areas of soft, ductile matrix and reduced macro- hardness and -stiffness. This is discussed further in Section 7.2.2.

Of the tungsten-carbide coatings, the HVAF sprayed coatings (EXP3, COMM2) have the highest $\dot{\varepsilon}$ values. This suggests that the processing method has a significant impact on the erosive performance of thermal spray coatings, for a given base composition. This could be due to the HVAF coatings being significantly harder than the HVOF sprayed coatings in the top-surface and cross-sectional orientations.

High-angle erosion

With high-angle erosion (60º, 90º), the tungsten-carbide based coatings generally exhibit better performance with respect to the relative erosive wear resistance, $\dot{\varepsilon}$, than COMM3 or the reference material COMM1. However, there are exceptions to this rule for materials EXP1 and EXP2 at an impact angle of 90º for all impact velocities which were tested. The best performing coatings were COMM2 and EXP3, with $\dot{\varepsilon}$ values over 1.7 in comparison to a $\dot{\varepsilon}$ of 1 for COMM1.

The invesetigated materials EXP1 and EXP2 were formed by High Velocity Oxy Fuel processes (HVOF) whilst COMM2 and EXP3 were formed by High Velocity Air Fuel processes. These coatings have similar top-surface hardness and elastic modulus, however their cross-sectional hardness and elastic modulus values are significantly different. In terms of hardness, EXP1's is lower by 1.3 GPa. In terms of the elastic modulus, EXP1 is lower by 59 GPa. The primary difference between the two coatings is that the high temperature spray method used for the production of EXP1 creates dissolution volumes in the matrix binder phase. These volumes form around carbides, leading to the formation of brittle phases around the carbide. This weakens the material and leaves it prone to failure through fracture of the carbides and other brittle regions.

[write more]

7.2.2 Assessment of the wear mechanisms

The investigated materials can be generally described as composites of two volumes; a soft and ductile metallic binder, and a hard, brittle carbide fraction. If one considers that the two volumes are independantly homogeneous, the analysis is simplified. In reality, due to uneven thermal effects during the spray process, this is often incorrect for higher temperature processes (e.g. HVOF, plasma spray).

The reference material, COMM1, features a binder content of roughly 25% by weight. Under low angle erosion testing, microcutting of the eroded surface was observed, as shown in Figure 7.3. Microcutting is often a dominant failure mode for metal-matrix composites with a metal content greater than 50% [130](other refs). For microcutting to be observed, the eroding particles (e.g. quartz) must be harder than the target eroded material (i.e. metal binder). Microcutting can be reduced by increasing the hardness of the metal binder phase. This can be achieved by solid solution strengthening, fine carbide or oxide dispersions or by effecting compressive residual stresses during the processing stage. Alternatively, the hard phase content (i.e. carbides) can be increased with respect to the metal binder content. As the erosive particle impact velocity increases, the severity of microcutting increases too.

When the eroded surface of COMM1 is observed using backscattered scanning electron imaging, the carbides are most easily seen. As shown in Figure 7.4, the carbides also show some fractures. The fractures are not extensive and as such carbide fracture is not considered to be the primary wear mechanism for COMM1 under low angle conditions. Regardless, it shows that under the test conditions that the fracture toughness of the carbide volumes of COMM1 is insufficient to provide total erosive wear resistance under low angle erosion.

It is shown in [131] that carbide volumes of WC-Co cermets that the soft Cobalt matrix wears preferentially during erosion. The carbide volumes are durable, although th7.3ey may fail due to fracture or fatigue. Additionally, the carbides may be dislodged

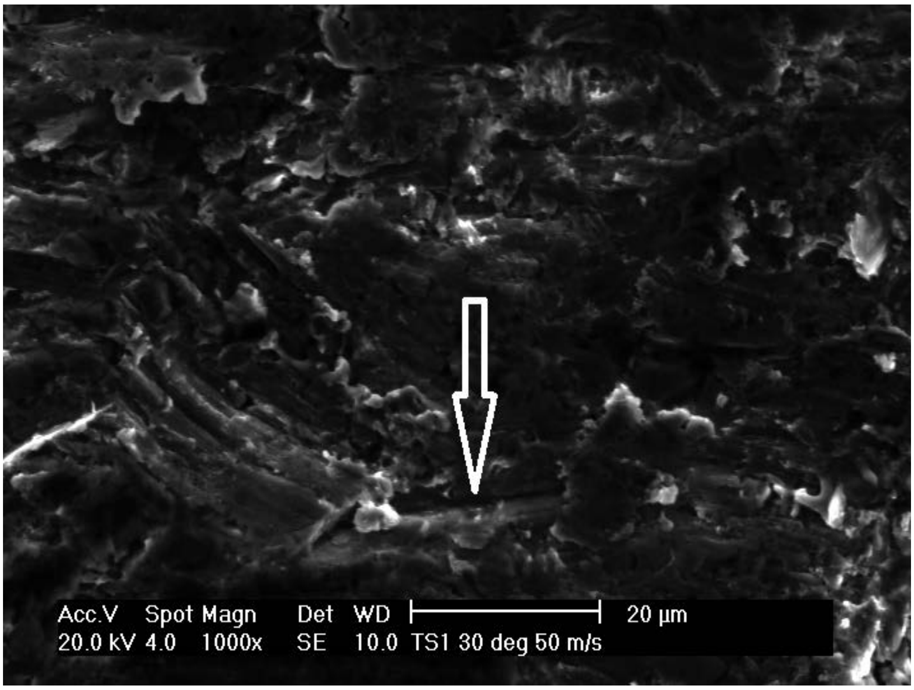

Figure 7.3: A SEM image (secondary electron) of the eroded surface of COMM1 sample after erosion testing at 30º and 50 m/s. An example of microcutting is shown by the white arrow

due to the removal of binder close to individual carbides. As each individual impact event is finely localised and rarely loading significant volumes of both phases, the carbides are not seen to offer significant protection to the matrix volume. This is dissimilar to earlier high load, single asperity tests (scratch, impact) where the carbides are believed to reinforce the deformation-prone matrix volume [60]. As such, erosion testing of the investigated materials offers insight towards the role of the matrix during tribological investigation. For a given raw material feedstock (wire or powder), the nature of the matrix can vary depending upon the thermal spray process parameters employed.

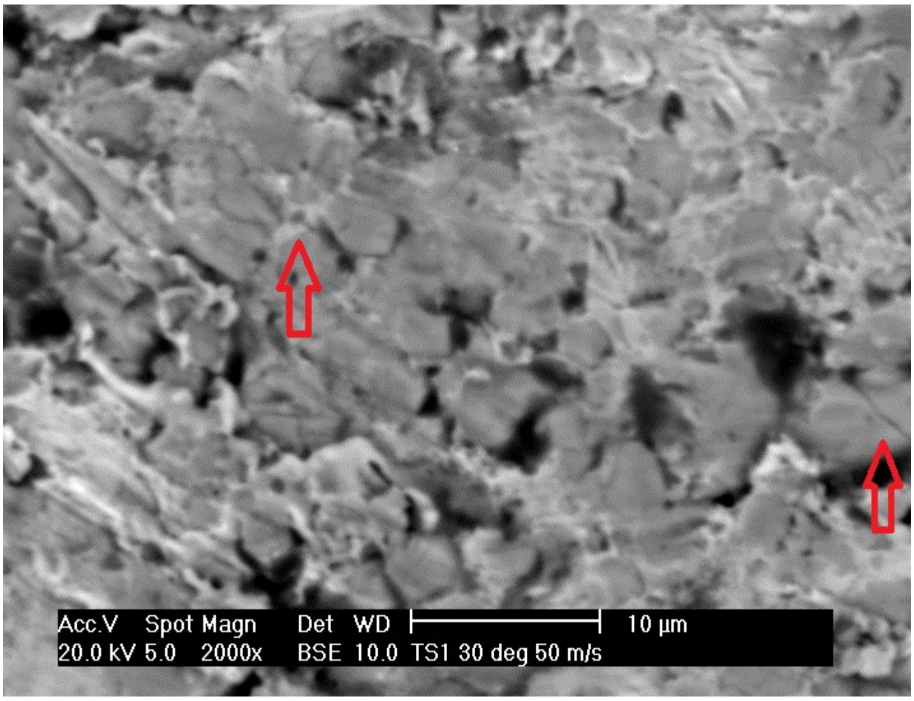

Figure 7.4: A SEM image (backscattered electron) of the eroded surface of COMM1 sample after erosion testing at 30º and 50 m/s. An example of carbide fracture is shown by the white arrow

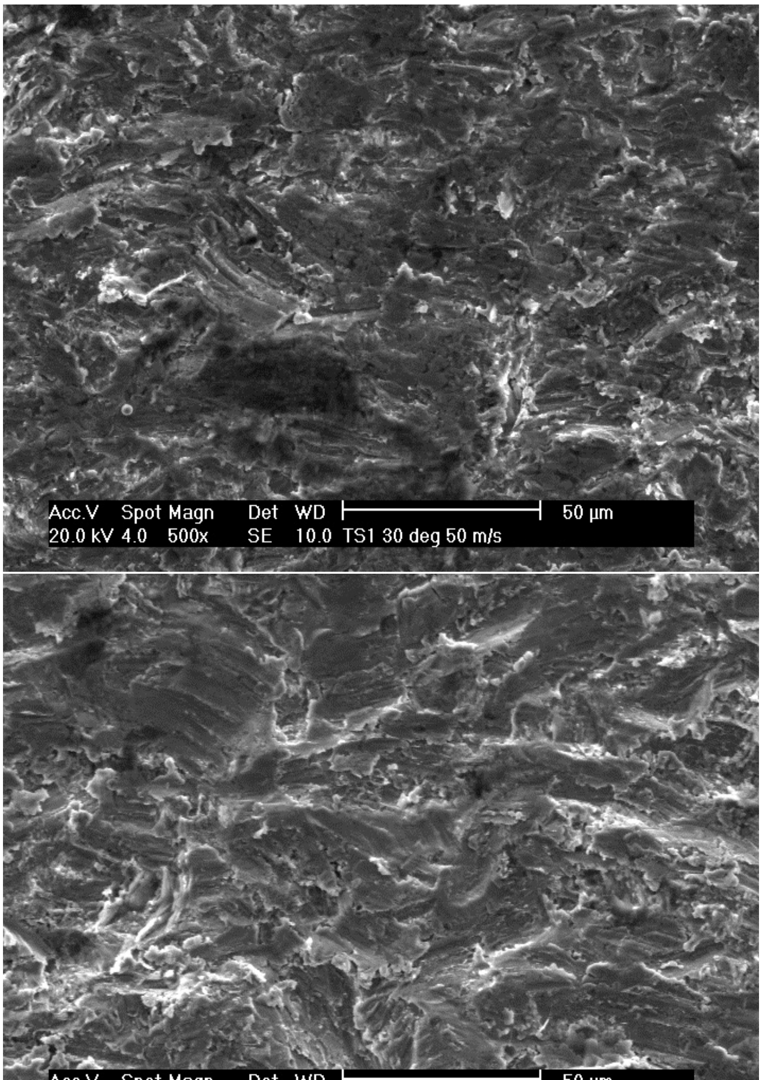

Numerous scars are seen on the eroded surfaces in Figure 7.5. These scars form by high plastic deformation of the matrix under a glancing particulate impact event. For all assessed investigated coatings, the primary wear mechanism by erosive cutting. In most cases, the hard erosive particles did not embed into the eroded surface and were deflected after the impact. This suggests that the matrix volumes were not sufficiently ductile for to allow particulate entrapment by plastic deformation, yet were able to deform plastically.

The secondary coatings failures were observed to be fracture of large carbides. The fractures were not seen to be critical; the carbide remained embedded in the matrix. However, the matrix volume is clearly reduced around the carbide. This effect is clearly demonstrated for COMM1 and COMM3 in Figure 7.6.

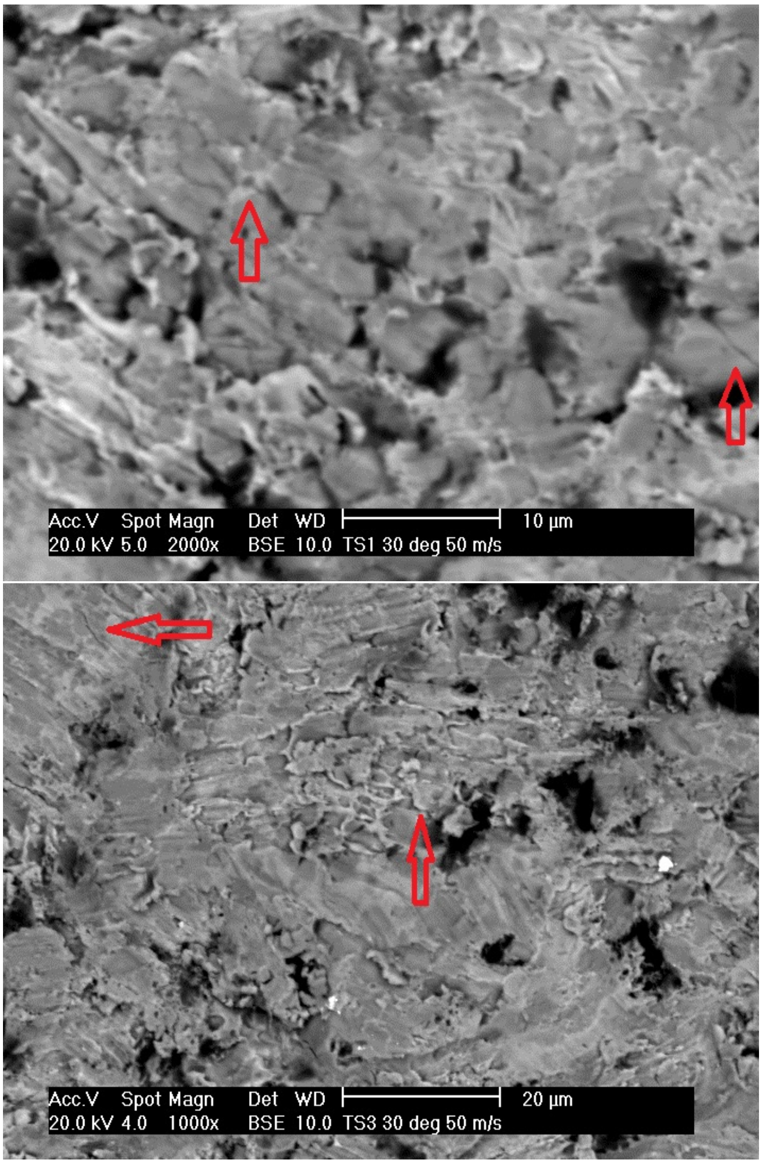

Figure 7.6: Carbide fracture and local matrix volume wear for COMM1 (top) and COMM3 (bottom), after erosion assessment at 30° and 50 m/s

7.3 Summary of particle erosion wear assessment

The thick, thermal spray coatings were subject to a series of erosion tests. The erosive media was accelerated by a centrifugal accelerating device as show in Figure 2.6. The test matrix investigated the role of impact velocity and impact angle for the test materials EXP1, EXP2, EXP3, COMM1, COMM2 and COMM3. The exception was EXP4, where the limited amount of samples did not permit any erosion tests to be performed.

The materials were assessed according to their wear by mass loss per unit mass of erosive media and relative erosion wear resistance for a range of average particle velocities and impact angles. Mass loss was measured with a balance, finding the difference of sample mass before and after erosion testing. In order to compare the wear performance of the investigated coatings, the coatings were assumed to have an apparent density of 100%, i.e. without pores and that the samples were ideally smooth before the commencement of erosion testing.

The Tungsten Carbide based coatings generally demonstrated better erosion resistance compared to the Chromium Carbide (COMM1) and Molybdenum Boride (COMM3) coatings. It is suspected that differences in hardness, modulus, ductile binder content and the morphology and content of hard phases are significant.

Additionally, the harder Tungsten Carbide-based coatings performed with greater distinction under low angle erosion testing (30º). The HVOF sprayed Tungsten Carbide-based materials, EXP1 and EXP2, offered similar relative erosion wear resistance at 30º and 60º for all particle velocities tested. At 90º, the coatings offered a relative erosion wear resistance less than that of COMM1 for all investigated particle velocities. This was not observed for either of the HVAF Tungsten Carbide-based coatings, COMM2 and EXP3. The base composition of EXP1, EXP2, COMM2 and EXP3 is defined by the raw material (powder as described in Table 3.3). Thus, it is suggested that HVAF processing provides greater erosion resistance than for HVOF processing, for a given base composition. It is likely that this is due to their high top surface hardnesses, restraining plastic deformation on the investigated surface. The softer HVAF coatings, COMM1 and COMM3 performed poorly with respect to all of the Tungsten Carbide based coatings; likely due to high ductility enabling cutting and ploughing of the softer matrix volume leading to enhanced wear.

Chapter 8

Discussion

8.1 Introduction

The investigated materials were investigated with numerous methods. A flowchart which shows the investigation process is given in Figure 1.7.These included characterisation to determine their material properties as shown in Chapter 3 with commonly used methods. The materials were characterised to help define their microstructure and mechanical properties which will determine their behaviour under the test conditions.

Then, the investigated materials were assessed according to their basic tribological and impact performance for simple loaded contacts, as presented in Chapters 4, 5 and 6. These methods are relatively simple when compared to the real, industrial problems faced currently. They are able to assess different characteristics of the investigated materials under certain criteria (sliding, normal impact and compound sliding impact).

Finally, the investigated materials were assessed by erosion testing as shown in Chapter 7. This method is complex when describing movement of the erosive particles and relating that to the degredation of the test surface. It is fairly well defined compared to an industrial environment (e.g. rock mine, desert sandstorm) however more complex than a laboratory impact test.

In this section, the results and findings from Chapters 2, 4, 5, 6and 7 are compared to see how they can be used to understand real-world impact and erosion behaviour of thick, composite coatings. It is hoped that a combination of simple laboratory scale investigations can be used to lead to increased understanding of complex, industrial wear related to impact and erosion conditions.

8.2 The effects of hardness, elastic modulus and fracture toughness on the scratch response

The individual thermal spray process and parameters used to spray the coatings influence the microstructure of the coating which partially influences the performance of the coating. The scratch performance of the tungsten-based coatings (EXP1, EXP2, EXP3 and COM2) was compared against results obtained to describe their mechanical properties and fracture behaviour by indentation methods, in Sections 8.2.1, 8.2.2 and 8.2.3.

8.2.1 Hardness

The hardness of a material under a static load is defined by the load applied and the contact area. It is the resistance that a material exhibits to plastic deformation. Increased hardness has been shown to improve sliding wear resistance for plastically deforming, asperity-asperity contacts [26].

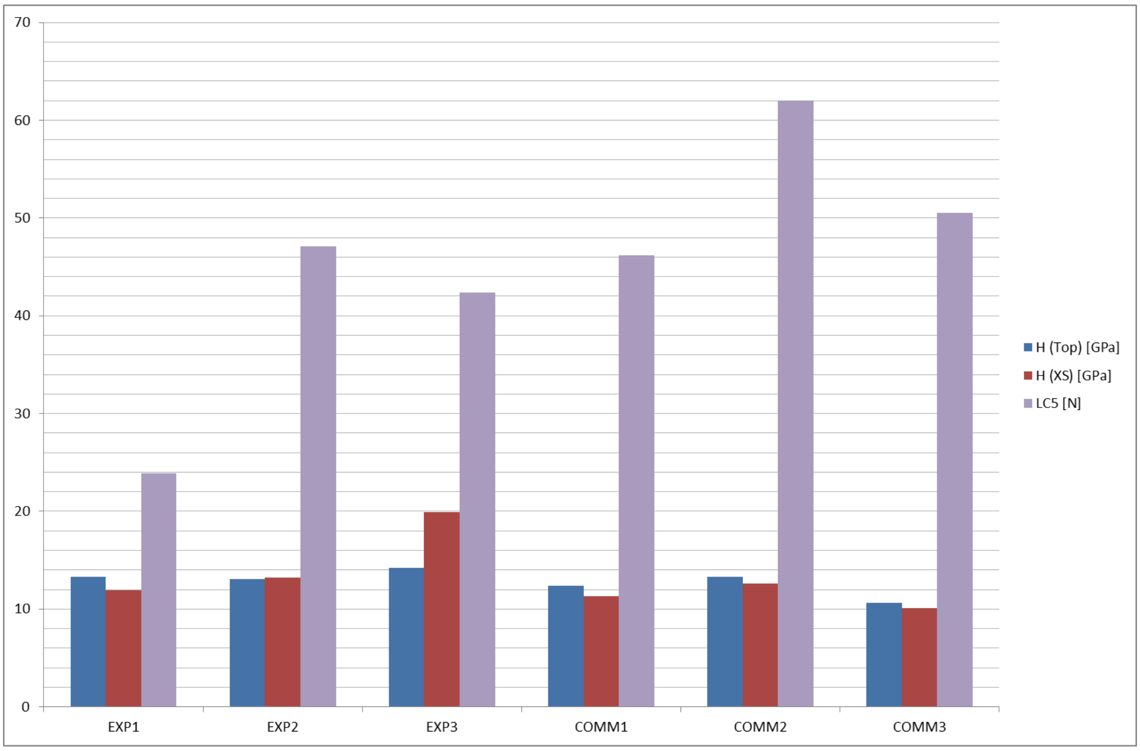

Figure 8.1: Plot of hardness vs. LC5 for the investigated thick, thermal spray coatings

A scratch test can be described as an interasperity contact. Under ideal conditions, the indenter is perfectly formed and smooth. In the case of the Rockwell C diamond indenters used, we assume that the spherical tip is perfectly round, i.e. unworn. Likewise if the rougness of the polish surface is below a certain criteria related to the indenter size, there could be interasperity contact. However, the thermal spray coatings are not perfectly smooth and uniform across the polished surface. This is due to carbide and splat pullout, aswell as fine grooves and scratches arising from the polishing process and even minor cracking. Thus, the relationship between hardness and scratch performance is unclear for the investigated materials.

The hardness of the investigated materials was plotted against the critical scratch failure load for delamination (Lc5). The hardness is plotted against LC5 for both top-surface and cross-sectional orientations in Figure 8.1.

8.2.2 Elastic Modulus

The elastic modulus of a material defines the resistance to elastic deformation.

The Indentation Elastic modulus is plotted against LC5 for both top-surface and cross-sectional orientations in Figure 8.2.

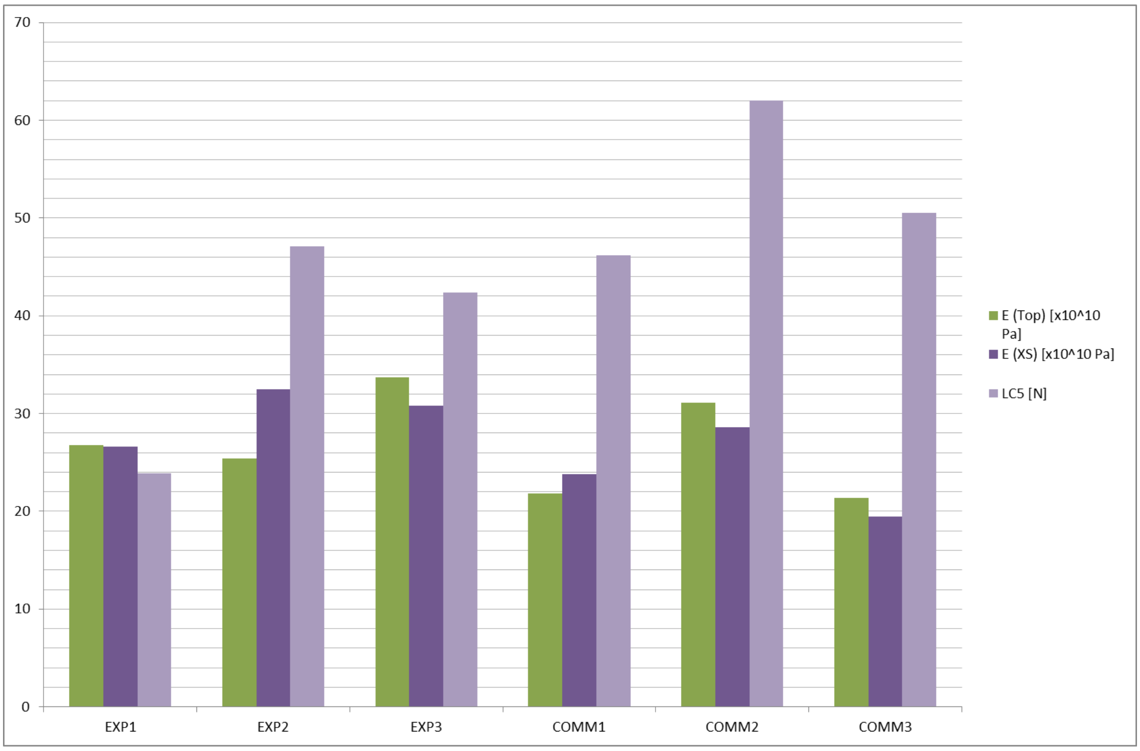

Figure 8.2: Plot of Indentation Elastic Modulus vs. LC5 for the investigated thick, thermal spray coatings

Figure 8.4: Plots showing percussive normal impact crater volume vs. indentation modulus, indentation hardness (macro) and cross-sectional indentation fracture toughness

8.2.3 Fracture toughness

Figure 8.3: Graphs showing the relationship between fracture toughness and selected critical scratch failure loads for the investigated thick, thermals spray coatings

8.3 Failure and wear vs. material properties for percussive normal impact

8.4 Erosion vs. scratch

The erosion results are compared with those obtained during scratch test assessment, as described earlier in Chapter 4.

[Finish scratch chapter first]

8.5 Erosion vs. impact

The erosion results are compared against those for percussive normal impact (Chapter 5) and single compound sliding-impact (Chapter 6).

8.5.1 Erosion vs. percussive normal impact

[Write up percussive impact chapter first]

8.5.2 Erosion vs. single, particulate impact

[Write up single impact chapter first]

Chapter 9

Conclusions

Industrial materials and components which are used in mining and minerals handling are subject to significant damage due to harsh operating conditions. It is expected that components which are exposed to a mining site are at risk of damage by numerous means, including impact loading, erosion, abrasion and adhesion. These wear modes can be investigated individually using current laboratory methods. The benefit is that the performance of each material system can be investigated in a controlled manner with reasonable control over the test conditions. However, laboratory-scale assessment may not correlate with tests which have been performed in the field of action, i.e. a mine. Therefore, it is important to consider the relevance of a single laboratory test against the real application. It is also important to understand the reach and limitations of a particular test method.

A test framework based on a range of laboratory assessments was developed to improve the design of impact resistant, thick coatings. The nature of an impact event was described by the impact force or energy, number of impact cycles and impact angle.

For each laboratory assessment, the test site was investigated to determine the nature of the developing or developed failures. The onset of failure was measured against the critical controllable variable for the assessment; applied force, number of loading cycles or impact energy. For thick thermal spray coatings, failure mechanisms including tensile cracking, cohesive spallation and interfacial spallation were commonly observed for most laboratory tests and materials.

Scratch tests were performed to assess the response of the investigated coating systems under a sliding contact. A sliding contact develops significant tensile and compressional shear stresses. These are features which are seen for impact test methods, yet are difficult to isolate due to the rapid nature of an impact contact. A methodolgy was developed based on currently accepted methods, to accomodate differing failure modes observed for both thick and thin hard coatings. Coatings manufactured with HVAF methods dominated, showing higher resistance to fracture and cohesive strength. Generally, these qualities can also be observed for the impact tests. This suggests that a coating that performs well under scratch testing may also have some of the qualities necessary for impact wear resistance.

For percussive normal impact contacts, the topsurface hardness correlated with impact resistance. The hard HVAF Tungsten Carbide coatings showed reduced plastic deformation and wear at high and low loads in contrast to the softer HVOF Tungsten Carbide coatings. The form of the impact crater evolved with the number of impact cycles; starting with plastic deformation, then fracture of the coating and ultimately wear by fatigue, microsliding or sudden fracture. This allowed the coatings to be ranked qualitively by marking the failures developed and their severeity against the number of impact cycles. Additionally, quantative assessment was made by measuring the crater morphology (depth, area, volume) against the impact cycles, to describe the impact resistance.

[1pp on compound impact results]

Generally speaking, the thermal spray Tungsten Carbide-based coatings manufactured by High Velocity Air-Fuel (HVAF) processes performed with greatest distinction. High fracture toughness and hardness were promoted by high particle spray velocity and a relatively cool spray temperature profile. The Tungsten Carbide coatings manufactured by High Velocity Oxy-Fuel (HVOF) processes utilised lower particle spray velocities and higher spray temperature profiles. The highest spray temperature profile process (DJ-H) developed significant volumes of complex diffusion volumes, which are likely to be deleterious to tribological and impact resistance due to increased brittleness.

[1pp on role of the material choice]

When looking at the Processing-Structure-Property-Performance (PSPP) methodology [4], this work concentrated on the relationship between material properties and performance under laboratory conditions. A number of different methods were used to investigate coatings with different material and mechanical properties. Some methods were modified to enable the assessment of thick, thermal spray coatings. In the future, additional research could be performed to optimise coating microstructures by improving the thermal spray conditions, which will lead to an increased resistance to deformation and wear by impact and sliding contacts. The research suggested that HVAF spray methods deliver highly wear- and deformation-resistant coatings, which should be investigated further.

References

[1] BS EN 1071-3:2005 Advanced technical ceramics - Methods of test for ceramic coatings, 2005.

[2] A. Ghabchi, S. Sampath, K. Holmberg, and T. Varis. Damage mechanisms and cracking behavior of thermal sprayed WCCoCr coating under scratch testing. *Wear*, 313(1-2):97–105, May 2014.

[3] P.A. Engel. *Impact wear of materials.* Elsevier, Amsterdam, The Netherlands, 1976.

[4] G.B Olson. Designing a new material world. *Science*, 288(5468):993–998, 2000.

[5] Vtt propertune. Website, September 2015.

[6] Home page. Website, September 2015.

[7] H.P. Jost. Lubrication (tribology) - education and research. a report on the present position and industry needs (jost report). Technical report, Department of Education and Science, HM Stationary Office, London, 1966.

[8] H.P. Jost and J. Schofield. Energy savings through tribology: A techno-economic study. *Proceedings - Institute of Mechanical Engineers*, 197(16):151–173, 1981.

[9] G.W. Stachowiak and A.W. Batchelor. *Engineering Tribology.* Elsevier, Amsterdam, The Netherlands, 3rd edition edition, 2005. 801 pp.

[10] D. Tabor. *The Hardness of Metals.* Oxford Classic Texts in the Physical Sciences. Oxford University Press, Great Clarendon Street, Oxford, United Kingdom, 1951. 175 pp.

[11] D. Platz, E.A. Tholén, C. Hutter, A.C. von Bieren, and D.B. Haviland. Phase imaging with intermodulation atomic force microscopy. *Ultramicroscopy*, 110:573–577, 2010.

[12] S. Siegel. A review of supersonic methods for measuring elastic and dissipative properties of solids. *The Journal of the Acoustical Society of America*, 16(1):26–30, 1944.

[13] W.C. Oliver and G.M. Pharr. An improved technique for determining hardness and elastic modulus using load and displacement sensing indentation experiments. *Journal of materials research*, 7(06):1564–1583, 1992.

[14] W.C. Oliver and G.M. Pharr. Measurement of hardness and elastic modulus by instrumented indentation: Advances in understanding and refinements to methodology. *Journal of Materials Research*, 19(1):3–20, 2004.

[15] K Kato. Classification of wear mechanisms / models. *Proceedings of the Institution of Mechanical Engineers, Part J: Journal of Engineering Tribology*, 216(October 2001):349–355, January 2002.

[16] S.C. Lim and M.F. Ashby. Wear mechanism maps. *Acta Metallurgica*, 35(1):1–24, 1987.

[17] D.H. Buckley. *Surface Effects in Adhesion, Friction, Wear and Lubrications.* Elsevier, 1981.

[18] I.M. Hutchings. Abrasive and erosive wear tests for thin coatings: a unified approach. *Tribology International*, 31(1-3):5–15, January 1998.

[19] M. Lindroos, V.-T. Kuokkala, A. Lehtovaara, and P. Kivikytö-Reponen. Effects of Strain and Strain Rate on the Abrasive Wear Behavior of High Manganese Austenitic Steel. *Key Engineering Materials*, 527:211–216, November 2012.

[20] Standard test method for scratch hardness of materials using a diamond stylus. In *ASTM G171-03*, pages 1–7.

[21] Standard Test Method for Measuring Abrasion Using the Dry Sand Rubber Wheel Apparatus - ASTM G65, 2010.

[22] J. Terva, T. Teeri, V.-T. Kuokkala, P. Siitonen, and J. Liimatainen. Abrasive wear of steel against gravel with different rock steel combinations. *Wear*, 267(11):1821–1831, October 2009.

[23] Standard test method for wear testing with a pin-on-disk apparatus, astm g99 - 05, 2010.

[24] S. Ilo, A. Tomala, and E. Badisch. Oxidative wear kinetics in unlubricated steel sliding contact. *Tribology International*, 44(10):1208–1215, September 2011.

[25] R. Holm. *Electric Contacts*. Hugo Gebers Forlag, Stockholm, Sweden, 1940.

[26] J. F. Archard. Contact and Rubbing of Flat Surfaces. *Journal of Applied Physics*, 24(8):981, 1953.

[27] E. Rabinowicz. *Friction and Wear of Materials*. Wiley, New York, USA, 1965.

[28] R. Lewis. A modelling technique for predicting compound impact wear. *Wear*, 262:1516–1521, 2007.

[29] R. Waudby, P. Andersson, and K. Holmberg. Low-speed sliding tests with nodular cast iron in contact with steel wire and a diamond tip. *Tribology International*, 65:171–176, September 2013.

[30] H.S. Gehman, J. Barry, D. Deal, J. Hallock, K. Hess, S. Hubbard, J. Logsdon, D. Osherd, S. Ride, R. Terault, S. Turcotte, and W. Steven. Columbia Accident Investigation. Technical Report August, 2003.

[31] J. Chen, B.d Beake, R.G. Wellman, J.R. Nicholls, and H. Dong. An investigation into the correlation between nano-impact resistance and erosion performance of EB-PVD thermal barrier coatings on thermal ageing. *Surface and Coatings Technology*, 206(23):4992–4998, July 2012.

[32] D.A. Kring. Air blast produced by the meteor crater impact event and a reconstruction of the affected environment. *Mathematics and Planetary Science*, 32:517–530, 1997.

[33] A. Sundström, J. Rendón, and M. Olsson. Wear behaviour of some low alloyed steels under combined impact/abrasion contact conditions. *Wear*, 250(1-12):744–754, October 2001.

[34] K.-D. Bouzakis, N. Vidakis, T. Leyendecker, G. Erkens, and R. Wenke. Determination of the fatigue properties of multilayer PVD coatings on various substrates, based on the impact test and its FEM simulation. *Thin Solid Films*, 308-309:315–322, October 1997.

[35] G. Cassar, S. Banfield, J.C. Avelar-Batista Wilson, J. Housden, A. Matthews, and A. Leyland. Impact wear resistance of plasma diffusion treated and duplex treated/PVD coated Ti-6Al-4V alloy. 206:2645–2654, 2012.

[36] O. Knotek, B. Bosserhoff, A. Schrey, T. Leyendecker, O. Lemmer, and S. Esser. A new technique for testing the impact load of thin films: the coating impact test. *Surface and Coatings Technology*, 54-55:102–107, 1992.

[37] R. Bantle and Allan Matthews. Investigation into the impact wear behaviour of ceramic coatings. *Surface and Coatings Technology*, 74-75:857–868, 1995.

[38] J.C.A. Batista, C. Godoy, and A. Matthews. Impact testing of duplex and non-duplex TiAlN and CrN PVD coatings. *Surface and Coatings Technology*, 163-164:353–361, January 2003.

[39] M.F.B Abdollah, Y. Yamaguchi, T. Akao, N. Inayoshi, N. Miyamoto, T. Tokoroyama, and N. Umehara. Deformation wear transition map of DLC coating under cyclic impact loading. *Wear*, 274-275:435–441, January 2012.

[40] J.L. Mo, M.H. Zhu, a. Leyland, and A. Matthews. Impact wear and abrasion resistance of CrN, AlCrN and AlTiN PVD coatings. *Surface and Coatings Technology*, 215:170–177, January 2013.

[41] T. Slatter, R. Lewis, and A.H. Jones. The influence of induction hardening on the impact wear resistance of compacted graphite iron (CGI). *Wear*, 270(3-4):302–311, January 2011.

[42] T. Slatter, R. Lewis, and A.H. Jones. The influence of cryogenic processing on wear on the impact wear resistance of low carbon steel and lamellar graphite cast iron. *Wear*, 271(9-10):1481–1489, July 2011.

[43] I.M. Hutchings. A simple small-bore laboratory gas-gun. *Journal of Physics E: Scientific Instruments*, 8:84–86, 1975.

[44] G.A. Sargent and R.M. Vadjikar. Impact of aluminum by single spherical particles as a function of temperature. *Wear*, 96:143–151, 1984.

[45] M. Apostol, V.-T. Kuokkala, A. Laukkanen, and K. Waudby, R. andHolmberg. High velocity particle impactor - modelling and experimental verification of impact wear tests. In *Proceedings of the World Tribology Congress*, Torino, Italy, September 2013.

[46] R. Waudby, T. Varis, T. Suhonen, K. Holmberg, M. Apostol, M. Lindroos, and V.-T. Kuokkala. High velocity impact testing of thermal spray hard carbide coatings on steel substrates. In *World Tribology Congress*, Torino, Italy, 2013.

[47] F.B. Bowden and D. Tabor. *The Friction and Lubrication of Solids*, volume I and II. Oxford University Press, 1964.

[48] E.F. Finken. *Journal of Lubrication Technology*, 95:393–394, 1973.

[49] Peter A Engel and Zheming Zhao. Impact of Delrin disc: lubricated and dry contacts. *Wear*, 193:114–125, 1995.

[50] K Holmberg, A Laukkanen, A Ghabchi, M Rombouts, E Turunen, R Waudby, T Suhonen, K Valtonen, and E Sarlin. Tribology International Computational modelling based wear resistance analysis of thick composite coatings. 72:13–30, 2014.

[51] K. Holmberg, A. Laukkanen, E. Turunen, and T. Laitinen. Wear resistance optimisation of composite coatings by computational microstructural modelling. *Surface and Coatings Technology*, 247:1–13, May 2014.

[52] K. Holmberg, A. Laukkanen, A. Ghabchi, M. Rombouts, E. Turunen, R. Waudby, T. Suhonen, K. Valtonen, and E. Sarlin. Computational modelling based wear resistance analysis of thick composite coatings. *Tribology International*, 72:13–30, April 2014.

[53] R.E. Jones. *Bondcoat developments for thermal barrier coatings.* Doctoral thesis, Sheffield Hallam University, 1999.

[54] M. Oksa. *Nickel and iron based HVOF thermal spray coatings for high temperature corrosion protection in biomass fired power plant boilers.* Doctoral thesis, Aalto University, 2015.

[55] J.A. Picas, A. Forn, and G. Matthäus. HVOF coatings as an alternative to hard chrome for pistons and valves. *Wear*, 261(5-6):477–484, September 2006.

[56] R. J K Wood. Tribology of thermal sprayed WC-Co coatings. *International Journal of Refractory Metals and Hard Materials*, 28(1):82–94, 2010.

[57] S. Siegmann and C. Albert. 100 years of thermal spray: About the inventor max ulrich schoop. *Surf. Coat. Technology*, 220:3–13, 2013.

[58] P. Vuoristo. Thermal Spray Coating Processes. In D Cameron, editor, *Comprehensive Materials Processing*, volume 4, chapter 4.10, pages 229–276. Elsevier Ltd, 2014.

[59] G. Mauer, R. Vassen, and D. Stover. Plasma and Particle Temperature Measurements in Thermal Spray: Approaches and Applications. *Journal of Thermal Spray Technology*, 20(3):391–406, November 2010.

[60] A. Ghabchi. *Wear Resistant Carbide based Thermal Sprayed Coatings. Process , Properties , Mechanical Degradation and Wear.* PhD thesis, Stony Brook University, 2011.

[61] J. Karthikeyan. Cold spray technology. *Advanced Materials and Processes*, 163(3):33–35, 2005.

[62] S. V. Klinkov, V. F. Kosarev, A. A. Sova, and I. Smurov. Deposition of multicomponent coatings by Cold Spray. *Surface and Coatings Technology*, 202(24):5858–5862, 2008.

[63] T. Stoltenhoff, H. Kreye, and H.J. Richter. An analysis of the cold spray process and its coatings. *Journal of Thermal Spray Technology*, 11(4):pp. 542–550, 2002.

[64] Y. Xu and I. M. Hutchings. Cold spray deposition of thermoplastic powder. *Surface and Coatings Technology*, 201(6):3044–3050, 2006.

[65] H.J Kim, C.H. Lee, and S.Y. Hwang. Fabrication of WC-Co coatings by cold spray deposition. *Surface and Coatings Technology*, 191(2-3):335–340, 2005.

[66] T. Suhonen, T. Varis, E. Turunen, X. Liu, Y. Ge, O. Söderberg, and S.-P. Hannula. The effect of microstructure on mechanical properties of HVOF sprayed WC-CoCr composite coatings. *Tribologia*, 28(1-2):14–28, 2009.

[67] M. Oksa, E. Turunen, T. Suhonen, T. Varis, and S.-P. Hannula. Optimization and characterization of high velocity oxy-fuel sprayed coatings: Techniques, materials, and applications. *Coatings*, 1:17–52, 2011.

[68] T. Suhonen, T. Varis, S. Dosta, M. Torrell, and J.M. Guilemany. Residual stress development in cold sprayed Al, Cu and Ti coatings. *Acta Materialia*, 61(17):6329–6337, October 2013.

[69] A. Holmberg, K.and Matthews. *Coatings Tribology: Properties, Mechanisms, Techniques and Applications in Surface Engineering*, volume 56 of *Tribology and Interface, Engineering Series*. Elsevier, 1994.

[70] M. Leskelä and M. Ritala. Atomic layer deposition (ALD): From precursors to thin film structures. In *Thin Solid Films*, volume 409, pages 138–146, 2002.

[71] E. Granneman, P. Fischer, D. Pierreux, H. Terhorst, and P. Zagwijn. Batch ALD: Characteristics, comparison with single wafer ALD, and examples. *Surface and Coatings Technology*, 201(22-23 SPEC. ISS.):8899–8907, 2007.

[72] G.N. Parsons, S.M. George, and M. Knez. Progress and future directions for atomic layer deposition and ALD-based chemistry. *MRS Bulletin*, 36(11):865–871, 2011.

[73] S Veprek, M Veprekheijman, P Karvankova, and J Prochazka. Different approaches to superhard coatings and nanocomposites. *Thin Solid Films*, 476(1):1–29, April 2005.

[74] S. Veprek and M.J.G. Veprek-Heijman. Industrial applications of superhard nanocomposite coatings. *Surface and Coatings Technology*, 202(21):5063–5073, jul 2008.

[75] Y.X. Wang and S. Zhang. Toward hard yet tough ceramic coatings. *Surface and Coatings Technology*, 258:1–16, 2014.

[76] B. Borawski, J. Singh, J.A. Todd, and D.E. Wolfe. Multi-layer coating design architecture for optimum particulate erosion resistance. *Wear*, 271(11-12):2782–2792, September 2011.

[77] K. Miyoshi, B. Pohlchuck, K.W Street, J.S. Zabinski, J.H. Sanders, A.A. Voevodin, and R.L.C. Wu. Sliding wear and fretting wear of diamondlike carbon-based, functionally graded nanocomposite coatings. 225-229:65–73, 1999.

[78] K.L. Choy and E. Felix. Functionally graded diamond-like carbon coatings on metallic substrates. *Materials Science and Engineering a-Structural Materials Properties Microstructure and Processing*, 278(1-2):162–169, 2000.

[79] Y. Liu and E. I. Meletis. Tribological behavior of DLC coatings with functionally gradient interfaces. *Surface and Coatings Technology*, 153(2-3):178–183, 2002.

[80] K. L. Rutherford, S. J. Bull, E. D. Doyle, and I. M. Hutchings. Laboratory characterisation of the wear behaviour of PVD-coated tool steels and correlation with cutting tool performance. *Surface and Coatings Technology*, 80(1-2):176–180, 1996.

[81] S.C. Santos, W.F. Sales, F. J. da Silva, S.D. Franco, and M.B. da Silva. Tribological characterisation of PVD coatings for cutting tools. *Surface and Coatings Technology*, 184(2-3):141–148, 2004.

[82] V.P. Astakhov. The assessment of cutting tool wear. *International Journal of Machine Tools and Manufacture*, 44(6):637–647, 2004.

[83] R. M'Saoubi, M. P. Johansson, and J. M. Andersson. Wear mechanisms of PVD-coated PCBN cutting tools. *Wear*, 302(1-2):1219–1229, 2013.

[84] K.J. Wahl, M. Belin, and I.L. Singer. A triboscopic investigation of the wear and friction of MoS2 in a reciprocating sliding contact. 214(2):212–220, 1998.

[85] H. Ronkainen, S. Varjus, and K. Holmberg. Friction and wear properties in dry, water- and oil-lubricated DLC against alumina and DLC against steel contacts. *Wear*, 222(2):120–128, 1998.

[86] B. Navinšek, P. Panjan, and I. Milošev. PVD coatings as an environmentally clean alternative to electroplating and electroless processes. In *Surface and Coatings Technology*, volume 116-119, pages 476–487, 1999.

[87] H. Hoche, S. Groß, R. Foerster, J. Schmidt, and W. Adamitzki. Development of decorative and corrosion resistant coatings for the surface refinement of magnesium alloys by plasma-based methods. In *Plasma Processes and Polymers*, volume 6, 2009.

[88] J. Robertson. Diamond-like amorphous carbon. *Materials Science and Engineering R*, 37:129–281, 2002.

[89] N.M. Chekan, N.M. Beliauski, V.V. Akulich, L.V. Pozdniak, E.K. Sergeeva, A.N. Chernov, V.V. Kazbanov, and V.A. Kulchitsky. Biological activity of silver-doped dlc films. *Diamond and Related Materials*, 18(5 - 8):1006 – 1009, 2009. Proceedings of Diamond 2008, the 19th European Conference on Diamond, Diamond-Like Materials, Carbon Nanotubes, Nitrides and Silicon Carbide.

[90] Dorota Bociaga, Piotr Komorowski, Damian Batory, Witold Szymanski, Anna Olejnik, Krzysztof Jastrzebski, and Witold Jakubowski. Silver-doped nanocomposite carbon coatings (ag-dlc) for biomedical applications: Physiochemical and biological evaluation. *Applied Surface Science*, 355:388 – 397, 2015.

[91] G. Bolelli, L. Lusvarghi, M. Montecchi, F. Pighetti Mantini, F. Pitacco, H. Volz, and M. Barletta. HVOF-sprayed WC-Co as hard interlayer for DLC films. *Surface and Coatings Technology*, 203(5-7):699–703, December 2008.

[92] G. Bolelli, B. Bonferroni, G. Coletta, L. Lusvarghi, and F. Pitacco. Wear and corrosion behaviour of HVOF WC-CoCr CVD-DLC hybrid coating systems deposited onto aluminium substrate. *Surface and Coatings Technology*, 205(17-18):4211–4220, May 2011.

[93] J. Llorca, C. González, J. M. Molina-Aldareguía, J. Segurado, R. Seltzer, F. Sket, M. Rodríguez, S. Sádaba, R. Muñoz, and L. P. Canal. Multiscale modeling of composite materials: A roadmap towards virtual testing. *Advanced Materials*, 23(44):5130–5147, 2011.

[94] S. Usmani. *Abrasion and sliding friction of thermal spray coatings*. PhD thesis, State University of New York at Stony Brook, 1997.

[95] S. Usmani, S. Sampath, D.L. Houck, and D. Lee. Effect of carbide grain size on the sliding and abrasive wear behaviour of thermally sprayed WC-Co coatings. *Tribology Transactions*, 40(3):470–478, 1997.

[96] Astm e384 - 11e1 standard test method for knoop and vickers hardness of materials.

[97] Astm e10 - 15 standard test method for brinell hardness of metallic materials, 2001.

[98] Astm d2240 - 05(2010) standard test method for rubber property - durometer hardness, 2001.

[99] Astm e18 - 15 standard test methods for rockwell hardness of metallic materials, 2001.

[100] Metallic materials – instrumented indentation test for hardness and materials parameters – part 1: Test method, iso 14577-1, 2002.

[101] A.G. Evans and T.R. Wilshaw. Quasi-static solid particle damage in brittle solids -I. Observations, analysis and implications. *Acta Metallurgica*, 1976.

[102] G.R. Anstis, P. Chantikul, B.R. Lawn, and D.B. Marshall. A Critical Evaluation of Indentation Techniques for Measuring Fracture Toughness: I, Direct Crack Measurements. *Journal of the American Ceramic Society*, 64(9):533–538, 1981.

[103] Y. Tanaka, N. Ichimiya, Y. Onishi, and Y. Yamada. Structure and properties of Al-Ti-Si-N coatings prepared by the cathodic arc ion plating method for high speed cutting applications. *Surface and Coatings Technology*, 147:215–221, 2001.

[104] F. Sergejev and M. Antonov. Comparative study on indentation fracture toughness measurements of cemented carbides. *Proceedings of the Estonian Academy for Science and Engineering*, 12(4):388–398, 2006.

[105] J. Valli, U. Mäkelä, A. Matthews, and V. Murawa. TiN coating adhesion studies using the scratch test method. *Journal of Vacuum Science & Technology A: Vacuum, Surfaces, and Films*, 6(A 3):2411–2414, 1985.

[106] S.J. Bull. Can scratch testing be used as a model for the abrasive wear of hard coatings? *Wear*, 1999.

[107] S.J. Bull and E.G. Berasetegui. An overview of the potential of quantitative coating adhesion measurement by scratch testing. *Tribology International*, 2006.

[108] Standard test method for evaluation of scratch resistance of polymeric coatings and plastics using an instrumented scratch machine. In *ASTM D7027-13*.

[109] Quantitative evaluation of scratch-induced damage and scratch visibility. In *BS ISO 17541*, 2014.

[110] Thermal spraying – evaluation of adhesion/cohesion of thermal sprayed ceramic coatings by transverse scratch testing, iso 27307, April 2015.

[111] D D Env. BS EN 1071-3:2005 Advanced technical ceramics - Methods of test for ceramic coatings, 2005.

[112] Rolling bearings Balls. In *BS ISO 3290-2*, 2008.

[113] P. Kivikytö-Reponen, A. Laukkanen, M. Apostol, R. Waudby, T. Andersson, A. Helle, K. Valtonen, and V.-T. Kuokkala. Modelling and testing of elastomer impact deformation under high strain rates. *Tribology - Materials, Surfaces & Interfaces*, 8(1):48–54, March 2014.

[114] Aisi 52100.

[115] I. Kleis. The device for erosion testing. *Proceedings of Technical University of Tallinn*, 152(1):1–19, 1958. (In Russian).

[116] I. Kleis and K. Priit. *Solid Particle Erosion.* Springer London, London, 2008.

[117] K. Holmberg, A. Laukkanen, H. Ronkainen, R. Waudby, G. Stachowiak, M. Wolski, P. Podsiadlo, M. Gee, J. Nunn, C. Gachot, and L. Li. Topographical orientation effects on friction and wear in sliding dlc and steel contacts, part 1: Experimental. *Wear*, 330-331:3–22, 2015.

[118] D.G. Teer. Magnetron sputter ion plating, August 1996.

[119] S. Yang and D.G. Teer. Investigation of sputtered carbon and carbon/chromium multilayered coatings. *Surf. Coat. Technology*, 131:412–416, 2000.

[120] R.K. Singh, L. Zhou, L. Li, P. Munroe, M. Hoffman, and Z. Xie. Design of functionally graded carbon coatings against contact damage. *Thin Solid Films*, 518:5769–5776, 2010.

[121] T. Suhonen. Private communication. VTT Technical Research Centre of Finland Ltd., Finland, 2014.

[122] P.J. Burnett and D.S. Rickerby. The relationship between hardness and scratch adhesion. *Thin Solid Films*, 154:403–416, 1987.

[123] J. Nohava, B. Bonferroni, G. Bolelli, and L. Lusvarghi. Interesting aspects of indentation and scratch methods for characterization of thermally-sprayed coatings. *Surface and Coatings Technology*, 205(4):1127–1131, November 2010.

[124] F. Beltzung, G. Zambelli, and E. Lopez. Fracture toughness measurement of plasma sprayed ceramic coatings. *Thin Solid Films*, 181(1-2):407–415, 1989.

[125] K. Holmberg, A. Laukkanen, H. Ronkainen, K. Wallin, and S. Varjus. A model for stresses , crack generation and fracture toughness calculation in scratched TiN-coated steel surfaces. *Wear*, 254:278–291, 2003.

[126] B.D. Beake, V.M. Vishnyakov, and A.J. Harris. Relationship between mechanical properties of thin nitride-based films and their behaviour in nano-scratch tests. *Tribology International*, 44(4):468–475, April 2011.

[127] K Holmberg. Tribological analysis of TiN and DLC coated contacts by 3D FEM modelling and stress simulation. *Wear*, 264(9-10):877–884, April 2008.

[128] J.M.J. den Toonder, J. Malzbender, G. de With, and A.R. Balkenende. Fracture toughness and adhesion energy of sol-gel coatings on glass. *Journal of Materials Research,*, 177(1):224–233, 2002.

[129] J.P.A. Tillett. Fracture of Glass by Spherical Indenters. *Proceedings of the Physical Society Section B*, pages 47 – 54, 1955.

[130] I. Kleis and P. Kulu. *Solid Particle Erosion.* 2007.

[131] S.F. Wayne, J.G. Baldoni, and Buljan S.-T. Abrasion and erosion of wc-co with controlled microstructures. *Tribology Transactions*, 4(33):611–617, 1990.

Appendix A

Surface roughness test parameters

Parameter	Unit	Value
Stylus radius	µm	2 (check)
Sliding speed	mm/sec	0.2
Number of samples	-	5
Sampling length	mm	0.08
Z-range	µm	0.008

Table A.1: Surface roughness test parameters

Appendix B

Percussive normal impact assessment: Impact force vs. time

The low-load (100 N) percussive impact equipment recorded the force at regular intervals with a load cell. Using Matlab v2015b, a program was developed to assess the measured force vs. time data. Generally, 10 % of all impact events were recorded in an effort to minimise computational demands. The Matlab program used the script presented in Section B.1. The program counted the number of recorded peaks, the average measured peak impact force and the variation of the peak impact force. Examples of the output data are given in Figures B.1 and B.2.

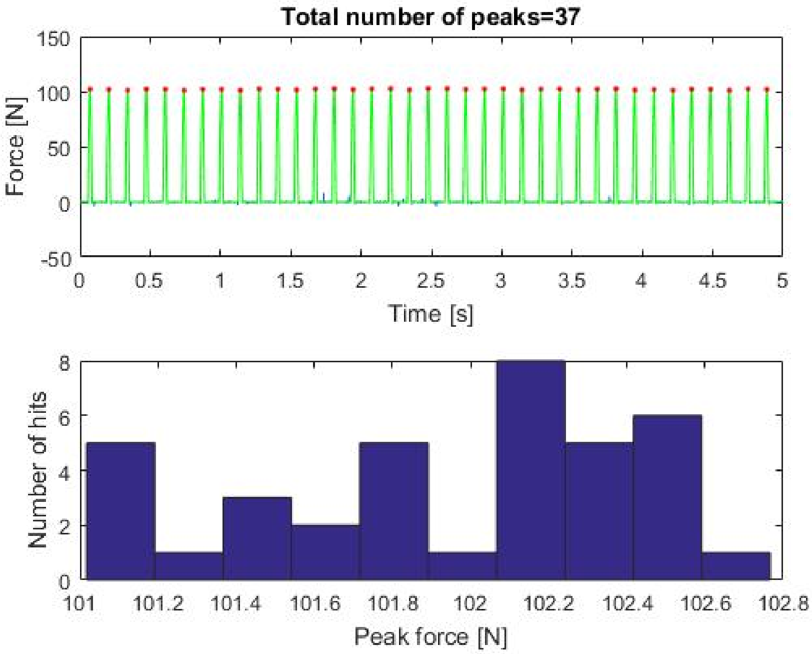

Figure B.1: An example of the plots generated by the Matlab script to plot the measured impact force vs. time (top) and a histogram of the measured impact force (bottom)

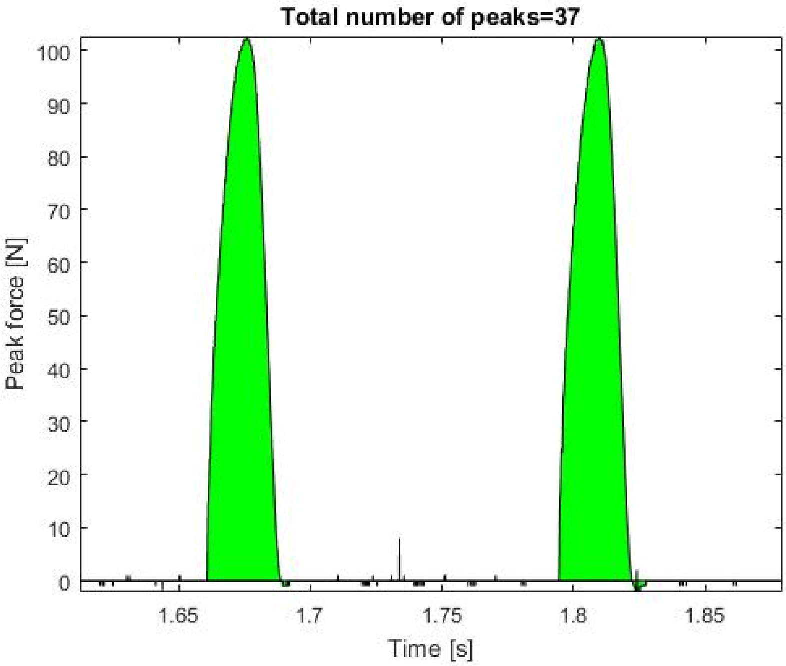

Figure B.2: Typical impact force-time curves for two impact events

B.1 Matlab v2015b script

1. clear close all set(gca, ’FontSize’, 20) set(0,’defaulttextfontsize’,18);
2. timeCount = cputime;
3. tDelta = 1e-4; % time interval between measurements
4. Ninterp = 12; % number of measurements used to fit one spline
5. polyDeg = 3; % degree of least-square splines (3rd degree = parabola)
6. Nsub = 500000000000000; % consider first Nsub measurements
7. minimumPeakHeight = 70; %minimumPeakDistance = 0.05;
8. cd(’folder name’);
9. A=load(’input data file’);
10. A=A(:,2); % ’:’ = pick every element column-wise, ’2’ = pick column number two
11. y=A(2:end); % measurement data
12. Nraws = length(y); % number of measurements
13. Nsub = min(Nsub,Nraws);
14. %Nsub = Nsub*0.1 tEnd = tDelta*(Nraws-1); % end time of measurements
15. x = 0:tDelta:tEnd; % vector of time steps in the measurements
16. xSub = x(1:Nsub); ySub = y(1:Nsub);
17. subplot(2,1,1) plot(xSub,ySub)
18. tInterval = Ninterp*tDelta; % time interval between two splines
19. tEndSub = (Nsub-1)*tDelta; % end time of the sub
20. xSubPolyPlot = linspace(0,tEndSub,2*Nsub);
21. Npolys = round(tEndSub/tInterval); % total number of splines used for the data
22. B = spap2(Npolys,polyDeg,xSub,ySub); % calculate the splines for the data

```
hold on;
pp = fn2fm(B,’pp’);
ySubPolyPlot = fnval(B,xSubPolyPlot);
hold on;
plot(xSubPolyPlot,ySubPolyPlot,’g’)
hold on;
[peaks,locs] = findpeaks(ySubPolyPlot,’MINPEAKHEIGHT’,minimumPeakHeight);%,’MINP
xPeaks = xSubPolyPlot(locs);
plot(xPeaks,peaks,’.r’)
xlabel(’Time [s]’);
ylabel(’Force [N]’);
titleStr = strcat(’Total number of peaks=’,num2str(length(peaks)));
title(titleStr)
subplot(2,1,2)
hist(peaks)
xlabel(’Peak force [N]’);
ylabel(’Number of hits’);
timeCountEnd = cputime - timeCount
figure;
tDiffs = zeros(Nsub-1,1);
for i=1:Nsub-1 tDiffs(i) = abs(y(i+1) - y(i));
end title(’Time interval distribution’);
hist(tDiffs,20)
xlabel(’Time interval’);
```

47. ylabel('Number of counts');

48. figure;

49. plot(xSub,ySub) trapz(xSub,ySub) area(x,y,'FaceColor','g') %plot as an area %facecolour: % b,g,k,r

50. xlabel('Time [s]');

51. ylabel('Peak force [N]');

52. titleStr = strcat('Total number of peaks=',num2str(length(peaks)));

53. title(titleStr);

The impact deformation and wear of thick composite coatings

ISBN 978-951-38-8551-9 (URL: http://www.vttresearch.com/impact/publications)
ISSN-L 2242-1211
ISSN 2242-122X (Online)
http://urn.fi/URN:ISBN:978-951-38-8551-9

VTT TECHNOLOGY 300 The impact deformation and wear of...